Microfabricted passive preconcentrator/injector designed for microscale gas chromatography

by

Jung Hwan Seo

A dissertation submitted in partial fulfillment
of the requirements for the degree of
Doctor of Philosophy
(Mechanical Engineering)
in The University of Michigan
2012

Doctoral Committee:

Professor Katsuo Kurabayashi, Chair
Associate Professor Xudong Fan
Associate Professor Wei Lu
Assistant Professor Kenn Oldham

©   Jung Hwan Seo

2012

ACKNOWLEDGEMENTS

To my family.

TABLE OF CONTENTS

LIST OF FIGURES

LIST OF TABLES

LIST OF APPENDICIES

ABSTRACT

Microelectromechanical system (MEMS) technology enables the realization of miniaturized lab-on-a-chip analytical systems. One of the active MEMS research areas is microscale chromatography (μGC) capable of field-deployable *in situ* gas analysis. An analytical μGC system promises to meet the need for hand-held, low-cost, and low-power instruments analyzing complex organic compounds. Prominent applications of μGC include environmental air monitoring, homeland security, military surveillance, and biomedical diagnostics.

In particular, a complete μGC system comprises at least the following three essential microscale components: (1) a preconcentrator, (2) a column, and (3) a detector. A micromachined preconcentrator plays a major role in the quantitative detection of volatile organic compounds (VOC) in moderately complex mixtures using a μGC system. The preconcentrator installed at the front end of an analytical system significantly enhances the detection performance of a μGC system by trapping and concentrating analytes. Preconcentrated vapors are thermally desorbed by a heat pulse generated at the heater integrated in the preconcentrator and delivered as a concentrated plug into the downstream separation column by pumping. A narrow injection time-width pulse of analytes by rapid thermal desorption leads to a significant improvement in the separation ability of the system. Thus, there is a strong need for a power-efficient microfabricated preconcentrator capable of achieving high preconcentration and rapid heating.

Here, we present design, fabrication, thermal operation, and characterization of a device named the microfabricated passive preconcentrator/injector (μPPI), which captures VOC mixtures from the ambient by diffusion without a pump. The μPPI consists of two layer structures; the top layer incorporates vertical square diffusion channels for passive vapor sampling; and the bottom layer contains a membrane cavity structure with pillar structures to retain carbon adsorbent granules inside and an integrated heater on its backside for injecting captured VOCs downstream by thermal desorption. Fluidic and heat transfer models are developed to guide the device design to ensure power-efficient sample transfer during the thermal desorption. Comprehensive tests of the μPPI demonstrate its general utility to enhance the detection performance of a μGC system.

Experiments performed with four individual VOCs at concentrations of ~ 500 ppb show that the μPPI yields high sampling rates of 8.7, 8.6, 9.0, and 6.9 mL/min for benzene, Trichloroethylene (TCE), toluene, and *m*-xylene, respectively, for up to ~ 45 min. The μPPI can reach 250 ˚C within 0.3 s with 1 W of applied power. The study identifies an optimal heating condition of 90 ˚C/s for the μPPI that results in complete separation of a quaternary VOC mixture. From an analysis of chromatograms obtained with the sampling time of 60 min, the μPPI traps the quaternary mixture in the mass-ratio of 13.6 % for benzene, 20.7 % for TCE, 24.6 % for toluene, and 41.1 % for *m*-xylene. The results of these comprehensive tests demonstrate the μPPI's ability to significantly enhance detection sensitivity and separation resolution by zero power passive analyte

preconcentration and power-efficient rapid heating. The μPPI opens a new way to realize a battery-operated standalone hand-held microanalytical system.

CHAPTER I

INTRODUCTION

1.1 Research Introduction and Background

Exposure to volatile organic compounds (VOC) can seriously affect human health. These compounds in the air should be monitored and analyzed for environmental and human health protection [1, 2]. Gas chromatography (GC) is a powerful technique commonly employed in a laboratory setting to analyze VOCs in a moderately complex mixture [3, 4]. The components of a VOC mixture sample can be physically separated and quantitatively identified by a GC system. However, conventional GC systems comprise typically large, expensive, fragile, high power, and complicated bulky pieces of instruments. As a result, it is challenging to acquire on-site data of indoor/outdoor environment air quality using these systems. A low-cost, miniaturized, and hand-held analytical instrument, namely a gas chromatographic microsystem (μGC), is highly desirable to address the challenge. Such a microsystem enables field-deployable *in situ* data analysis of a gas sample. In addition, μGC systems find wide use in indoor environmental monitoring of homes, building offices or factories, point-of-care health diagnostics, and homeland security.

Microelectromechanical system (MEMS) technology offers clear advantages over conventional fabrication methods for miniaturizing an analytical system down to the microscale. The microscale dimensions of MEMS devices lead to low-power consumption and fast thermal response due to their small thermal mass while allowing development of portable devices [5]. MEMS technology allows microfabrication of all the three essential components of a μGC system, i.e., a preconcentrator, a separation column, and a detector. The preconcentrator serves as a device for sample collection and injection. The separation column, typically consisting of two polymer-coated silicon channels and an anodically bonded glass cap with an integrated heater, is conceived to achieve separation of a wide range of compounds. The detector used for the determination of the analytes eluted from the column could be an either of a chemiresistor, a thermal conductivity detector, a flame ionization detector, an optical detector, a surface acoustic wave detector, or a differential mobility spectrometer.

Many applications using a microanalytical system often require the detection of VOCs at low concentration levels of the parts-per-billion (ppb). However, the inherent lack of sensitivity for most detectors limits the detection of such a low concentration of the target analytes. Thus, preconcentration of VOCs is an inevitable process here. Physisorption is the phenomenon governing the preconcentration process, where weak intermolecular interactions between analyte molecules and an adsorbent surface are caused by means of Van de Waals force. Physisorption processes can easily be reversed by heating that raises the internal energy and breaking the weak bonds. The method based on physisorption is preferred for preconcentration due to its simplicity and reversibility.

Physisorption is driven by two mechanisms: cryogenic cooling (cold trapping) [6] and adsorption trapping [7]. Cryogenic cooling traps analytes on sorbents or device surfaces at a temperature below their boiling points. This method requires high power to cool down the system to -150 ˚C ~ -170 ˚C. On the other hand, adsorption trapping immobilizes analytes on the surface of adsorbents at room temperature. The surface energy of the adsorbents become lowered by the attachment of the analyte molecules. A high surface-to-volume ratio is typically needed for the adsorbents to trap a large amount of analytes. Therefore, a cooling-free, adsorption-based microfabricated preconcentrator is highly desirable for use in a gas chromatographic microsystem.

A microfabricated preconcentrator (μ-preconcentrator) also plays a critical role as an injector in a μGC system. The preconcentrated analytes should be rapidly delivered to a downstream analytical system in the form of a narrow desorption peak yielding local high concentration. This sharp analyte peak pulse enhances the separation capability and detection sensitivity of GC analysis. As such, a μ-preconcentrator has the two important functions of trapping a chemical sample and injecting concentrated sample vapors to the inlet of a downstream analytical system by thermal desorption. As VOC analytes at low concentrations pass through the device, the adsorbents packed in or deposited on the surface of the device chamber trap these compounds over a period of time, followed by subsequent rapid thermal desorption.

This thesis work develops a new μ-preconcentrator that achieves both vapor sample trapping at zero power consumption and rapid thermal desorption at low heating power using MEMS technology and fluidic and heat-transfer modeling.

1.2 Research Motivation

This research is primarily motivated by the need for a new approach to reducing electrical power consumption in carrier gas pumping for the vapor sampling by a microfabricated preconcentrator. The power reduction is highly critical to develop a portable μGC system. Several researchers have developed μ-preconcentrators, which typically comprise a micromachined device with an internal cavity packed or lined with adsorbent materials. VOC mixtures in an air sample, drawn through these preconcentrators by means of a small pump, are trapped on the surfaces of the adsorbents. As more power-efficient μGC components are developed, the pumping process becomes highly dominant in power consumption and presents itself as a bottleneck against realizing a battery-operated hand-held system. Although several prototypes of low-power microfabricated pumps have been demonstrated, their pumping capacity is still limited and insufficient for the operation in a complete μGC system [8, 9]. Most μGC systems still use commercial pumps whose power is comparable to that required for thermal operations of microscale preconcentrators and separation columns [10-17]. For the detection of a low concentration range of VOCs, which requires a large sample volume over a long period of time for analysis, the energy used for pumping easily exceeds that for the other subsystems.

This research is also motivated by the need to improve the vapor thermal desorption and injection performance of a μ-preconcentrator. This is required to achieve high-resolution chromatographic separation of VOC mixtures at low power. Preconcentrators for detecting a broad spectrum of VOCs require a thicker and a more complicated cavity structure to retain adsorbent granules than analyte-specific devices that incorporate a membrane structure coated with a vapor-adsorbing polymer thin film [25-35]. The problem is that the former devices typically suffer from poor heat transfer due to poor heat transfer in their structures. Thus, detection of complex organic compound mixtures using these preconcentrators requires relatively high power (2 ~ 10 W) with slow thermal response [18-20, 22, 23]. This hinders the generation of sharp analyte injection pulses leading to high separation resolution as well as the reduction of power required for the development of a hand-held system.

This study employs a non-conventional sampling method that eliminates the use of a pump on the basis of vapor diffusion. This passive sampling method enables us to significantly reduce energy consumption for VOC analysis. Moreover, we design a membrane structure-based preconcentrator device to achieve enhanced thermal desorption/injection performance even at low power using proper fluidic and thermal models. This thesis describes the development of a new MEMS device that overcomes the aforementioned problems with microfabricated preconcentrators for VOC mixture detection.

1.3 Thesis Objectives

This research has four main goals to address the shortcomings of existing microscale preconcentration technologies. The first objective is to establish a new approach to molecular diffusion-based vapor collection for developing a zero-power passive sampling preconcentrator. The second objective is to achieve rapid thermal desorption and injection of trapped VOCs at a membrane cavity structure with an optimal thermal design. The third objective is to explore the influence of heating conditions on the chromatographic separation resolution of a μGC system incorporating the designed preconcentrator; here, a multi-physics model accounting for heat transfer, fluid dynamics, and vapor desorption kinetics is developed. With careful engineering analysis, this work provides a device design/operation guideline to achieve accurate GC analysis in a microanalytical system. The final objective is to demonstrate the general utility of our device for analyzing a broad spectrum of VOC mixtures with a GC system. This study provides a new microscale device to significantly improve the detection sensitivity and separation resolution of GC analysis that differentiates and identifies a large number of analyte species in a complex mixture.

1.4 Thesis Outline

The thesis study comprises five subsequent technical chapters. The outline of the thesis is summarized as follows:

Chapter II − Review of Related Studies: This chapter reviews other studies related to this thesis work and providing essential information for this project. The chapter summarizes other competing technologies targeting similar goals and applications. The review is focused on two main topics: (1) gas chromatographic microsystems and (2) microscale preconcentrators. Each section summarizes representative studies concerning one of these topics.

Chapter III − Passive vapor sampling of microfabricated preconcentrator/ injector: This chapter describes design, fabrication, and preliminary testing of a new MEMS device, namely the microfabricated passive preconcentrator/injector (μPPI). The device design concept is first described, showing how the passive sampling method can be integrated into a micromachined device for vapor preconcentration. Next discussed are design specifications, fabrication processes, and experimental methods used for testing the device performance. The power dissipation and thermal response of the device are then characterized by gravimetric tests to measure the initial mass uptake rate for toluene. Finally, the sampling rate and sampling capacity as well as the sample loss upon the thermal vapor desorption are studied for the μPPI using a custom chamber setup.

Chapter IV − Impact of microscale on-chip heating on vapor release and injection: This chapter discusses the influence of on-chip heating conditions on the vapor desorption and injection performance of the μPPI. Our study develops a modified desorption kinetic model coupled with heat transfer theory to predict the dynamic process associated with the vapor thermal desorption. Using an experimental setup incorporating an optical sensor and the aforementioned custom chamber, we observe elution peak signals generated by our device and characterize their peak height, full width at half maximum, and peak tailings. Comparing the experimental results with model prediction elucidates how the thermal desorption/vapor injection behavior of the μPPI affects the resulting peak band signal characteristics.

Chapter V − Preconcentration, Injection, and Separation performance for VOC mixtures: This chapter achieves preconcentration, desorption/injection, and separation of a VOC mixture sample using the μPPI to demonstrate the device's general utility in a μGC system. A custom GC system fluidically integrating the μPPI and dual optical sensors is first developed and then used to demonstrate the full μPPI-based GC operations. Calibrations of the optical sensor signals for the tested 4 vapor analytes are performed for subsequent quantitative measurements. Next, the sampling rates for these analytes are measured. We then experimentally determine an optimal heating condition to generate a sharp vapor injection pulse by the μPPI and obtain complete separation of the components of the VOC mixture. Finally, we analyze chromatograms resulting from the complete separation verifying the detection sensitivity enhancement caused by using the μPPI.

Chapter VI − Conclusions and Future Work: This final chapter summarizes the impact of the presented research and discusses future work on the μPPI. The current study can be extended to two directions: (1) in-depth study of the performance of the μPPI for preconcentration and separation of sub-ppb-level vapor mixtures when integrated in a GC system and (2) full integration of the μPPI with a microfabricated column and sensor to develop a battery-operated low-power μGC system.

CHAPTER II

REVIEW OF RELATED STUDIES

In this chapter, we review previous studies related to this thesis research. Reviewing these studies helps justify our research as well as provides an overview of other competing technologies. Our work aims to provide a new MEMS preconcentrator device as a useful component for microscale gas chromatography. To benchmark our device against state-of-the-arts, we review current (1) gas chromatographic microsystems and (2) microscale preconcentrators.

2.1 Gas Chromatographic Microsystems

Components of a complete μGC system typically include micropreconcentrators [18-35], microcolumns [36-45], microsensors [46-59], and micropumps [8]. Several studies developed individual micromachined components or subsystems combining a micromachined column with another component [60-62]. However, only a few studies demonstrated a complete μGC system consisting of at least three essential components micromachined, *i.e.*, a preconcentrator, a column, and a detector [10-14, 37, 63].

Terry *et al.* first pioneered a miniaturized gas analysis system fabricated on a Si wafer [64] and Reston and Kolesar subsequently reported a GC system employing a micromachined column and thermal conductivity detector [65, 66]. Since then, several researchers have developed μGC systems potentially enabling low-power, low-cost, low-volume, rapid analysis, and battery-operated hand-held operation [10-14].

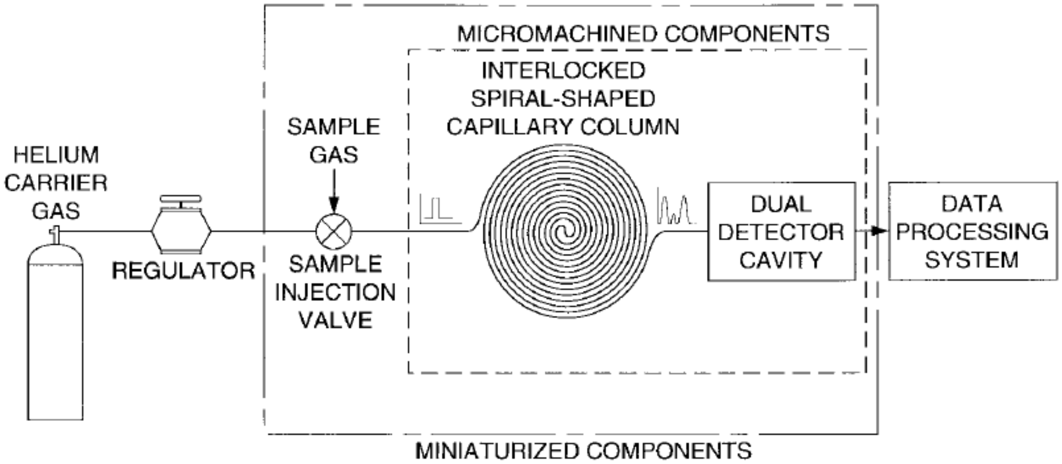

Figure 2.1 Functional block diagram of the micromachined gas chromatography (GC) system [67]

Figure 2.1 shows the earliest silicon micromachined GC system consisting of a carrier gas supply, a sample injection system, a separation column, and a detector, all fluidically connected to each other. The data processing system connected to the detector was used for signal analysis. In this system, the separation column and the detector were the only microfabricated components. To separate vapor analytes, a certain amount of gas volume extracted from the environment was injected into the capillary column via an inert carrier gas using the sample injection valve. Each analyte component has a different vapor pressure in the mixture sample and elutes at a different time after interacting with a stationary-phase film coating the inner surface of the column. Consequently, the effluents of the components of the vapor mixture emerge from the separation column as a series of

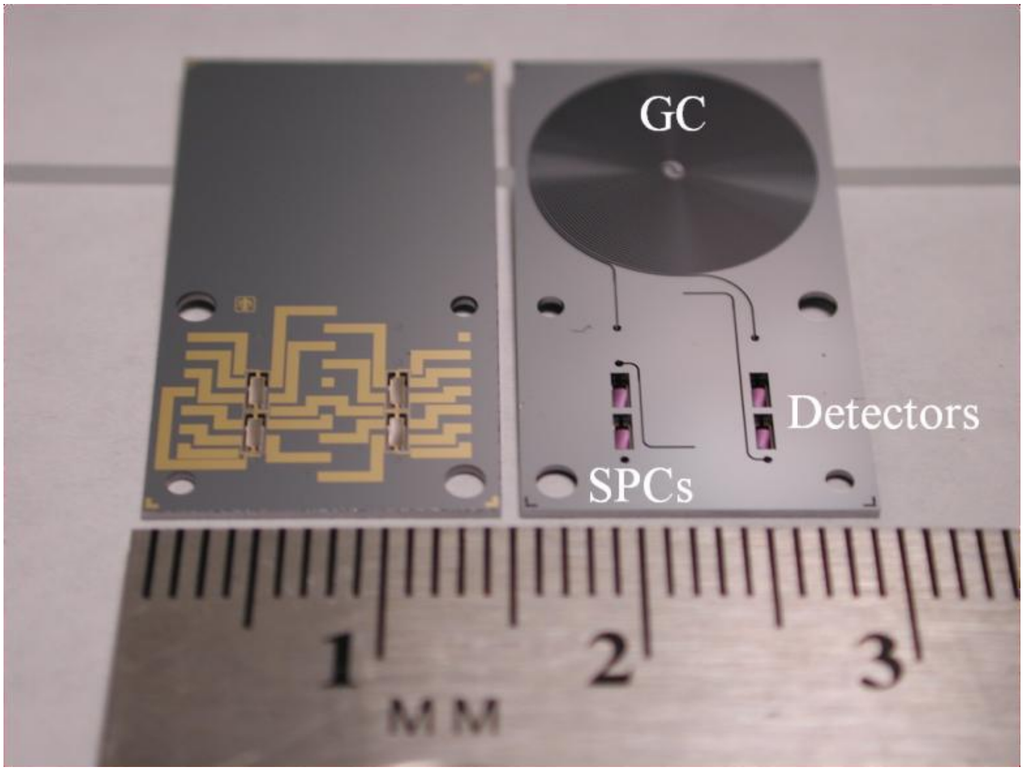

Figure 2.2. Two monolithically-integrated μGCs chips side-by-side. The chip on the left-hand side has the metallic traces used to electrically connect the PC and sensor shown face up. The chip on the right hand side is metal-side down to show the fluidic channels and deep reactive ion etched (DRIE) μGC channel [59].

separated peaks in the inert carrier gas. The system incorporated a chemiresistor detector, which measures the particular property of each analyte (*e.g.*, thermal conductivity, electrical conductivity, etc.), to analyze the separated components of the mixture sample. The early-stage micromachined GC systems needed high analayte concentrations (~ as high as several hundreds of parts-per-million (ppm)) because of the limited sensitivity of the gas detector.

More recently, Sandia National Laboratories developed the μChemLab® , the first fully microfabricated GC system with all of its essential components micromachined. This system incorporated a microfabricated preconcentrator with a micromachined-Si separation column and an integrated acoustic-wave sensor array into a hybrid microanalyzer [12, 28]. A revised system with monolithically integrated components was recently reported (Fig. 2.2) [59]. In their new system, a magnetically-actuated pivot plate resonator (PPR) sensor and a GC column were fabricated on the same Si chip. The detector relies on Lorentz force generated by an alternating current in the presence of a magnetic field to drive the sensor platform into mechanical oscillation. The sensor coated with a thin polymer layer traps the sample and the resulting mass change induces an oscillation frequency shift, which is electronically detected. It is also used as a mass-sensitive preconcentrator due to its trapping function. Here, monolithic integration of a MEMS GC column and a PPR sensor on the same platform greatly simplified the system fabrication. However, the operation of this monolithic microsystem is only limited to analyzing specific chemical warfare agents (CWA), which represent a narrow spectrum of VOC species.

To overcome this limitation, other laboratories have developed a whole μGC system assembled from separately fabricated subsystems for comprehensive environmental vapor analysis in the low-ppb range [10, 11, 37]. In 2004, Dziuban *et al.*, developed the first portable GC system in Europe [37]. This system employed a micromachined injector and a thermal conductivity detector (TCD). The injector in this system compresses a vapor sample by electromagnetic valve actuations. which requires fluidically complicated interconnections and operations to collect samples. The TCD detects a temperature increase caused by chemical reaction of the device's polymer coating with the vapor sample. However, the detector has low sensitivity of ~ 10 ppm and low preconcentration performance, thus limiting its application. More recently, Zampolli,

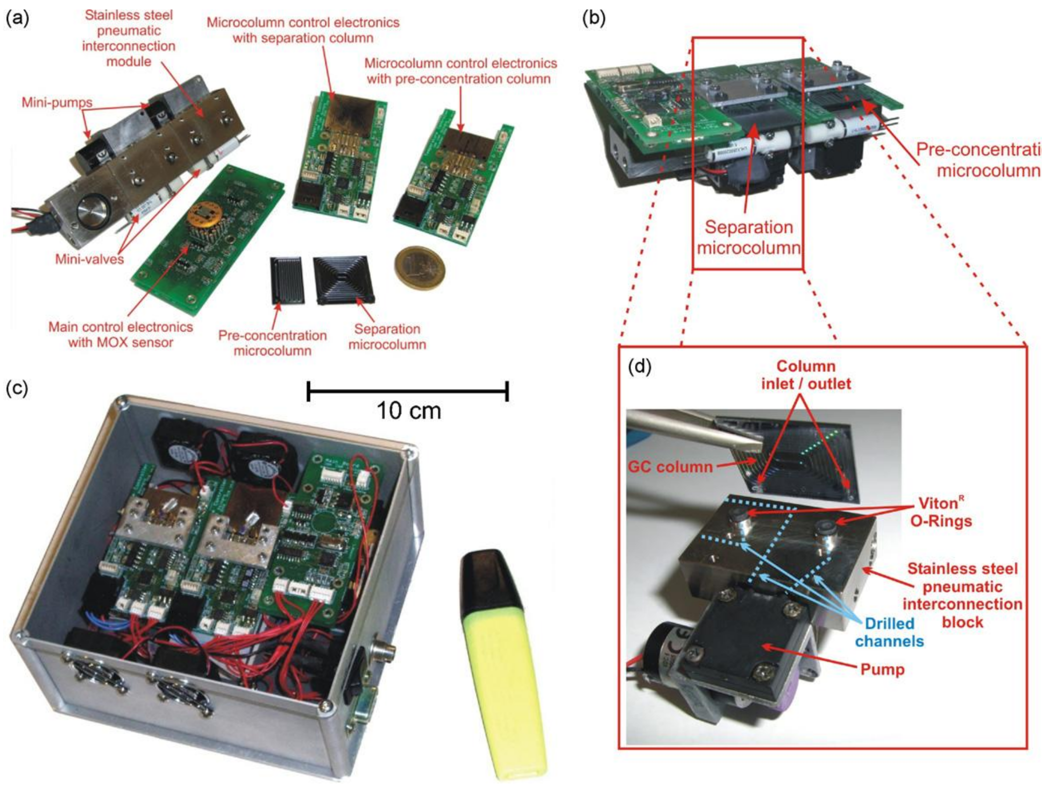

Figure 2.3. Photograph of the prototype miniGC system: single components (a), assembled mini GC (b), complete packaged prototype (c) and close-up on the pneumatic interconnections (d) [11].

et al. [11], a research group at the Institute of Microelectronics and Microsystems of the Italian National Research Council (CNR-IMM), developed a complete μGC system comprising a preconcentration column, a GC separation column, and a metal oxide semiconductor (MOX) solid-state gas sensor (Fig. 2. 3). The researcher fabricated the micromachined preconcentration column using a DRIE process, followed by anodic bonding of a Pyrex wafer for encapsulation. A metallic pattern was deposited on the back-side of the Si wafer to form a microheater. The fabricated channels were coated with a mesh of quinoxaline-bridged cavitand (QxCav) that engulfs aromatic compounds. A micromachined separation column was fabricated to form a 50 cm long spiral channel with a cross-section of 0.8 mm^2. The MOX sensor arrays highly sensitive to aromatic compounds were integrated in a Si-micromachined structure. This mesoscopic GC system detected benzene ranging ~ 0.5 ppb to ~ 2ppb after sampling 55 min at 50 mL/min. However, the implementation of this system is only limited to selective detection of aromatic compounds.

The Engineering Research Center for Wireless Integrated Microsystems (WIMS), University of Michigan, developed the first hybrid microfabricated gas chromatograph with all of its analytical components consisting of the MEMS devices (Fig. 2. 4). These components include an on-board calibration-vapor source, a microfabricated preconcentrator/focuser (μPCF), a separation column, and a multi-sensor array. The microfabricated calibration-vapor source was designed to generate calibrant vapor by diffusion from a liquid reservoir. This component was adjunctively used to compensate for several factors affecting analytical performance such as aging or drift. The μPCF, one of the aforementioned three essential components, traps organic vapors with a three-stage structure and thermally desorbs the captured/concentrated analytes. It is designed to provide a sharp injection pulse to enhance high-speed chromatographic separation performance. A series of three types of carbon-based adsorbents packed in the stages of the μPCF is used to trap a broad spectrum of volatile organic compounds (VOCs). The separation column employs a series of glass-capped square-spiral channels etched by the DRIE process to provide sufficient resolution to separate components in a vapor mixture. The μGC detector consists of an integrated array of four chemiresistors, each showing partially selective response to the analytes. The detector identifies the vapor type and quantifies the vapor concentration. This hybrid microsystem could separate and identify 11 vapor species in a moderately complex mixture within a few minutes. However, each of the components of this system suffered from either limited sample trapping/thermal

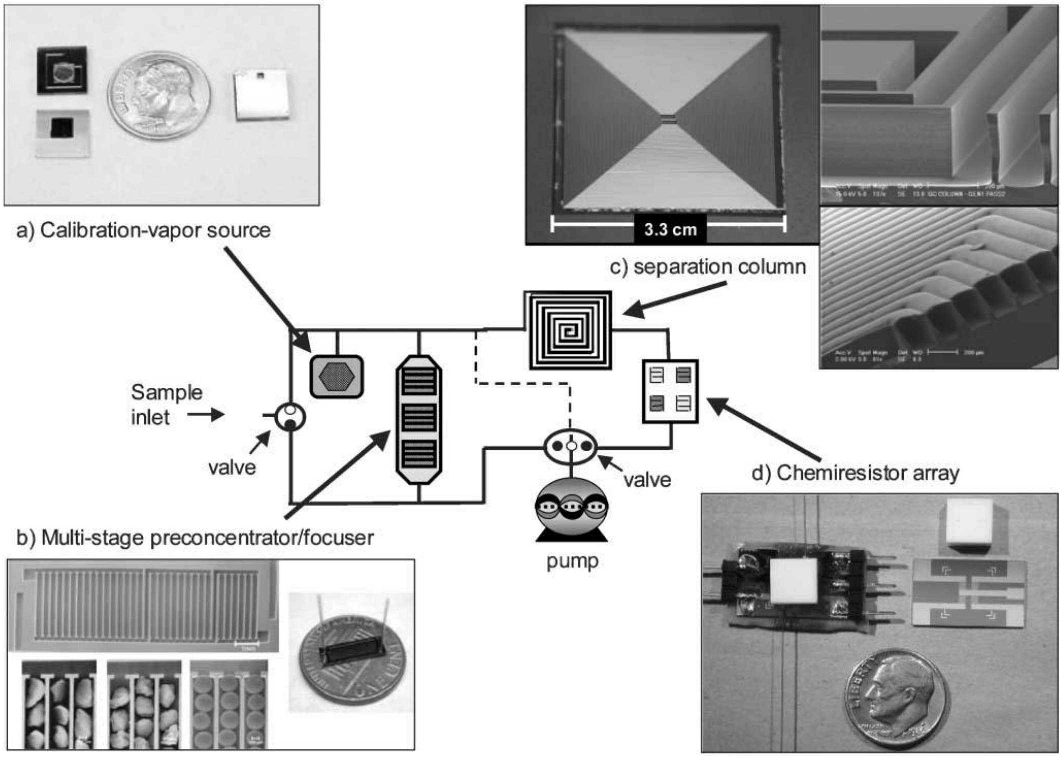

Figure 2.4. Block diagram of the MEMS μGC prototype analytical system: (a) calibration-vapor source before (left) and after (right) assembly; diffusion channel and headspace aperture can be seen in the top section and macro-PS reservoir can be seen in the bottom section; (b) 3-stage adsorbent μPCF prior to loading and sealing (top left), with close-up SEM images of each section loaded with adsorbents (lower left) and assembled structure with capillary interconnects on a U. S. penny; (c) 3 m separation-column chip (left) with close up views of the channel cross- sections prior to (top right) and after (lower right) sealing; (d) detector assembly with 4-chemiresistor array chip (right), Macor lid (white square structure), and sealed detector with connecting capillaries mounted on a custom mounting fixture (left). The dashed line is a flow-splitter [10]

performance, low desorption capability, poor separation resolution, or low detection sensitivity. Furthermore, the first-generation hybrid μGC system was not able to perform *in situ* gas analyses because of its insufficient capability of collecting an air sample from the field. The system operations were also limited to a laboratory environment because of the need for a data acquisition/system control desktop computer as well as several power supplies for driving the individual components.

Toward developing a complete field-deployable μGC, the WIMS center at the University of Michigan has improved the design and performance of several components of the aforementioned μGC system [10] and integrated them into a single unit for more accurate quantitative analysis of organic vapor mixtures (Fig. 2. 5) [14]. In this μGC unit, a mini pump draws an air sample through a manifold-mounted pretrap and a sampler at a high flow rate. The sampler coupled with the pretrap can collect an air sample from the environment that contains a large number of background compounds. The captured VOCs from the ambient are then thermally desorbed and transferred to the microfocuser (μF) at a low flow rate by appropriate valve actuation. The μF is rapidly heated to desorb the re-trapped VOC mixtures and subsequently draw them into the two series-coupled microcolumns for separation, followed by detection by the array of nanoparticle-coated chemiresistor microsensors. The further improvement of the hybrid μGC system enabled selective determination of target analytes at sub-ppb concentrations in the presence of a complex mixture of the background VOCs (~40 components). However, this new hybrid μGC system still requires external power supplies for its operation. The need for pumping large volume of the sub-ppb air sample significantly increased the power consumption. To realize a battery-operated GC system, a more power efficient μGC pumping mechanism is required.

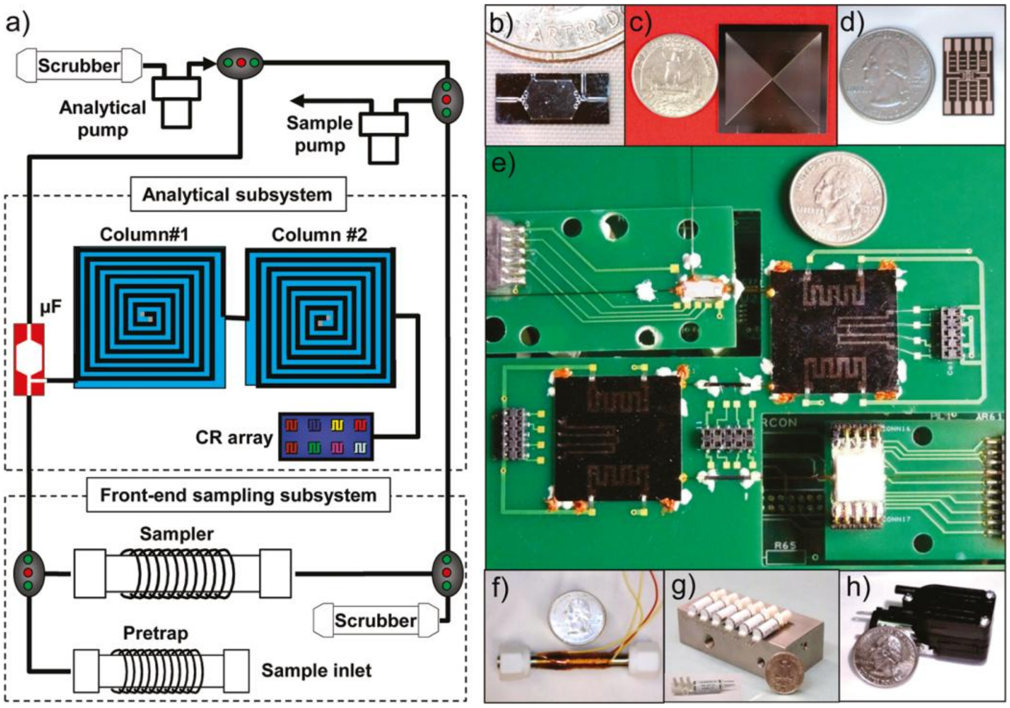

Figure 2.5. Fluidic pathway diagram of the μGC prototype and photographs of the major components: (a) schematic diagram showing fluidic pathways; (b) microfocuser (μF); (c) 3 m microcolumn; (d) microsensor array; (e) integrated microanalytical subsystem; (f) high-volume sampler/pretrap; (g) valve and vale manifold; (h) miniature diaphragm pump. [14]

2.2 Microscale Preconcentrators

An upstream preconcentrator can enhance the overall detection and separation performance of a GC system. In general, preconcentrator devices are used for two main purposes: (1) detection of a handful of specific target analytes and (2) detection of moderately complex volatile organic compounds (VOC) mixtures. When it comes to determination of the components of a moderately complex vapor mixture at parts-per-billion (ppb) concentrations, a preconcentrator is an essential component serving both as a vapor sampler and as an injector.

Conventional tube preconcentrators, or so called microtraps, comprise a stainless-steel or glass capillary tube packed with adsorbents [68-70]. For thermal desorption, electrical power is directly applied to a stainless-steel tube or to a metal wire coiled around the glass capillary tube. These devices are large in size and consume high power for heating. The performance is also limited by large dead volume and low heating

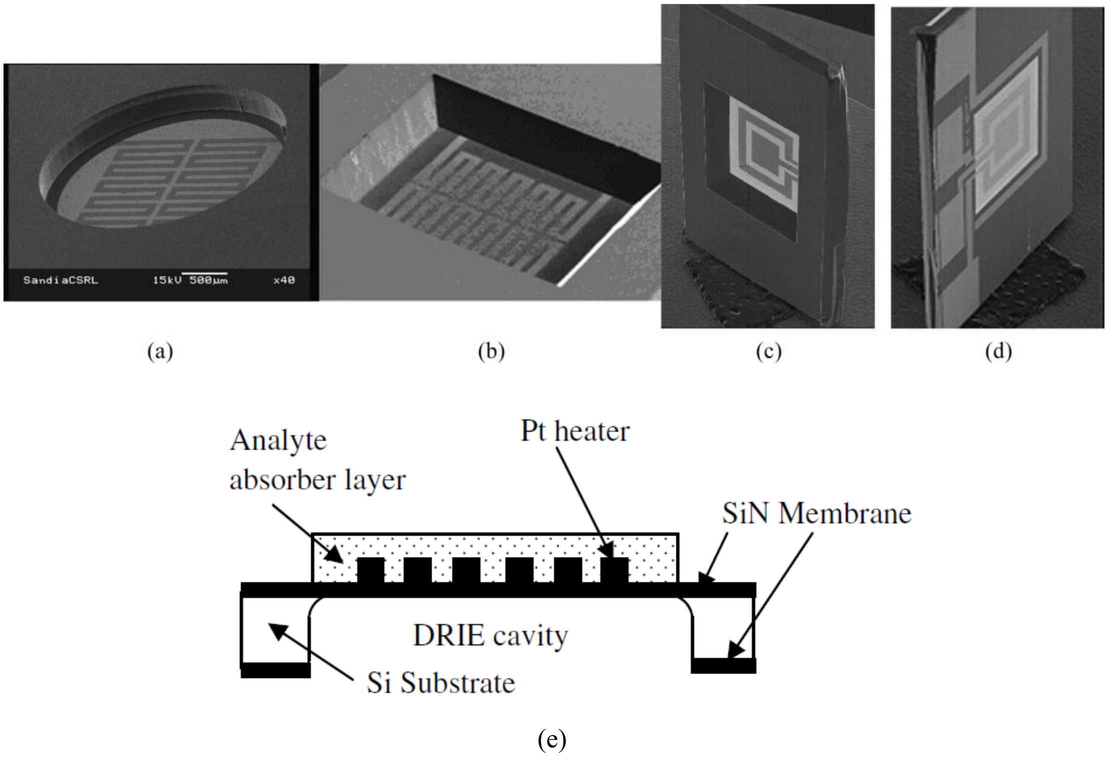

Figure 2.6. (A) Deep reactive ion-etched (DRIE) microhotplate preconcentrator. (B-D) KOH-etched microhotplate planar preconcentrators. In (B), a circular patch of adsorbent is centered on the preconcentrator. (C) and (D) show the etch side and metal side, respectively, of the same device. (E) Cross-section of a planar preconcentrator. [12, 73]

efficiency due to their large thermal mass, which results in vapor injection with a broad pulse profile. Microfabricated preconcentrators (μ-preconcentrators) using MEMS technology significantly reduce dead volume, device size, and thermal mass, thereby overcoming these limitations. The μ-preconcentrator device plays a key role as the subsystem of a microsensor through significantly improving detection sensitivity and selectivity. Its microscale dimensions also enable integration of the device with other microfabricated key components of a micro-analytical system.

Some investigators have developed μ-preconcentrators for selective detection of a limited spectrum of compound species, such as explosives or chemical warfare agents (CWA). These μ-preconcentrators typically employ a micromachined planar microhotplate and apply a highly selective adsorbent coating to the hotplate surface. Sandia National Laboratories initially developed a planar μ-preconcentrator (1997) to meet the need for rapid trace detection of specific target analytes [71]. This μ-preconcentrator was incorporated in the μChemLab® , introduced in chapter 2.1 [12]. The micro-hotplate with an integrated platinum micro-heater (Pt) was fabricated using DRIE or KOH etching (Fig. 2. 6). This planar μ-preconcentrator reached 200 ˚C from room temperature in 4 ms at a low power of 100 mW. The hotplate surface was coated with a surfactant-templated sol-gel layer with a microporous hydrophobic surface [72], which yields high adsorption selectivity. The analyte flow was drawn parallel to the device by a pump. This device successfully collected compounds of interest such as CWA soman or dimethyl methylphosphonate (DMMP) even over a background of numerous interfering compounds. With rapid thermal desorption, this planar preconcentrator injected a narrow vapor pulse to the GC column.

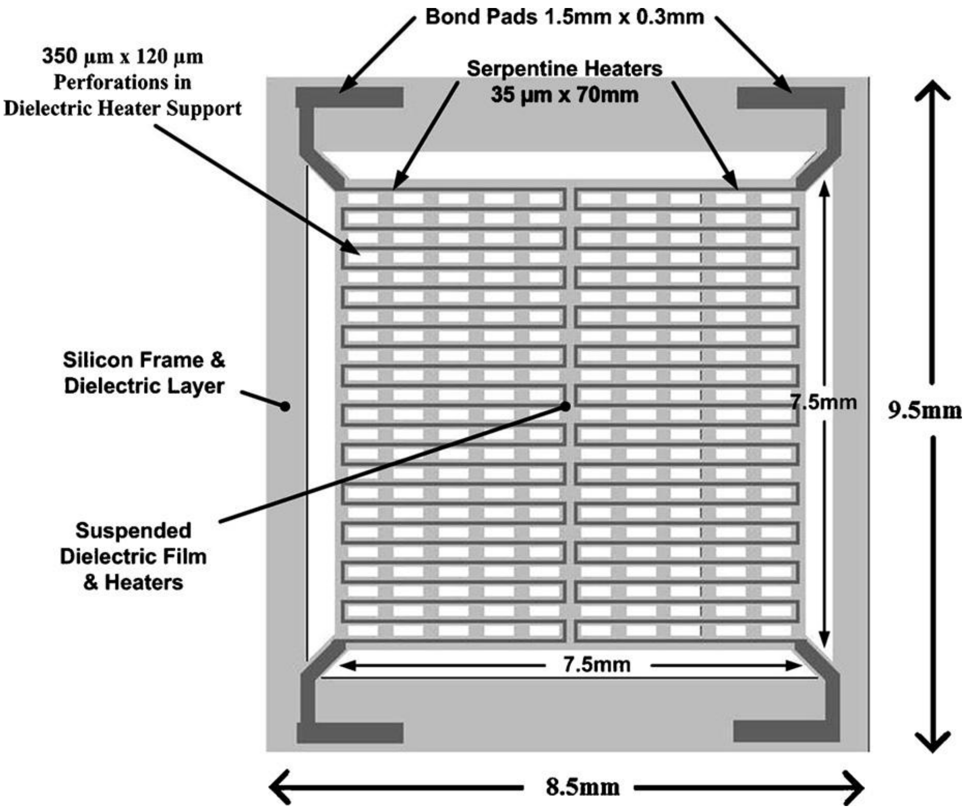

Figure 2.7. Basic preconcentrator design. [74]

The naval Research Laboratory (NRL), Washington, DC, USA, in collaboration with the University of Lousville (U of L) and George Washington University (GWU) developed a different type of μ-preconcentrator operated by the same principle. The focus of their study was on enhancing the detection threshold for explosives, namely organophosphates and nitro-aromatic compounds, using a μ-preconcentrator with an ion mobility spectrometer (IMS). These devices incorpoate arrays of perforated micro-hotplate structures coated with a polymer layer, a hyperbranched carbosilane with hexafluoroisopropanol functional group (Fig. 2. 7). This sorbent polymer is useful for collecting hydrogen bond-based explosive analytes. With the increased surface area, the flow-through hotplate design facilitates gas flow through the device at a relatively high rate , thereby improving the analyte collection capacity. The platinum micro-heater was also embedded in the perforated hotplate and achieved heating from room temperature to

120 ˚C within 0.3 s at 150 mW. The large active area of this μ-preconcentrator hotplate contributed to a larger preconcentration factor than the Sandia planar preconcentrator. Using this μ-preconcentrator, dimethyl methylphosphonate (DMMP) and explosives were successfully detected.

Preconcentration of VOCs typically requires a thick hotplate with deep cavities holding a large quantity of adsorbents [18-24]. These adsorbents comprise carbon-based granular materials of different size and allow for capturing multiple VOC species in moderately complex mixtures. The effective surface area for compound adsorption provided by these materials is much larger than that of the analyte-specific μ-preconcentrators. Thus, an adsorbent-based μ-preconcentrator can trap a large amount of VOCs with various volatilities, thereby yielding a high preconcentration factor. The VOC preconcentration process uses a diaphragm pump to draw air samples into adsorbents packed in the μ-preconcentrator. Micro-heaters integrated activates vapor thermal desorption at the μ-preconcentrator. A multi-stage microfabricated preconcentrator-focuser, one type of adsorbent-based μ-preconcentrator, was developed at The University of Michigan (Fig. 2. 8) [20]. The researchers packed three different active carbon adsorbents in a containment channel of the device. The channel comprises a bulk heater with high-aspect-ratio active elements that provide both a large heating surface area and volume capacity to retain a large amount of adsorbents. Each type of the three carbon adsorbent granules has its own effective surface area, pore size distribution, and pore morphology. Simultaneous use of these adsorbents enables the three-stage μ-preconcentrator to efficiently trap VOCs spanning a wide range of volatilities. With a doped microheater, the device was heated up to 250 ˚C within 6.5 s at a power of 1.5 W.

Using a conventional GC system connected to this device successfully analyzed 30 compounds at sub-ppm concentrations.

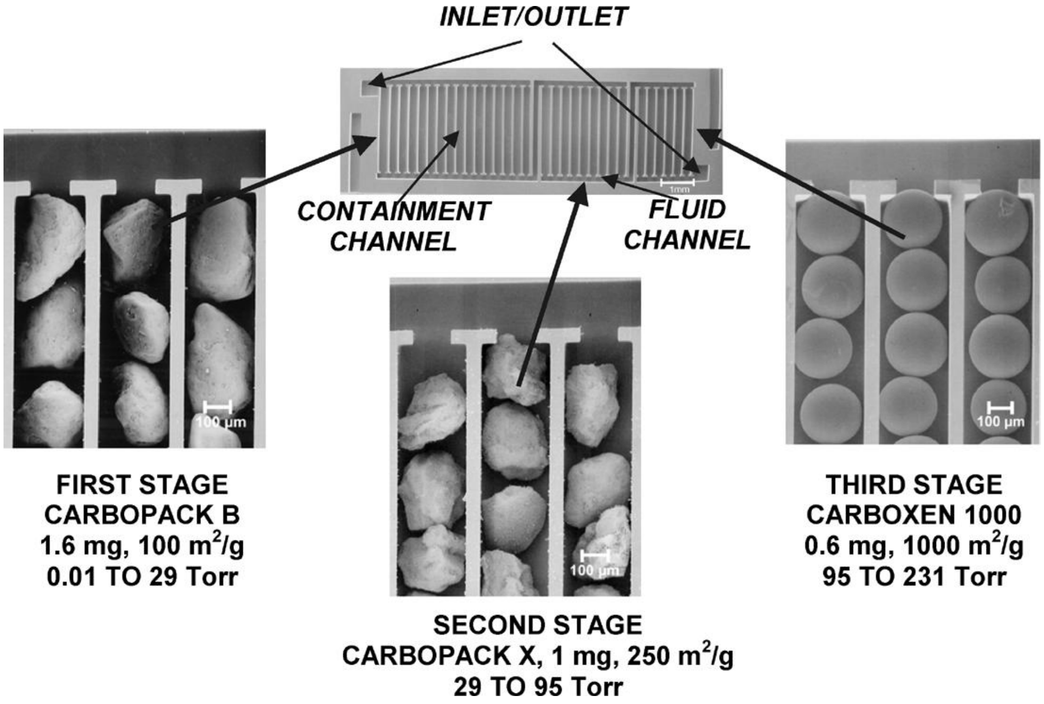

Figure 2.8. Three-stage microfabricated preconcentrator-focuser using thick microheater (upper center) packed with three carbon adsorbents to cover a wide range of compound volatilities. [20]

In recent years, μ-preconcentrators coated with a polymer layer of nano-powders were developed for concentrating a mixture of organic vapors [12, 26, 31]. An example of these devices developed in Sandia National Laboratories offered 3D adsorbent supports with a larger area in comparison to the planar counterparts and yielded a sampling time longer than 20 min for saturation. This enables collection of analytes at relatively low concentrations and allows trapping of compounds with low volatility that

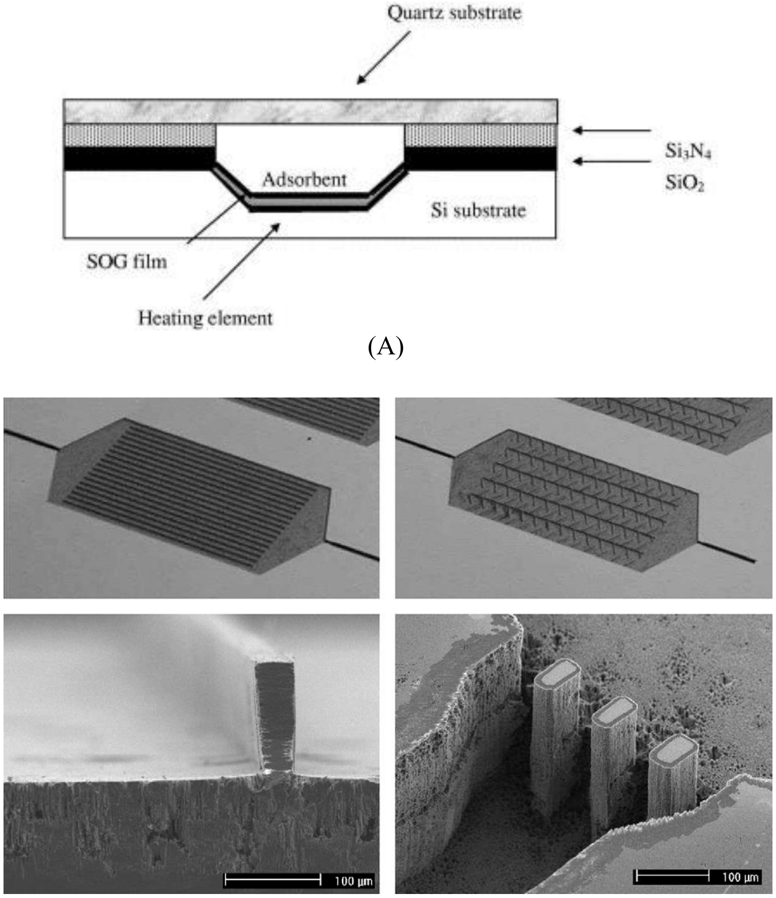

(A)

(B)

Figure 2.9. (A) Cross-section of the etched channel of the microfabricated micropreconcentrator [25]. (B) Silicon micro-channels obtained by DRIE. [26]

cannot typically be collected by the planar μ-preconcentrators. To capture the analytes, the surfaces of the 3D adsorbent supports were coated with nanoporous carbon, sol gels, and commercial packing materials. This device used 150 mW to achieve a desorption temperature of 200 ˚C and its enlarged adsorbent surface area resulted in the increase of the preconcentration by a factor of 3 than the planar preconcentrator. Other microscale preconcentrators comprised a microchannel [25] or an array of pillars [29-31, 33-35] etched using the DRIE process. A thin layer of Al deposited on the microchannel served as a heater that could reach 200 ˚C within 10 s. A polymer layer as an adsorbent was deposited on the microchannel (Fig. 2. 9A). This microchannel-based preconcentrator was tested with a stream of VOCs at ppm level concentrations. The preconcentrator containing an array of pillars significantly increased the surface areas by creating a large number of pillars in the Si-chip cavity (Fig. 2. 9B). The channel and pillars were coated with carbon nano-powder or a polymer layer (Tenax TA or PDMS). The pillar array and channel structures could be designed to increase the adsorption capability and ensure the smoothed sample flow to avoid gas residuals in the cavity. Although these devices successfully achieved a high preconcentration factor for VOCs, further improvements are necessary to detect low- and sub-ppb level concentrations of vapor sample.

Overall, regardless of preconcentrator type or group, all the existing μ-preconcentrators require active pumping to draw the vapor sample into the adsorbents. The power required for pumping in a μGC system becomes more significant along with the increase of the required sample volume and analysis time depending on needs. From the studies reviewed here, it is clear that the preconcentration capability and the rapid thermal desorption of a preconcentrator with low power play key roles together in GC analyte detection. These preconcentrator studies exemplify the need for a MEMS-based high performance preconcentrator device with low power and for an innovative approach to developing such a device.

CHAPTER III

PASSIVE VAPOR SAMPLING OF MICROFABRICATED PRECONCENTRATOR/INJECTOR

3.1 Introduction

Gas chromatographic microsystems (μGCs) offer great potential for analyzing mixtures of volatile organic compounds (VOCs) in miniature packages suitable for personal exposure monitoring, point-of-care medical diagnostics, explosive detection, and other applications. Examples of functional prototype μGCs, which we define as comprising, at a minimum, a preconcentrator or a sample injector, separation column, and detector, all of which are microfabricated from Si, glass, or other suitable materials, have appeared in recent years [8, 10-14].

Often, it is necessary to concentrate VOC(s) of interest prior to analysis because most detectors lack the inherent sensitivity required to attain the low detection limits demanded in many applications. For this reason, μGC injectors that incorporate a preconcentration function are common. Numerous reports have appeared on microfabricated preconcentrators, which typically consist of a micromachined device with an internal cavity packed or lined with an adsorbent material [18-20, 28, 31, 74-76].

The VOCs in an air sample, drawn through the device by means of a small pump, are trapped on the surface of the (typically) high-surface-area solid adsorbent. Subsequent rapid heating leads to desorption into a carrier gas flowing at a lower rate, which leads to an enhancement in concentration of the VOCs that are passed downstream to a separation microcolumn and/or a microsensor or microsensor array.

One important factor affecting device performance is the dynamic adsorption capacity, which is related to the volatility and functionality of the VOC(s), the mass and specific surface area of the adsorbent (and therefore the size/mass of the device), and the flow rate of the air sample being drawn through the device. Other important performance factors are the desorption rate, efficiency, and bandwidth, which are also related to the volatility and functionality of the VOC(s), the mass and surface area of the adsorbent, and the desorption/injection flow rate, as well as the maximum temperature and rate at which the device is heated. Power requirements also come into play, and often have a significant influence on device design.

As progress is made toward smaller and more power efficient μGC components, the power required for pumping becomes more significant. Although a few reports on low-power, microfabricated pumps used in μGC separations have appeared [8, 9], most μGC systems rely on commercial mini-pumps, which dissipate power on the order of 1-4 W [8, 10-17]; this is comparable to the power required for heating state-of-the-art microscale preconcentrators and separation columns [18, 20, 39, 75, 77]. Depending on the required sample volume and the time of analysis, the energy for pumping may exceed that for the other power-intensive components.

Passive diffusional samplers were developed nearly 40 years ago for sampling the breathing zone of workers potentially exposed to VOCs [78], and they are used routinely in environmental and occupational exposure monitoring [79-83]. Most commercial passive VOC samplers are small (*i.e.*, a few cm^3), employ carbon based trapping materials, and have sampling rates of ~3 to 30 mL/min. Following the sample collection period, typically 4-24 h, the sampler is returned to the laboratory for solvent or thermal desorption followed by conventional GC analysis. Although a miniaturized passive sampler has been reported [84, 85], there have been no reports on a microfabricated passive sampler with or without an integral heater.

In this chapter, we report on a microfabricated passive preconcentrator-injector (μPPI) that captures vapors from the air at a known rate by diffusion, without a pump. The μPPI has a top layer with a grid of precisely defined micrometer-scale channels through which VOCs diffuse, and a bottom layer with a thermally isolated, adsorbent packed cavity, tapered inlet/outlet sections with fluidic ports, and an integrated heater on the underside of the cavity floor for desorbing and injecting captured VOCs downstream upon completion of a specified sampling period. The next section provides a brief overview of diffusional sampling theory and the scaling laws relevant to miniaturization. A general description of the μPPI is then presented, followed by the detailed design specifications, the fabrication process, and methods used for testing performance. The power dissipation and response time of the device heating function along with results of initial gravimetric tests of the mass uptake rate using toluene as the test vapor are then briefly summarized. Finally, chamber tests showing the operation of the μPPI are presented, with an emphasis on documenting the sampling rate, capacity, and desorption (injection) capture efficiency of toluene as a function of flow rate.

3.2 Background and Theory of Passive Sampling

Passive samplers rely on the diffusion of vapors down a concentration gradient created within the device by placing an adsorbent trap at the end of a stagnant chamber that is open to the ambient. Assuming that the air concentration is effectively zero at the surface of the trap, the diffusional sampling rate is given by the following equation, derived from Fick's law of diffusion [86]:

$$S = \frac{DA}{L} = \frac{m}{Ct} \tag{3.1}$$

where D is the diffusion coefficient of the vapor (cm^2/s), A is the cross-sectional area of the sampler (cm^2), L is the length of the diffusion path within the sampler (cm), C is the ambient vapor concentration (μg/cm^3), and m is the mass of vapor captured (μg) over the sampling time, t (s).

In the absence of turbulence, S is directly proportional to A and inversely proportional to L, and it is theoretically possible to scale down the size of the sampler while keeping S constant by maintaining a constant L/A ratio. In one sequence of articles, Gonzalez and Levine [84, 85] described a miniature passive sampler consisting of a cylindrical steel thimble, with a charcoal-pad trap and wire mesh cap. The dimensions of the device, A = 32 mm^2 and L = 3.8 mm, resulted in a sampling rate for benzene of 2.8 mL/min, which is relatively low due to the small A/L ratio of 8.4. This sampling rate could be maintained for 30 min at a challenge concentration of ~0.8 ppm of benzene, after which it started to taper off due to the limited capacity of the adsorbent.

At low vapor concentrations and sub-monolayer coverage of the adsorption sites on the trapping material, the amount of vapor adsorbed to the surface of a granular adsorbent at equilibrium is proportional to the air concentration of the vapor. It can be expressed as the equilibrium adsorption capacity, W_e, which is the ratio of the mass of adsorbed vapor to the mass of adsorbent material [87]. As a monolayer is approached, W_e no longer increases in proportion to the air concentration of the vapor, and at a full monolayer W_e reaches a constant value. In the sub-monolayer regime, the adsorbent serves as an effective vapor trap and the concentration of vapor near the surface can be assumed to be close to zero, so that the sampling rate is governed by equation (3.1). As the sites on the adsorbent gradually become occupied, the trapping efficiency is expected to decrease along with the sampling rate. The point at which the sampling rate decreases significantly is a function of time and the vapor concentration, and it defines the effective capacity or service life, as explored below.

Once the sampling period is concluded it is necessary to desorb the captured vapors for analysis. For a microfabricated device, this could be done thermally by heating the adsorbent *in situ* and drawing the released VOCs to downstream components by means of a small pump. This was the approach taken for the μPPI described here. Designing the device for power-efficient heating is therefore important. In addition, sufficient suction flow velocity must be provided to overcome the back-diffusion velocity imparted to the VOCs by the heating process so they do not escape through the inlet aperture. The material properties, fluidic paths, dimensional constraints, heat transfer efficiency, and velocity profiles related to these design and operation variables must all be accounted for in order to realize a variable microscale device suitable for use in the quantitative analysis of VOCs.

3.3 General Description

Fig. 3.1 shows a block diagram of a hypothetical microscale GC (μGC) system that incorporates the μPPI as the vapor capture device. A focuser is included because the (pump-driven) flow rate required for delivering desorbed samples from the μPPI to the microcolumn is expected (see below) to exceed the maximum flow rate typically used in μGC separations (*i.e.*, <5 mL/min). Although splitting the flow downstream from the μPPI could be considered, a properly configured focuser can function as an efficient

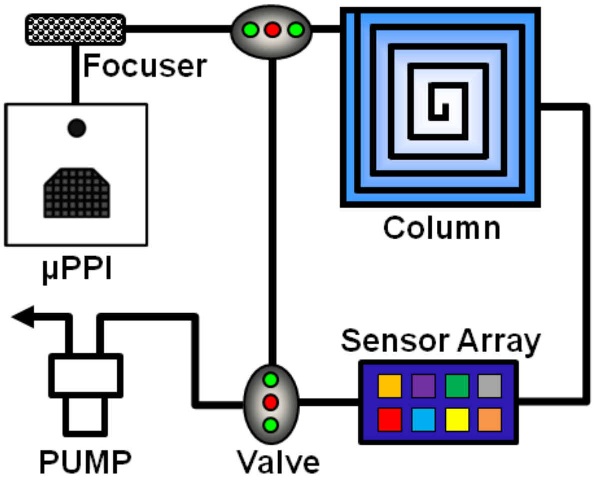

Figure 3.1. Conceptual layout diagram of a microscale gas chromatograph (μGC) incorporating the μPPI wherein vapor samples would be collected passively, transferred to a (micro)focuser, injected to the microcolumn for separation, and detected by an array of microsensors.

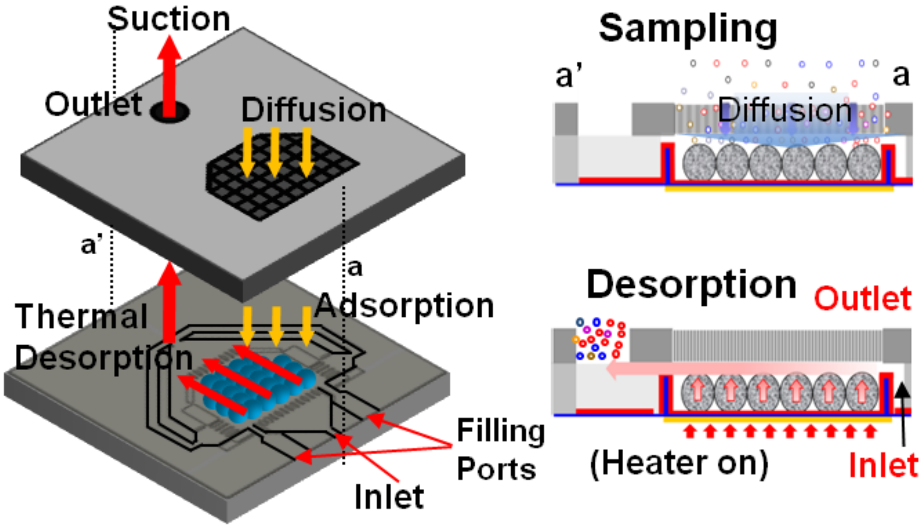

Figure 3.2. Exploded view conceptual diagram of µPPI and side views showing the diffusional sampling and thermal desorption processes.

VOC trap at relatively high flow rates and then be heated rapidly to inject a VOC sample at a (lower) flow rate more compatible with efficient chromatographic separations [14]. The (entire) injected mixture of VOCs would then be separated in the microcolumn and detected by an array of microsensors [10, 14].

Fig. 3.2 shows an exploded-view illustration of the µPPI along with side-view illustrations of the sampling and desorption processes, and Fig. 3.3 provides more detailed diagrams and images of selected device features. The top layer contains a grid of square diffusion channels through which vapors pass into the device (Fig. 3.3A). This layer also has a through-hole used for fluidic interconnection to downstream components upon thermal desorption/injection of capture VOC samples. The bottom layer contains a cavity with tapered entrance/exit pathways on two sides and a set of walls and pillar structures to retain the adsorbent granules in its central region (Fig. 3.3B). The area of

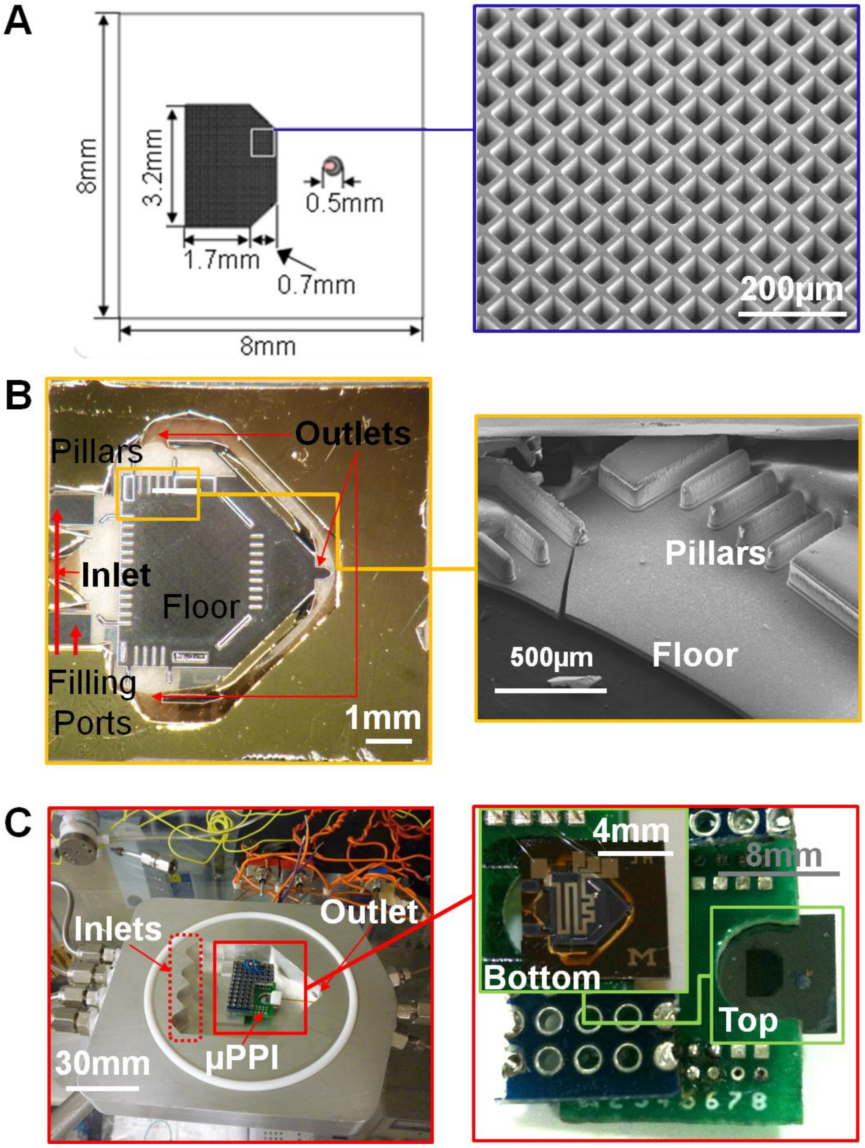

Figure 3.3. Images of (A) top layer, (B) bottom layer, and (C) assembled μPPI system in the exposure chamber. The fabricated top layer is shown in (A). The adsorbents (Carbopack X) are packed through the filling ports (left-hand image of (B)) after bonding the top layer and the bottom layer. The right-hand image of (B) shows the 3D SEM image of the bottom layer. The adsorbents are confined by pillars after packing. In (C) the packaged PPI is shown mounted in the exposure chamber.

this central region matches that of the diffusion-channel grid in the top layer. The (desorption) inlet and adsorbent filling ports are located at one end of the cavity, and there are two internal side ports that help to distribute the airflow during thermal desorption. The underside of the membrane floor of the cavity has a meander-line metal thin-film heater and a resistance temperature device (RTD) for thermal desorption (Fig. 3.3C). The desorbed vapors are drawn through the outlet port and injected onto the downstream focuser.

3.4 Device Design and Expected Performance

The top layer Si-substrate thickness, which defines the diffusional path length through the grids, L_1, was set at 200 μm. The aperture of each element in the diffusion-channel grid was set at 54 × 54 μm (grid walls = 12 μm wide). The grid can be viewed as a rectangular subsection with dimensions of 3.2 mm × 1.7 mm and a trapezoidal subsection with dimension of 3.2 mm (long side), 1.8 mm (short side), and 0.7 mm (width), the sum of which contain 1530 channels with an overall area, A_1, of 4.5 mm^2.

Note that the need for a turbulence barrier arises if $L/d < 2.5$, where d is the diameter of the sampling aperture [88]. Below this value of L/d, the path length can be effectively reduced in windy environments by eddy currents created at the entrance to the sampler, to an extent that increases the sampling rate significantly. For an effective grid aperture diameter of 61 μm (derived from a circle having the same area as each grid-aperture square), the value of L_1/d for each channel in the μPPI is 3.3, and the effects of turbulence should be negligible.

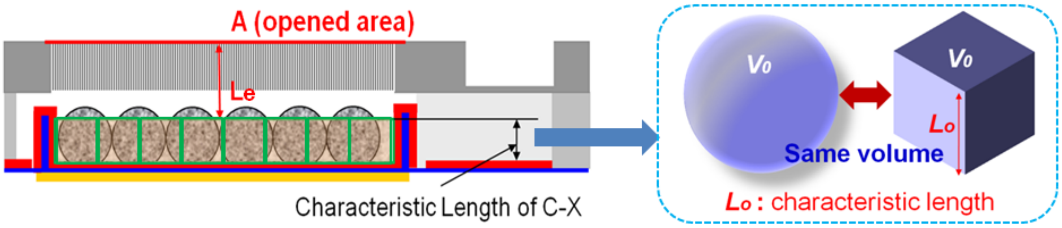

Figure 3.4. Determining the sampling rate: Concept of characteristic length.

The cavity in the bottom layer was designed with a small headspace volume above the adsorbent layer to facilitate adsorbent loading and the subsequent capture of desorbed vapors. Since vapors must diffuse through this gap, it affects the sampling rate. For the selected bottom layer Si-substrate thickness of 250 μm, the cavity floor thickness was limited to 24 μm (*via* boron-doping level, considering mechanical strength, thermal isolation, and heat transfer as discussed below) to give a cavity depth of 226 μm. The adsorbent granules were sieved to a nominal average diameter of 200 μm. Assuming spherical particles, the characteristic length (thickness) for the single-layer adsorbent bed is 161 μm in Fig. 3.4. The effective diffusion channel length $L_e = L_1 + L_2$ is shown in Fig. 3.4. Here, the effective diffusion channel L_e is defined as the distance between the entrance of the diffusion channel and the top surface of the C-X particle, for which we assume a cubic shape of equivalent volume. We define the height of the cube as the characteristic length of the C-X particle: L_0. The value of L_0 is determined from the average diameter of the C-X particle. The experimentally observed average diameter of the C-X particle is typically 200 μm. The corresponding characteristic length is L_0 = 161 μm. As such, the effective diffusion length $L_e = L_1 + L_2$ = 265 μm is determined by subtracting L_0 = 161 μm from the distance between the cavity bottom and the external

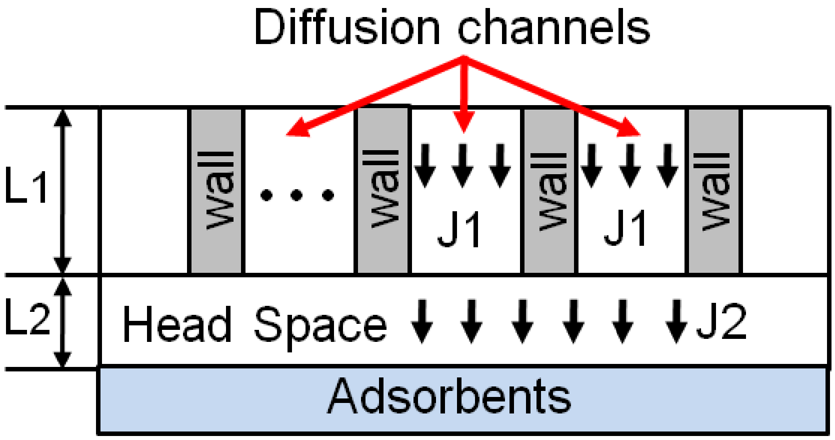

Figure 3.5. Cross-sectional view of the μPPI structure consisting of diffusion channel array, head space and absorbent layer.

surface of the top layer (= 426 μm). This results in an effective diffusional path length through the headspace, L_2, of 65 μm. The cross-sectional area of the headspace, A_2, is 6.7 mm^2 (note: A_2 is larger than A_1 because of the lack of any grid walls in the headspace).

Given the serial flow resistance through the grid and then the headspace (note: diffusion into the interstitial spaces between particles is ignored), the effective sampling rate, S_e, can be estimated. Figure 3.5 shows the cross-sectional view of the μPPI structure consisting of diffusion channel array, head space and absorbent layer. From the 1D diffusion equation and Fick's law, the sampling rate for a diffusion channel is derived as:

$$j = -D\frac{dC}{dZ} = D\frac{\Delta C}{L} = \frac{M}{A \cdot t} \tag{3. 2}$$

where j is the vapor flux, D is the vapor diffusion coefficient, ΔC is the concentration difference between two positions along the diffusion path, L is the diffusion length, M is the vapor mass (or alternatively, the number of molecules), A is the cross sectional area normal to the diffusion direction, t is the sampling period. It follows that the sampling rate S is given by

$$S = D\frac{A}{L} = \frac{M}{\Delta C \cdot t} \tag{3. 3}$$

From equation (3. 2) and equation (3. 3), the mass flow rate J is expressed as:

$$J = (\Delta C)S \tag{3. 4}$$

The vapor flow driven by diffusion takes place inside the device through two regions: (a) the diffusion channel layer and (b) the head space. Applying the mass conservation rule to the above two regions, we obtain the following equations.

$$J = (C_1 - C_i)S_1 = (C_i - C_2)S_2 \equiv \left(C_1 - C_2\right)S_e \tag{3. 5}$$

where C_1 is the vapor concentration at the top surface of the diffusion channel layer of length L_1 and total diffusion cross sectional area A_1, C_i is the vapor concentration at the interface between the diffusion channel layer and the head space of height L_2 and cross sectional area A_2, C_2 is the concentration at the adsorbent surface, $S_1 = D\frac{A_1}{L_1}$ is the sample flow rate at the diffusion channel layer, $S_2 = D\frac{A_2}{L_2}$ is the sample flow rate at the head space, and S_e is the overall effective sample flow rate for the entire diffusion length (L_1 + L_2). From equation (3. 5), we obtain

$$S_e = \frac{S_1 S_2}{S_1 + S_2} = D\frac{A_1 A_2}{A_1 L_2 + A_2 L_1} \tag{3. 6}$$

The sampling rate for each region can be calculated from equation (3. 1) as S_1 = 11.4 mL/min and S_2 = 52.1 mL/min are achieved. A_1 is 4.46 mm^2 and the cross sectional area (A_2) in the headspace increases by 49%. Using the values of the variables given above and a value of D = 0.0849 cm^2/sec (25 ˚C) for toluene [86], equation (3. 6) yields an expected sampling rate of 9.3 mL/min for the μPPI.

The graphitized carbon Carbopack X (C-X) was chosen as the adsorbent material on the basis of previous work indicating that it would have a high affinity for toluene (and other similarly volatile VOCs), which was used as the test vapor, while also allowing efficient thermal desorption [70, 89]. this material also has a low affinity for water vapor. The amount of C-X that could be packed into the device was estimated to be about 680 μg on the basis of the cavity volume and the published packing density for 60/80 mesh C-X of 0.41 g/cm^3 [90], and was subsequently determined gravimetrically to be 750 μg for the sieved C-X used in the actual device. Since the W_e value for toluene at 1 ppm on C-X is 2800 μg/g, the capacity of the device is 2.1 μg of toluene. At 9.3 mL/min, saturation would be expected after ~60 min of exposure. Since S_e is expected to decline prior to this point, the maximum time between successive thermal desorption/regeneration cycles should be somewhat less than this value.

The primary design factors considered with respect to the desorption of VOCs from the μPPI were the heating rate and power, and the air velocity required to capture (inject) the desorbed vapors. A target maximum desorption temperature of 250-300 ˚C was chosen on the basis of previous work [19, 70, 89]. The membrane floor thickness of 24 μm for the cavity represents a compromise between minimizing thermal mass, which promotes rapid, low-power heating, and maximizing mechanical rigidity, which reduces stress-induced deflection and increases the robustness of the overall structure. Although the high thermal conductivity of the p-doped Si (~150 W/m·K) promotes the rapid distribution of heat from the underlying heater to the entire adsorbent bed, it demands thermal isolation from the surrounding substrate. Therefore, a 15 μm layer of SiON (thermal conductivity = 5 W/m·K) was deposited beneath the cavity floor membrane and the perimeter of the Si membrane was removed so that the cavity floor was suspended on the SiON. A combination of lateral wall structures and arrays of pillars was required at the edges of the Si membrane to retain the adsorbent within the heated region; in the case of the latter there was also a need to allow airflow to pass with minimal flow resistance. A Ti/Pt meander-line heater was then patterned on the underside of the SiON to enable the uniform heating of the cavity and precise, programmable temperature control with low power. Thermal modeling, which accounted for the thermal contact resistance of the adsorbent layer and the convective cooling from the airflow during thermal desorption, indicated that ~1 W of power would raise the membrane temperature to 300 ˚C in 3 s and that the adsorbent bed temperature would be within the targeted range.

Turning now to the fluidic factors, the first issue considered was the temperature dependence of D, which varies as the square of the temperature ratio, T_2/T_1, where T_1 is the reference temperature and T_2 is the desorption temperature [86]. For toluene, this leads to a D value of 0.31 cm^2/s at 300 ˚C. Assuming the flux out of the device is governed entirely by back diffusion, the expected volumetric flow rate upward during desorption, by equation (3. 6), is 34 mL/min, which corresponds to a linear velocity through the headspace of 0.1 m/s.

The suction flow velocity required by the downstream pump to avoid loss of toluene through the diffusion-channel grid was estimated using computational fluid dynamics (CFD) analysis (CFD-ACE, ESI Group, Paris, France) [91]. The CFD analysis considered the cavity dimensions, the inlet/outlet port locations and the transition geometries, and initially assumed that the entering flow came from the inlet and the grids and the existing flow went only through the outlet port (*i.e.*, the side ports were not considered).

Simulated flow patterns and trajectories were examined as a function of applied suction pressure, taking into account both the forced convection by the air flow and the back-diffusion of the desorbed vapor. Criteria used to determine performance were the presence of any points where the vertical (z-direction) velocity was positive at an elevation corresponding to the top surface of the grid and the number and locations of stagnant loci or vortices indicative of low fluid motion within the interior cavity zone. To keep the computational task reasonable, the presence of the adsorbent granules was ignored (note: it can be shown that the empty cavity represents a more conservative constraint in terms of preventing the vapor loss due to the back diffusion).

Upon heating the device membrane, vapor molecules desorbed from the adsorbent materials may escape through the diffusion channels due to the developed concentration gradient in the vertical direction. To understand how the carrier gas flow dynamics affects the sample losses during the suction process, we performed CFD analysis for the designed device (Fig. 3. 6). The CFD analysis for the cavity design of the μPPI shows all

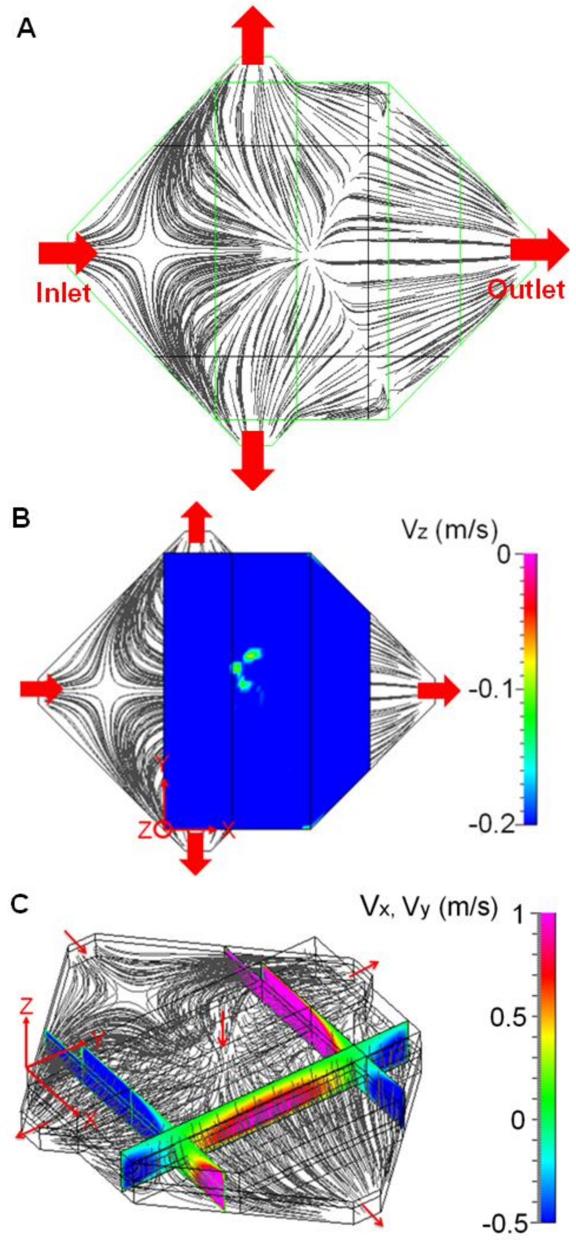

Figure 3.6. (A) Velocity field of all vapors flowing inside the cavity from the inlet and the top diffusion channels divided into three regions close to the outlets. (B) Computational fluid dynamics (CFD) analysis of the vertical (z-direction) velocity of the carrier gas flow at the top surface of the diffusion channels (colored) under the suction pressure at the outlet. (C) Flow patterns inside the device cavity and distribution of velocity magnitude on cross sections normal to the outlet flows.

thermally desorbed vapors migrate to the outlets without escaping through the diffusion channels. The red arrows indicate the flow direction at the inlets (including diffusion channels) and outlets. The CFD model numerically solves the full Navier-Stokes equations assuming Newtonian incompressible flow in the cavity chamber of the μPPI. It predicts the relatively complex flow pattern of the vapor molecules driven by a carrier gas in either the laminar or turbulent regime. The heater temperature and the suction pressure at the outlet are both programmable and controllable. Thus, all boundary conditions are determined according to the operational conditions of our choice. The initial pressure of the inlet is set at the ambient pressure here. The pressure drop at the outlet, provided by a mini diaphragm pump, is assumed to be 15kPa. The ambient temperature and the temperature of the cavity bottom upon the desorption process are set at 25℃ and 300℃, respectively.

In our CFD analysis, we considered the worst condition that would yield the maximum vapor loss and the lowest vapor flow rate at a given pressure drop. The condition is realized when the analysis assumes an empty cavity with no adsorbents, which is verified by the model in Fig. 3.13. In the real device setting, the volume of the adsorbents filling the cavity reduces the effective cross-sectional area through which the vapor is horizontally carried during the sample injection process. This real condition results in higher horizontal (*x*-direction) vapor velocity, hence less vapor losses at the same pressure drop as used in the analysis. Assuming a sphere shape for the adsorbent beads, the vapor desorption rate of 34.0 mL/min calculated for the overall cavity area using equation (3. 1) and equation (3. 6) in the main text is converted to a vapor linear velocity of 0.1 m/sec in the radial direction of the adsorbent sphere. The average desorption linear velocity projected in the vertical (z-) direction is 0.07 m/sec and used for the boundary condition in the vertical direction with adsorbents packed. To be conservative in our prediction, we apply a vapor desorption linear velocity of 0.12 m/sec in the vertical direction as the boundary condition at the bottom chamber floor. Figure 3.6 shows the prediction of the net vertical (z-direction) velocity of the carrier gas containing the vapor molecules, accounting for the vapor counter flow by diffusion. Our simulation indicates that the carrier gas will pass through the entire open area of the diffusion channel grid and be collected by the outlets without vapor losses. It also shows no vortices and stagnation points inside the chamber. A suction flow rate of 60 mL/min ensures that the z-direction velocities of the carrier gas have all negative values over the whole area at the top surface of the diffusion channel grid under. Under this condition, it is expected that the desorbed vapor molecules are effectively carried by the gas and collected. Therefore, we employ the 3-outlet design as the optimal passive preconcentrator design in our study.

CFD simulations of numerous possible design variations and flow conditions revealed the importance of using tapered inlet and outlet transitions to promote the uniformity of the flow profile across the width of the cavity, and adding sideport exit paths toward the upstream end of the cavity to ensure that the vertical velocity remained negative in this region. A minimum pressure drop of 15 kPa between the inlet and outlet was required to avoid loss of vapor through the top-layer grid and to eliminate vapor stagnation in the cavity. This pressure drop translates into a minimum flow rate of ~60 mL/min (1.25 m/s).

3.5 Experimental

This chapter discusses the fabrication and experimental methods for the designed micro-device. The μPPI fabrication was performed at the Lurie Nanofabrication Facility (LNF) at the University of Michigan. Experimental methods include measurement of VOC sampling of the μPPI using the TGA and the exposure chamber.

3.5.1 Microfabrication and Assembly

Wafers of p-doped <100> Si, 200 μm and 250 μm thick, were used to fabricate the top and bottom layer of the μPPI, respectively. The former was double-side polished and the latter was single side polished. In fabricating the top layer (Fig. 3.7A), a Cr/Au (10/450 nm) layer was first evaporated onto the backside and the grid wall pattern was defined with photoresist. Au was then electroplated to a thickness of 3-4 μm on the perimeter of the backside of the top layer for subsequent eutectic bonding. After stripping, a new photoresist layer was patterned to expose the grid apertures and the thin Cr/Au layers were removed by wet etching. Through-wafer deep reactive ion etching (DRIE) was used to create the diffusion grid and the outlet port.

The bottom layer fabrication (Fig. 3.7B) started with the growth of a 15 μm thick thermal oxide layer on the backside of the wafer, which was then patterned to permit formation of the pillars (height: 170-190 μm; width: 90 μm; spacing: 100 μm), the lateral walls (height: 170-190 μm; width: 130-440 μm), the side ports (width: 780 μm), and the side-port flow channels (height: 250 μm; width: 260 μm) by DRIE. After that, the oxide

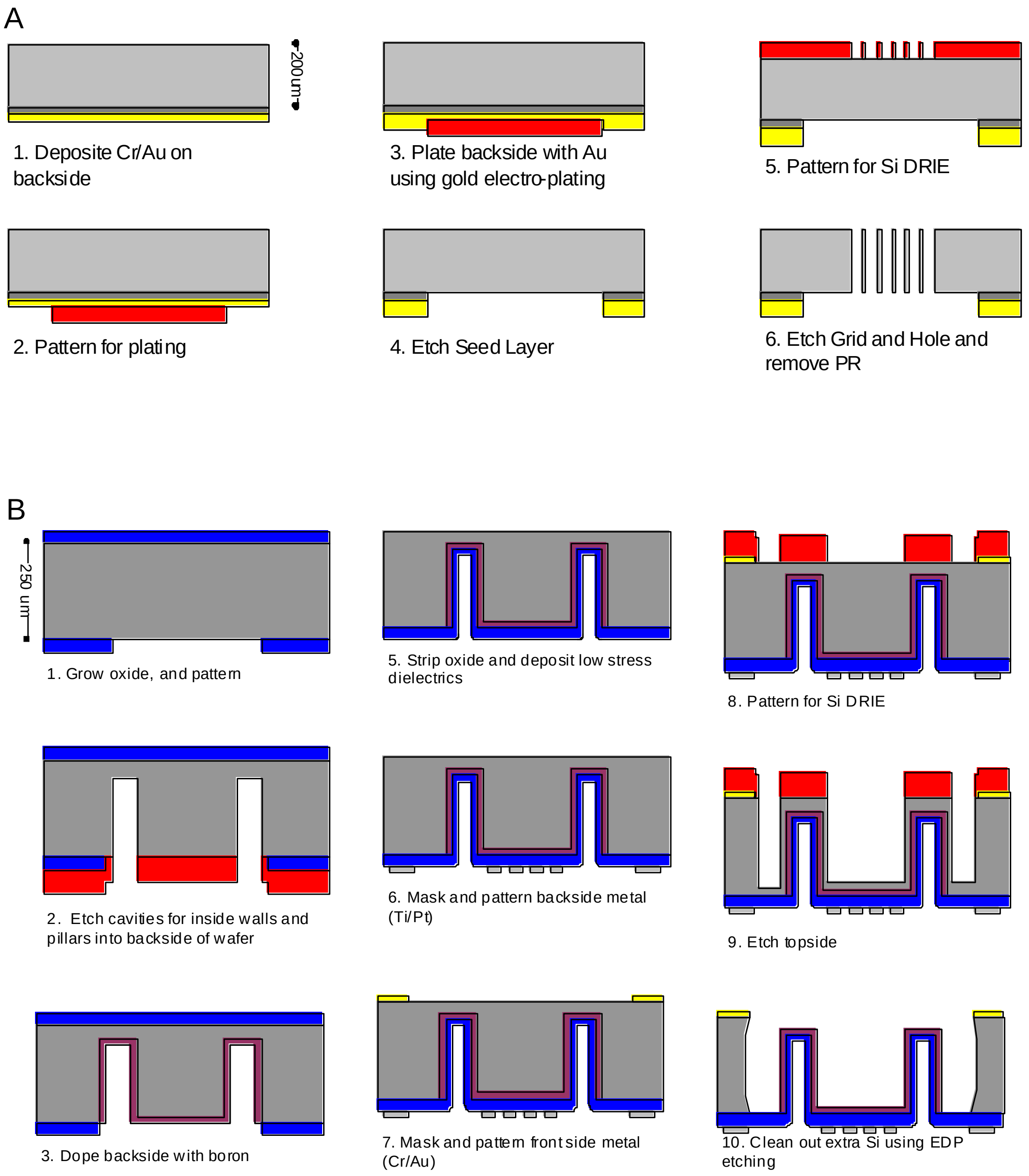

Figure 3.7. (A) Top layer and (B) Bottom Layer Fabrication processes

layer was stripped. Then, a 24 μm thick boron-doped Si layer was formed on the backside of the cavity floor by a standard boron diffusion process for ~17 h. A 15 μm thick low-stress SiON layer was then deposited on the backside by plasma-enhanced chemical vapor deposition (PECVD). The Ti/Pt meander-line microheater and the resistive temperature sensor were then patterned and deposited on the oxy-nitride layer by a lift-off process, followed by annealing at 400 ˚C to relieve thermal stress. A Ti/Au mask layer was then deposited and patterned on the front side of the bottom layer for eutectic bonding and DRIE was used to complete the formation of the cavity-floor membrane, filling ports, inlet, and pillars. Finally, etching in ethylenediamine pyrocatechol (EDP) removed residual updoped Si.

Top- and bottom-layer structures were diced, aligned, and temporarily fixed to each other using a small amount of epoxy (Durapot 865, Cotronics, NY). This was followed by eutectic bonding of the two layers at 330 ˚C for 12 hours. The device was fixed to a set of pins on a small section of a printed circuit board (PCB) and the on-chip heater and the RTD on the bottom layer were wire bonded to traces on the PCB. A capillary connector with right-angle circular channels was fashioned from a piece of Macor® and was bonded to the outlet port in the top layer using epoxy (Duraseal 1531, Cotronics, Brooklyn, NY), and then a section of deactivated fused-silica capillary (i.d.: 530 μm) was inserted and sealed with the same epoxy.

A sample of 60/80 mesh C-X (specific surface area = 250 m^2/g, Supelco, Belafonte, PA) was sieved to isolate granules in the size range of 180-212 μm, and then loaded into the device cavity *via* the loading ports under gentle suction pressure. Visual inspection was used to confirm when a single layer that filled the entire cavity had been achieved. Pre- and post-weighing of the device on an electronic balance indicated that ~750 μg of C-X was loaded. Figure 3C shows the packaged and mounted device.

3.5.2 Performance Testing

Test atmospheres of toluene vapor were generated dynamically by passing N_2 through a fritted bubbler containing the liquid solvent and then diluting in a metered flow of dry air. A portion of the flow was diverted every 5 min to a gas sampling loop mounted on a bench scale GC equipped with a flame ionization detector (FID) (Model 6890a, Agilent, Wilmington, DE) for confirmation of the toluene concentration. The FID was calibrated by auto-sampler syringe injections of liquid standards of toluene in CS_2. Injected masses ranged from 0.4 ng to 2.2 μg and the plot of peak area *vs*. mass injected (*i.e.*, calibration curve) was linear ($r^2 > 0.999$).

As part of a preliminary assessment of μPPI performance, the device was placed in the weighing chamber of a thermogravimetric analyzer (TGA) (Pyris 1, Perkin Elmer, Waltham, MA) and exposed to toluene. The μPPI was suspended from the weighing pan by a fine wire, and the N_2 purge line normally used to maintain an inert atmosphere within the semi-enclosed chamber was modified to permit switching from N_2 to a test atmosphere of toluene in N_2. The mass of the μPPI was recorded as a function of time to monitor toluene uptake in triplicate.

To characterize the sampling rate and desorption/injection efficiency of the device more thoroughly, the PCB-mounted μPPI was placed inside a custom-made 25-mL environmental chamber (Figure 3.3C) in the system shown schematically in Figure 3.8. A flow divider at the inlet to the chamber distributed the incoming flow (0.1 L/min) evenly over the raised device mounting pedestal, and a portion of the exhaust flow was directed to a 250-μL sample loop mounted on a 6-port valve. The loop was alternately filled and

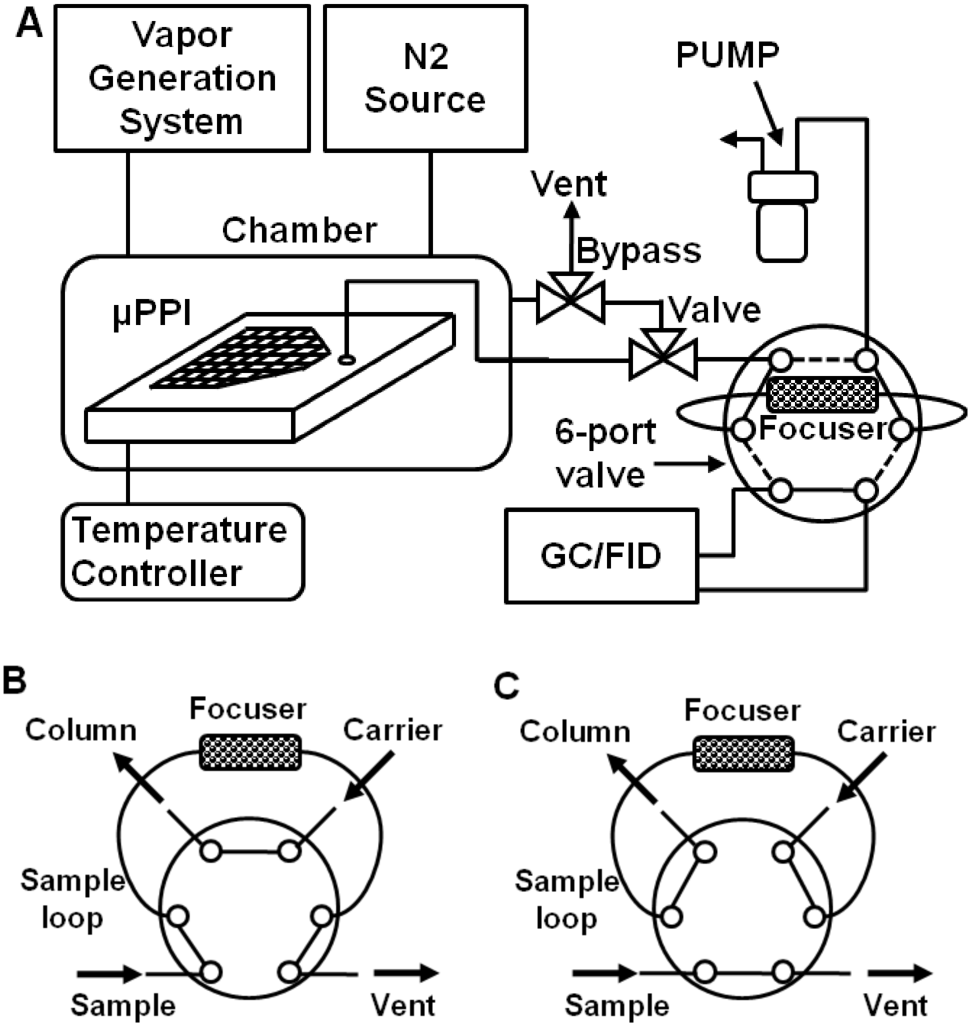

Figure 3.8. (A) Schematic of the test setup used to characterize the sampling rate and the capture/transfer efficiency of the μPPI during thermal desorption. (B) The vapor sample is transferred from the μPPI to the focuser. (C) When the valve is switched, the sample in the focuser is thermally injected onto the column.

then purged/injected into the GC inlet port (using a separate N_2 tank) in order to verify the test-atmosphere concentration (Figure 3. 8A). Following collection of a sample by the μPPI, the loop was replaced with a C-X-packed focuser (described immediately below), the upstream end of which was connected to the Macor® connector on the outlet port of the μPPI via deactivated fused-silica capillary (sealed within one of the chamber exit lines), and the downstream end of which was connected via the 6-port valve, to a mini-pump (N86KNDCB, KNF Neuberger, Trenton, NJ) (Fig. 3.8B). During thermal desorption of the μPPI sample, the mini-pump drew N_2 through the device and then the focuser. The valve was then switched and the focuser was heated rapidly and a separate N_2 tank was used to backflush the toluene desorbed from the focuser to the GC column (Figure 3.8C). The mass of toluene injected was determined from the FID peak area by comparison with the calibration curve. Replacement of the focuser with the sample loop and collection of an additional sample allowed the chamber concentration to be checked post-exposure for residual toluene.

The focuser was a stainless steel tube (0.318 cm i.d.) packed with 5 mg of C-X (sieved to ~200 μm in diameter) held in place with wire mesh and silanized glass wool. It was pre-conditioned initially at 300 ˚C for 12 h under N_2. The focuser was wrapped with an insulated Cu heater wire and thermally desorbed at 300 ˚C for 10 min, which served to transfer the toluene to the GC and re-condition the adsorbent for subsequent samples. The capacity of the focuser was verified in a separate series of tests showing that the mass of toluene captured and transferred to the GC matched that expected to be within 1.5%.

The PCB-mounted μPPI was placed on the pedestal in the center of the exposure chamber, electrical and fluidic interconnections were established, and the chamber was sealed and then purged with N_2. The system was programmed for repeated heating and cooling tests using LabView. The μPPI was preconditioned at 300 ˚C for 4 h. A constant concentration of 1 ppm of toluene vapor was passed through the chamber continuously and the μPPI was allowed to collect samples for discrete periods of 5, 10, 15, 20, 30, 40, 50, or 60 min. This concentration would be considered relatively low for industrial working environments and relatively high for typical office or residential environments [91, 92]. We found it a convenient concentration level to use for this study because stable test atmospheres could be generated easily and the sampling times required to accumulate quantities of toluene above the detection limit of the FID were not excessively long. Tests were run in triplicate for each time period. Following each exposure, the chamber was purged for 3 min with 0.11 L/min of N_2 to remove any residual vapor. Then, the flow of N_2 through the chamber was stopped and the μPPI was rapidly self-heated to ~300 ˚C for 3 min to desorb the captured toluene. Prior to heating, a Tedlar bag filled with N_2 was connected to the chamber in order to provide make-up gas. The mini-pump was activated to draw the desorbed toluene through the device outlet port and the focuser for 6 min at a flow rate ranging from 10 to 50 mL/min (note: 50 mL/min was the default flow rate used for all experiments except those designed to examine the effect of varying flow rate on capture/injection efficiency). The 6-port valve was then actuated and the focuser was heated under a flow of N_2 at 1.8 mL/min to inject the captured vapor sample into the capillary column for elution and detection by the FID.

3.6 Results and Discussion

This chapter presents thermal response, sampling rate, and injection efficiency of the μPPI for the development of the field deployable GC system. For this goal, we measure the temperature profile of the μPPI cavity membrane experimentally. Preliminary results demonstrating the sampling rate of toluene using the TGA and the exposure chamber are presented. Finally, we test the injection efficiency of the μPPI and compare it with the analytical prediction.

3.6.1 Thermal Response

To assess the thermal characteristics of the μPPI, the adsorbent loaded device was cycled between the ambient temperature and the target desorption temperature (300 ˚C) by repeatedly applying a constant bias of 12.5 V to the heater for 10 s and allowing it to cool for 190 s with air flowing through the device. For the 140 Ω baseline resistance of the meander line heater, this corresponds to an average of 1.1 W of dissipated power. Fig. 3.9 shows a series of temperature response profiles indicating that the floor of the cavity reaches 250 ˚C within 0.23 s and 300 ˚C within 3 s. The thermal cycling was continued for 100 hours, corresponding to ~2000 cycles, during which the time to reach the maximum temperature varied by < 10 % and the minimum and maximum temperature varied by < 3 %. The power dissipation, thermal response, repeatability, and robustness exhibited by the device are all quite satisfactory.

3.6.2 Gravimetric Estimation of Sampling Rate

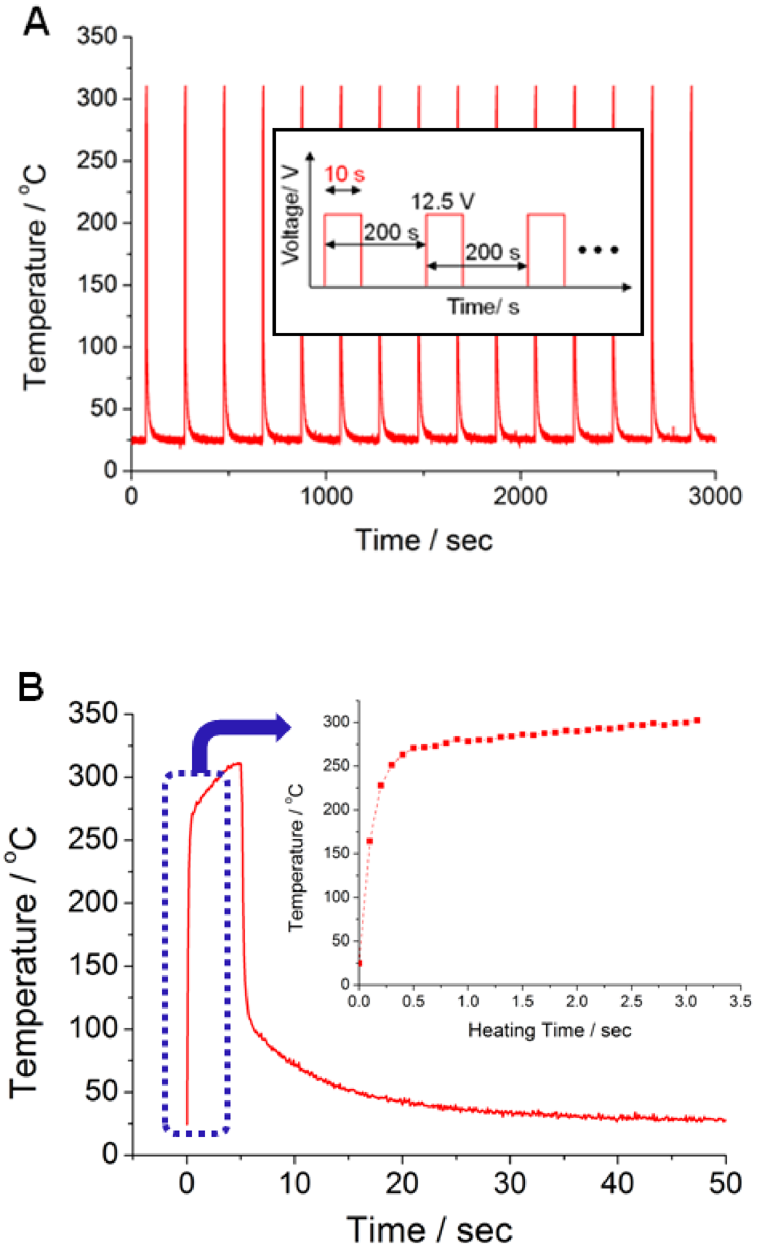

Figure 3.9. Thermal response of the µPPI at power input of~1W. (A) Temperature profile of the µPPI cavity membrane during thermal cycling. Each cycle with a 200 s period consists of a heating cycle of 10 s and a cooling cycle of 190 s. (B) Magnified temperature profile of the µPPI cavity membrane during the heating cycle. The temperature reaches 250 ˚C in 0.23 sec and 300 ˚C in 3 sec.

Preliminary tests of the sampling rate performed with the TGA apparatus entailed continuous exposure to ~1.2 ppm of toluene for 60 min while monitoring the mass uptake. Equation (3.1) was used to estimate *S*. Following a few minutes of induction, the mass uptake increased roughly linearly with time up to 24 min and then tapered off

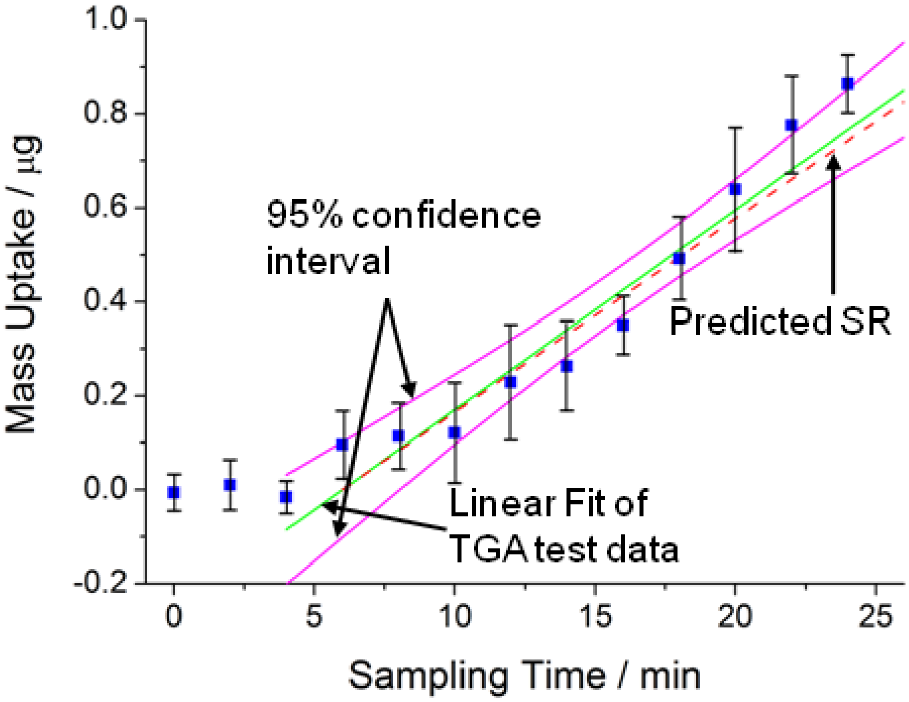

Figure 3.10. Mass uptake rates of µPPI measured by TGA for the diffusion length of 265 µm. The experimental data is ranging between the 95% confidence regions. Thus, the test sampling rate from the data meets the accuracy criterion of ±25% at the 95% confidence level.

significantly. Unfortunately, fluctuations in the TGA output signal, which are attributable to flow-induced vibrations of the wire-suspended device, were significant (Fig. 3.10). Applying a 120-pt running average to smooth the data [93], followed by linear regression (r^2 = 0.967) yielded a value of *S* = 9.8 ±0.49 mL/min from the slope of the line. This is 5% higher than the aforementioned theoretical value of 9.3 mL/min. The total mass uptake for the linear portion of the curve was 0.86 µg, which is 45% of the total capacity of 2.1 µg. Given the mass resolution limitat ions of the TGA, the precision with which the slope and linear range can be estimated is limited. However, these results provide confirmation of expectations for a linear mass uptake period followed by a reduction in that rate as the fraction of occupied adsorption sites becomes large, in this case ~45% of the total predicted on the basis of the measured W_e value.

3.6.3 Chamber Tests of Sampling Rate and Desorption/Injection Efficiency

Subsequent tests, performed in the exposure chamber, afforded more accurate and precise estimates of S. Fig. 3.11 shows a plot of injected mass *versus* sampling time from 5 to 60 min. The relative standard deviation was ≤ 5 % in all cases. Analysis of the residual toluene in the chamber headspace following each desorption led to values ranging from 3-7 % of the amount initially injected, which means that the capture/transfer efficiency ranged from 93-97 %. There was no apparent trend in transfer efficiency with sampled mass. These results indicate that the sampling/desorption performance of the μPPI is reproducible not only within a given sampling time but also over the entire series of experiments.

The mass uptake rate is constant up to ~30 min, after which it declines, in rough agreement with the results of the TGA experiments. A value of S = 9.1 mL/min was obtained from the slope of the linear region ($r^2 > 0.999$) of the curve after correcting for the residual mass of toluene not transferred during the initial desorption. This is only 2 % lower than the theoretical prediction, and corresponds to a mass uptake rate of 34 ng/min at this concentration. The linear dynamic range of the mass uptake (*i.e.*, up to 30 min) was 1.01 μg, which corresponds to 48 % of the total mass expected on the basis of W_e

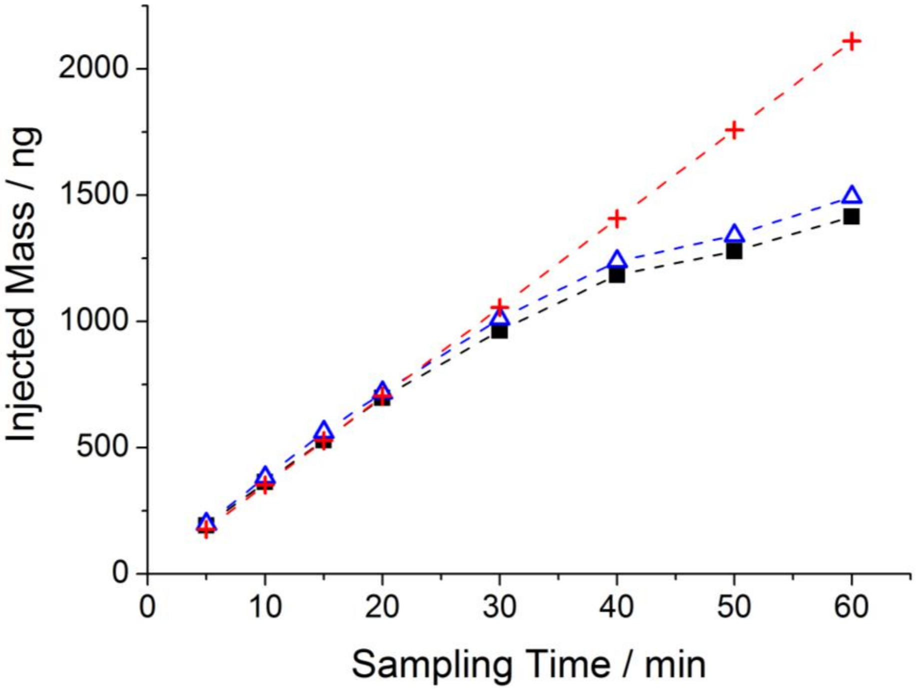

Figure 3.11. Plots of the mass of toluene captured and thermally desorbed (injected) by the µPPI as a function of sampling time for a 1 ppm challenge concentration and a desorption (suction) flow rate of 50 mL/min. The red line (+ symbol) reflects the expected mass uptake assuming the designed sampling rate of 9.3 mL/min. The black curve (filled squares) shows the experimental data obtained from the initial desorption of each sample. The blue curve (open triangles) shows the experimental data after addition of the residual mass of toluene that was not captured during the initial desorption. The reduction in the rate of mass uptake beyond 30 minutes reflects the decline in the sampling rate that occurs as the number of available surface sites on the adsorbent decreases.

and indicates that above this level of adsorbent loading the assumption of efficient trapping by the adsorbent no longer holds. However, thermal desorption of the captured sample regenerates the device for subsequent use with no apparent degradation in performance. Beyond 30 min, the device continues to sample, but at a lower rate, which is expected to continue to decrease as the adsorption sites on the C-X become completely filled. At *t* = 60 min, the mass uptake was 1.5 µg, which is 71 % of the total (2.1 µg) expected on the basis of the measured equilibrium adsorption capacity, W_e, assuming the designed sampling rate of 9.3 mL/min.

The capture/injection efficiency during thermal desorption was then examined as a function of the suction flow rate. For each of these tests, the device was exposed to 1 ppm of toluene for 15 min, leading to an expected mass uptake of 525 ng. The device was then heated while drawing flow from the downstream mini-pump at different flow rates. Results, plotted in Fig. 3.12, show that the capture efficiency decreases at a modest rate on going from 53 to 20 mL/min and at an apparently higher rate below 20 mL/min. The high efficiency observed at 52 mL/min (*i.e.*, 93 %) is consistent with the results reported above and with predictions from CFD analysis.

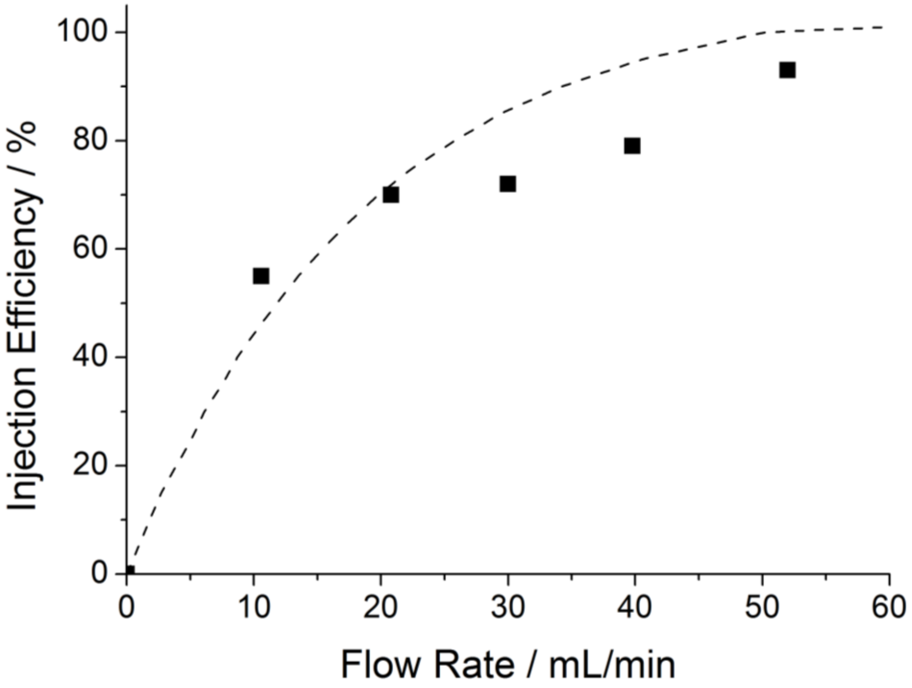

Figure 3.12. Modeled (dashed line) and experimental (filled squares) values of capture/transfer (injection) efficiency versus suction flow rate for the μPPI.

To further explore this, a two dimensional analytical model was developed for the capture/injection efficiency of the μPPI. Fig. 3.13 shows the top view of characteristic flow regions within the μPPI and the simplified cross sectional view of the characteristic flow region of the μPPI cavity. Fig. 3.13B is used for a model to predict the capture/transfer efficiency as a function of the suction flow rate as shown in Fig. 3.12. The model allows us to examine the "no vapor loss condition" for the empty cavity condition (L_0=0, maximum head space condition) and the adsorbent packed condition (L_0=161 μm, minimum head space condition). These two cases are studied to verify that the CFD model in Fig. 3.6 considered the most conservative (i.e., the worst scenario) condition.

The CFD analysis indicates that the device cavity can be divided into 3 characteristic flow regions between the central node of the flow pattern and the 3 outlet positions (Fig. 3.13A) regardless of the suction flow rate. These regions have similar velocity distributions and flow streamline patterns. The top of each characteristic region represents the position of the bottom of the diffusion channel layer of the μPPI. A spatially uniform vapor flux q'' driven by convention vertically enters the characteristic region from its top. The shape of each characteristic region is approximated to be a rectangular box defined by the cavity height (the adsorbent height L_0 + the head space height L_2), the effective flow length L_x, and the characteristic width L_y. The values of L_x and L_y are determined by taking the average distance between the two facing sides of the frame delineating the characteristic region in the x-direction (the direction pointing towards the outlet from the central note) and y-direction (the direction normal to the x-z plane), respectively. For Region 1, L_x is 1.2 mm and L_y is 2.0 mm, whereas L_x and L_y are

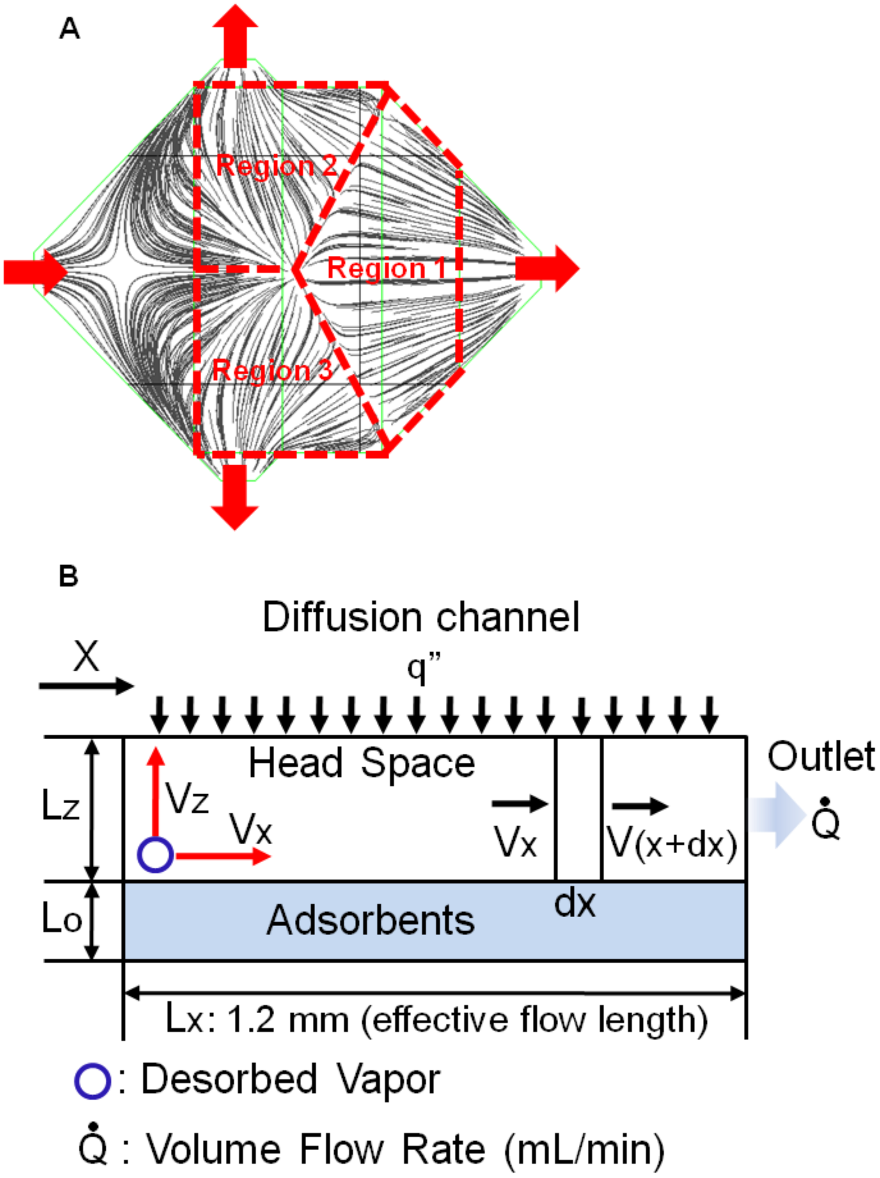

Figure 3.13. (A) Top view of characteristic flow regions within the μPPI cavity. (B) Simplified cross-sectional view of the characteristic flow region of the μPPI cavity.

both 1.2 mm for Region 2 and 3. L_z is 89 μm and 250 μm for the adsorbent packed condition and the empty cavity condition, respectively.

The model derives a mathematical formulation which accounts for the fraction of the amount of the vapors arriving at the bottom of the diffusion channel layer in the *z*-direction before reaching the outlet to the total vapors leaving the C-X surfaces. The "no loss condition" refers to the condition where the desorbed vapors leaving the adsorbent surface should horizontally reach the outlet without vertically arriving at the bottom surface of the diffusion channel layer. The vapor velocity distribution is assumed to be uniform across the *x*-*y* plane. The *x*-direction velocity V_x is estimated from the volume flow rate at each outlet. The vapor velocity to the z-direction V_z is equivalent to the vapor desorption linear velocity. The no loss condition requires the following relationship for the motion of the vapor molecule leaving the adsorbent surface at the left end corner at *x* =0:

$$t_x \leq t_z \tag{3. 7}$$

where t_x is the time required for the particle to pass through the cavity in the *x*-direction, t_z is the time required for the particle to reach the bottom of the diffusion channel layer in the *z*-direction. Applying mass balance for the differential control volume between *x* and *x*+*dx*, the governing equation for V_x is derived as

$$\frac{dV_x}{dx} - \frac{q''}{L_z} = 0 \tag{3. 8}$$

Solving the equation with the boundary conditions: $V_x(x = L_x) = q''(L_x + L_z)/L_z$, and $V_0 = q''$, which are derived from conservation of mass for the entire cavity and from Bernoulli equation, yields

$$V_x(x) = q'' \frac{(x + L_z)}{L_z} \tag{3. 9}$$

Now, the horizontal travel time t_x and the vertical travel time t_z are given as follows:

$$t_x = \int_0^{L_x} \frac{1}{V_x} dx \tag{3. 10}$$

$$t_z = \frac{L_z}{V_z} \tag{3. 11}$$

Then, the critical position x_c where $t_x = t_z$ for the vapor molecule leaving the adsorbent surface can be found using equation (3. 10) and equation (3. 11), yields

$$t_z = \int_{x_c}^{L_x} \frac{1}{V_x} dx \tag{3. 12}$$

From equation (3. 12), the critical position x_c can be determined with the suction flow rate. The vapor molecules desorbed at $0 < x < x_c$ escape from the diffusion channel while those desorbed at $x > x_c$ are injected. Thus, the capture/transfer efficiency *eff* is given by

$$eff = \frac{L_x - x_c}{L_x} \times 100 \tag{3. 13}$$

Using equation (3. 13), the minimum volume flow rate of 58.73 mL/min and 50.12 mL/min satisfying "no loss condition" are achieved for the empty cavity and the packed cases, respectively. Therefore, we can conclude the empty cavity condition (maximum head space case) represents the most conservative condition leading to the maximum vapor loss. The flow rate value of 58.73 mL/min is consistent with the one used in the aforementioned CFD analysis.

In other words, this 2D model derives a mathematical formulation for the ratio of the sampled mass to the mass capture (and transferred to the focuser for GC analysis) during thermal desorption as a function of the suction flow rate. As shown by the dashed line in Fig. 3.12, the agreement of the model with the experimental results is reasonably good, particularly at the extremes of the range tested; the experimental value of 93 % efficiency at the highest flow rate of 52 mL/min is only 7 % lower than predicted by the model. Notably, a flow rate > 10 mL/min is required to capture > 50 % of the desorbed vapor sample, hence the need for a focuser (or split-flow adaptor) to interface with a GC (micro)column.

3.7 Summary

The design, fabrication, and preliminary testing of a micromachined-Si passive vapor preconcentrator-injector (μPPI) have been described. Intended for incorporation in a gas chromatographic microsystem (μGC) for analyzing organic vapor mixtures, the μPPI captures vapors from the air at a known rate by means of passive diffusion (i.e, without pumping) and then desorbs the vapor sample thermally by means of an integrated heater and transfers it downstream (with pumping). The μPPI chip comprises a 1.8-μL deep-reactive-ion-etched (DRIE) Si cavity with a resistively heated membrane floor and a DRIE-Si cap containing >1500 parallel diffusion channels, each 54×54×200 μm. The cavity is packed with 750 μg of a commercial graphitized carbon adsorbent. Fluidic and heat-transfer modeling was used to guide the design process to ensure power-efficient sample transfer during thermal desorption. Experiments performed with toluene at concentrations of ~ 1 ppm gave a constant sampling rate of 9.1 mL/min for up to 30 min, which is within 2% of theoretical predictions and corresponds to a linear dynamic mass uptake range of ~ 1 μg. The cavity membrane could be heated to 250 ˚C in 0.23 s with 1 W of applied power and, with 50 mL/min of suction flow provided by a downstream pump, provided > 95% desorption/transfer efficiency of adsorbed toluene samples over an 8-fold range of captured mass.

CHAPTER IV

IMPACT OF MICROSCALE ON-CHIP HEATING ON VAPOR RELEASE AND INJECTION

4.1 Introduction

Volatile organic compounds (VOCs), emanating from solids or liquids at finite vapor pressure, may cause adverse health risks from breathing indoor/ambient air. A gas chromatographic system (GC) is widely used to measure and monitor VOCs. It is often challenging to obtain on-site data in indoor or ambient air due to high costs, high power requirements, and large sizes. Therefore, *in-situ* analysis and on-site monitoring of VOCs in moderately complex mixtures require the use of a microscale gas chromatographic (μGC) system that can serve as a highly portable micro-analytical tool. The valuable applications of a μGC system include point-of-care medical diagnostics, homeland security, worker exposure assessment, and so on. A μGC system generally comprises the following three essential components, all of which are fluidically interconnected and microfabricated: (1) a preconcentrator, (2) a separation column, and (3) a detector [8, 10-14]. In particular, microfabricated preconcentrator devices (μ-preconcentrators) play a critical role to enhance the detection sensitivity and separation resolution of μGC systems; they trap and concentrate VOCs initially at low concentrations with integrated adsorbents and inject high-intensity sharp plugs of the trapped VOCs via rapid thermal desorption to a downstream GC column.

As part of our on-going effort to establish a real-time field-deployable gas micro-analytical system, we introduced an on-chip device named the "microfabricated passive vapor preconcentrator/injector (μPPI)" in chapter 3 [94]. This device is the *first* microfabricated VOC preconcentrator that enables both zero-power diffusion-based passive sampling and preconcentration of VOCs and sample release/injection by controlling the temperature of its integrated on-chip micro-heater. The μPPI achieves a high sampling rate of 9.1 mL/min by diffusion and delivers the sampled vapor to a downstream GC component by thermal desorption at a low power of ~ 1 W. The sample loss is <5 % when a carrier gas flow rate was set at 50 mL/min. The device is used for on-chip gas chromatographic (GC) analyses in a matter of minutes with high separation and detection performance. The function of zero-power sample trapping and focusing of this device is to significantly reduce the total energy use required for GC analyses. The μPPI holds great promise to realize a battery-operated standalone field-deployable μGC system.

Over the last decade, significant research efforts have been made to develop μ-preconcentrators for field-deployable μGC systems [18-20, 28, 30, 31, 74-76]. However, little study has been performed to *quantitatively* assess their release/injection performance, which could significantly influence the separation resolution and sensitivity of GC analyses. Existing knowledge is only limited to elution peak tailing phenomena due to the undesirable condition of a separation column where non-equilibrium interactions occur between analyte molecules and its stationary phase [95-102]. A separation column is normally optimized to suppress these interactions before its use in a μGC system. Such an optimized column has been shown to successfully minimize elution peak-band tailings in a standalone setting [45, 99]. Yet, significant peak-band tailings [8, 10, 13, 14] are still consistently observed after the optimized column is integrated with other μGC components [39, 45]. We hypothesize that these peak tailings are attributed to a μ-preconcentrator yielding non-ideal vapor injection peak band profiles. The peak tailings induced by the unoptimized μ-preconcentrator would cause overlapping between consecutive vapor effluents, thus limiting the system's ability to resolve even moderately complex VOC mixtures. In addition, conventional μ-preconcentrators are heated for an excessive heating period to ensure the completion of vapor delivery to a GC column without fully examining fundamental phenomena governing the device performance and their impact on GC analyses [18-20, 28, 30, 31, 74-76]. The excess heating seriously compromises the original purpose of reducing the total energy consumptions of μGC systems with these devices.

In this chapter 4, we investigate the influence of microscale heating conditions on the vapor release and injection performance of the μPPI to fill the knowledge gap existing for the device. We employ the modified desorption kinetic model [76, 103-105], together with the transient heat transfer theory to predict the dynamic process associated with the thermal release of vapor trapped within the μPPI. Using the model prediction, we quantify the elution peak tailing effect induced by the μPPI prior to column separation and carefully study the. peak height and full width at half maximum (FWHM) of elution peak band signals. All of these signal characteristics are experimentally observed using an on-column optical fiber-based Fabry-Pérot (FP) gas sensor directly embedded in an interconnect tubing connected to the outlet of the μPPI. To our best knowledge, this paper presents the *first* study that quantitatively elucidates the correlation between the thermal desorption/vapor injection behavior of a μ-preconcentrator-type device and the resulting peak band signal characteristics. The presented results clearly support our original working hypothesis that the μ-preconcentrator performance is critically important for GC analyses as well as the column condition. This study provides us with an approach to optimizing chromatographic peak-band signal conditions and to minimizing the energy consumption of a μGC system incorporating the μPPI.

4.2 Materials and Methods

This chapter discusses the fabrication and experimental methods for the designed micro-device. The device fabrication was performed at the Lurie Nanofabrication Facility (LNF) at the University of Michigan. Experimental methods include measurement of vapor desorption and injection, transient thermal response, and vapor peak signals.

4.2.1 Device Design and Fabrication

The μPPI is designed on the basis of the classical Fickian diffusion theory, heat transfer, and fluid dynamics. The device consists of two layer structures (Fig. 4.1A); the top layer incorporates vertical square diffusion channel grids for passive VOC sampling from air; and the bottom layer contains a membrane cavity structure with tapered entrance/exit on its two sides, pillar structures to retain the graphitized carbon beads inside, and a meander-line Ti/Pt micro-heater and a resistance temperature detector (RTD) on its backside. As the first step of the device operation, the graphitized carbon (Carbopack X) beads on the cavity floor adsorb VOCs in the presence of a concentration gradient across the diffusion channel grids with no power requirements. Subsequently, the device is heated to thermally release the captured VOCs and to inject them to a downstream GC system with a carrier gas flow driven by a miniature pump. In our previous study [94], the μPPI was fabricated using silicon micromachining and Au eutectic water bonding. The device achieved a sampling rate of ~9.1 mL/min by means of the passive diffusion process at a carrier gas flow rate of 50 mL/min.

4.2.2 Experimental Setup

4.2.2.1 Vapor Desorption Characterization Setup

To study the vapor desorption effect within the μPPI, we first use a custom-made exposure chamber setup introduced in chapter 3 [94] and characterize the device using

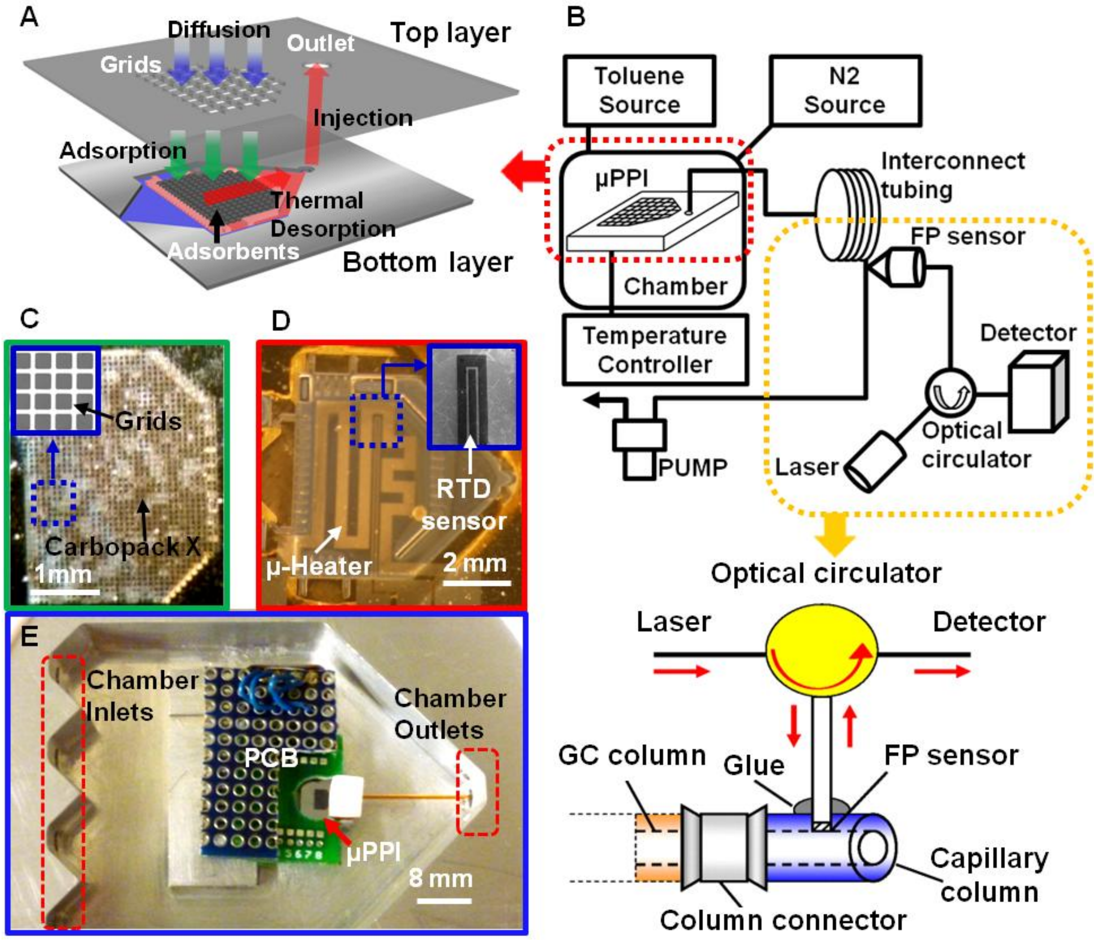

Figure 4.1 (A) Conceptual diagram of the μPPI showing the diffusional sampling and thermal desorption processes. (B) Schematic of the test setup incorporating a Fabry-Pérot (FP) optical gas sensor that was used to characterize the μPPI performance for real-time desorption and injection of toluene. (C) Optical image showing the top layer of the μPPI with diffusion channel grids and see-through image of Carbopack X beads packed underneath. (D) Optical image of the micro-heater and RTD sensor on the backside of the bottom layer of the μPPI. (E) Optical image of the μPPI mounted in the exposure chamber with its PCB packaging.

toluene as a model VOC. The experimental setup used for the characterization of vapor desorption within the μPPI incorporates the same custom-made exposure chamber setup as shown in Fig. 4.1E and a commercial CG system (Model 6890a, Agilent, Wilmington, DE) fluidically connected to this chamber via a focuser and a separation column [94]. After mounted on a wire-bonded printed circuit board (PCB), the μPPI is placed on the pedestal in the center of the exposure chamber. A flow splitter is placed at the chamber inlets to evenly distribute the incoming carrier gas (N_2) flow over the μPPI placed inside. The exhaust flow is directed to the chamber outlet connected to the downstream GC system. After electrical and fluidic interconnections are established, the exposure chamber is sealed. The system is programmed to control the device temperature using the LabView (National Instruments, Austin, TX) program. The sealed chamber is initially purged with N_2 and then filled with toluene in N_2, which is followed by the passive sampling with the μPPI. After finishing loading the toluene sample to the μPPI, the chamber is re-purged to remove the residual toluene vapor. A mini-pump (KNF Neuberger, Trenton, NJ) is operated to draw the vapor in N_2 through the device outlet to a focuser at a flow rate of 50 mL/min. The flow rate of 50 mL/min is necessary to minimize the vapor loss during the vapor desorption process by the μPPI. But it exceeds the maximum flow rate usually permitted in conventional GC separations (< 5 mL/min). As a result, we first re-capture the toluene injected from the μPPI at the focuser and then deliver it to the flame ionized detector (FID) at a lower flow rate compatible with the GC system. We determine the total toluene mass released from the μPPI from the integrated signal of the FID and its calibration data. The exposure chamber is cleaned with N_2 upon the completion of each desorption characterization cycle for subsequent repeated measurements.

4.2.2.2 Injection Peak Signal Characterization Setup

We further modify this setup such that it incorporates an FP gas sensor built in a stationary phase-free inert tubing (50 cm (L) and 0.23 cm (i.d.)) and characterize the injection peak signals generated by the μPPI (Fig. 4.1B). The interconnect tubing with the relatively large inner diameter is necessary to retain the original injection profile with minimum band dispersion at the detection point. A relatively high N_2 carrier gas flow rate of 10 mL/min is used to minimize the height equivalent to a theoretical plate in the tubing as shown in Fig. 4.2. The FP gas sensor is fabricated by sequentially depositing a metal

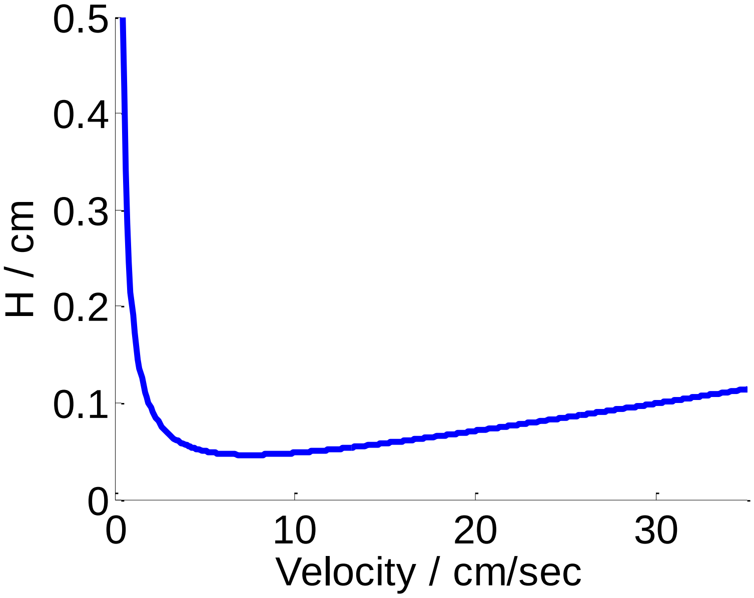

Figure 4.2 Height equivalent to a theoretical plate (H) versus average carrier gas (N_2) velocity for the stationary phase-free, inert, interconnect tubing used in the device characterization. Assuming toluene as the test vapor, the theoretical plot for the circular cross-section tubing is obtained from the simplified Golay and Spangler equation. The minimum plate height of ~ 0.05 cm occurs at the carrier gas velocity of 4 – 10 $cm \cdot s^{-1}$, which corresponds to the sample flow rate of 10 – 25 $mL \cdot min^{-1}$. Considering that the conventional gas chromatographic (GC) separations need a lower flow rate (< ~ 5$mL \cdot min^{-1}$), our experiments employ the lower bound for the flow rate value of 10 $mL \cdot min^{-1}$ in the above optimal range.

layer and a gas-sensitive polymer layer on the end-face of an optical fiber to form an FP cavity [55, 106, 107]. Light coupled in the optical fiber is partially reflected at the metal layer and the interface between the polymer and air, generating an interference spectrum. When the FP sensor is exposed to gas analyte, the polymer interacts with gas analyte, resulting in the shift of the interference spectrum. By monitoring the shift, we are able to obtain the kinetic information of gas analytes. Here, the FP sensor enables real-time signal detection at this flow rate, which is not typically allowed by the conventional GC/flame ionization detector (FID) system. Toluene vapor at 1 ppm is passed through the chamber for 90 min and loaded to the device, then followed by purging the chamber for 30 s with N_2 at 1 L/min to remove the residue of the toluene vapor. The top layer of the device is then temporally covered with a glass substrate to prevent vapor loss through the open diffusion channel grids during the thermal desorption process. After the purging process is completed, the micro-heater is turned on to heat the device up to ~ 300 ˚C at different heating rates for different periods of time. N_2 gas in a Tedlar bag is replenished to maintain the same pressure inside the chamber during the injection process. The toluene vapor was released from the μPPI and injected to the interconnect tubing. The toluene injection peak signal is eventually detected by the FP gas sensor.

4.2.3 Transient Thermal Model

We develop a heat transfer model to quantitatively predict the thermal response of the μPPI. Heat transfer equations are obtained from applying energy balance to each of the control volumes (CVs) assigned to several device structure sub-segments (Fig. 4.3A).

The equations account for changes in energy storage and heat transfer due to conduction and convection associated with the CVs. The contribution of radiation is estimated to be less than 1 % of the total heat transfer. Thus, our model neglects it. Because of the high thermal conductivity of the structural materials of the device and the adsorbent materials, we assume the isothermal condition for each CV. This allows us to apply the lumped thermal capacitance model to predict the temperature of each CV.

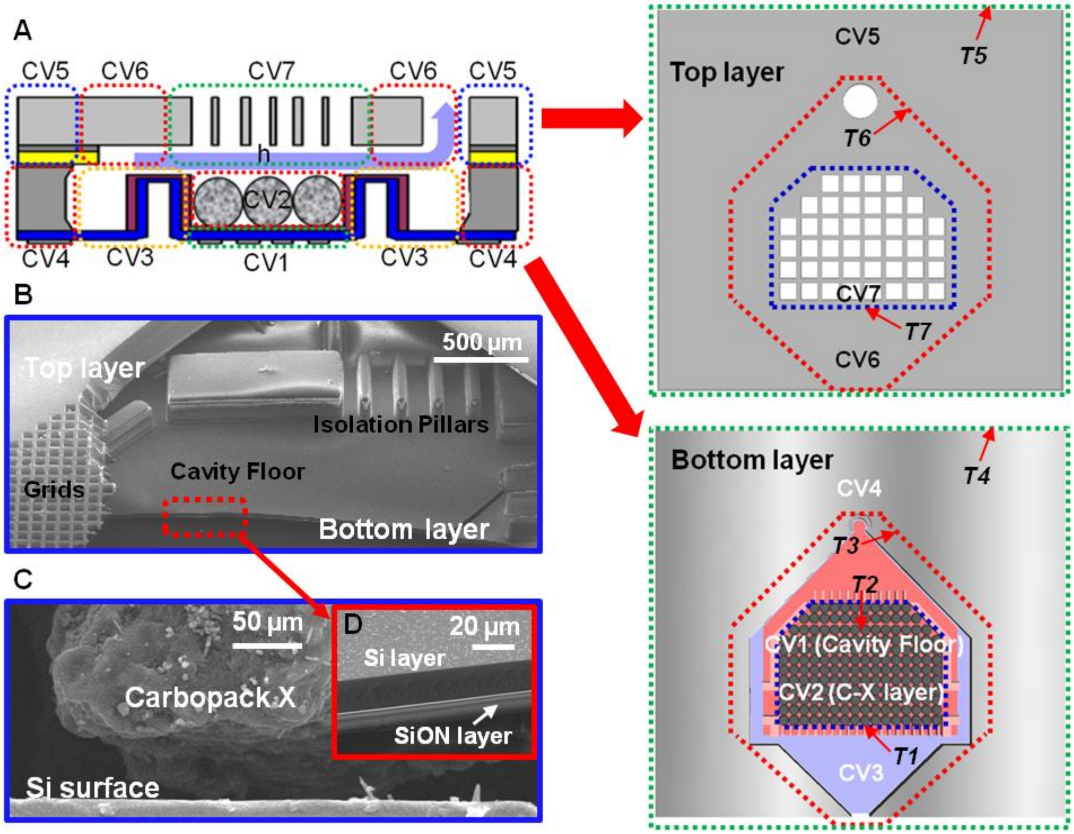

Figure 4.3 (A) Cross-sectional schematic of the μPPI and top views of its top and bottom layers with the control volumes used for the thermal analysis. (B) SEM image showing microfabricated structures of the open-cut device. (C) SEM image showing the Carbopack X-cavity floor interface. The contact area between the Carbopack X bead and the floor surface is measured from this image. (D) SEM image used to estimate the thicknesses of the boron doped silicon layer and the SiON layer.

Using the lumped thermal model, we have developed a series of governing equations for the temperatures at the seven segments of the μPPI: T_i (i = 1, 2, 3, 4, 5, 6, and 7) (Fig. 4.3A). Applying energy balance to the seven control volumes (CVs) surrounding the segments allowed us to derive these equations. The CVs include the membrane cavity floor (CV_1), the Carbopack X layer (CV_2), the isolation pillar structures (CV_3), the Si structure of the bottom layer bonded to the top layer (CV_4), the Si structure of the top layer bonded to the bottom layer (CV_5), the part of the Si top layer surrounding the diffusion channel grids (CV_6), and the array of the diffusion channel grids (CV_7). The resulting equations are given as:

$$TM_1 \cdot \dot{T}_1 = -\frac{T_1 - T_2}{R_{12}} + \dot{E}_{gen} - \frac{T_1 - T_3}{R_{13}} \tag{4. 1}$$

$$TM_2 \cdot \dot{T}_2 = \frac{T_1 - T_2}{R_{12}} - hA_2(T_2 - T_\infty) \tag{4. 2}$$

$$TM_3 \cdot \dot{T}_3 = \frac{T_1 - T_3}{R_{13}} - hA_3(T_3 - T_\infty) - \frac{T_3 - T_4}{R_{34}} \tag{4. 3}$$

$$TM_4 \cdot \dot{T}_4 = \frac{T_3 - T_4}{R_{34}} - hA_4(T_4 - T_\infty) - \frac{T_4 - T_5}{R_{45}} \tag{4. 4}$$

$$TM_5 \cdot \dot{T}_5 = \frac{T_4 - T_5}{R_{45}} - \frac{T_5 - T_6}{R_{56}} \tag{4. 5}$$

$$TM_6 \cdot \dot{T}_6 = \frac{T_5 - T_6}{R_{56}} - hA_6(T_6 - T_\infty) - \frac{T_6 - T_7}{R_{67}} \tag{4. 6}$$

$$TM_7 \cdot \dot{T}_7 = \frac{T_6 - T_7}{R_{67}} - hA_7(T_7 - T_\infty) \tag{4. 7}$$

where $TM_i \cdot \dot{T}_i$ represents the rate of energy storage for the thermal mass of the i^th^ control volume, which can be expressed as:

$$TM_i \cdot \dot{T}_i = (\rho C_p V)_i \frac{dT_i}{dt} \tag{4. 8}$$

where ρ (Si: 2330 kg·m^{-3}, SiON: 2400 kg·m^{-3}, Carbopack X: 410 kg·m^{-3}), C_p (Si: 712 J·kg^{-1}K^{-1}, SiON: 691 J·kg^{-1}K^{-1}), and V are the density, specific heat, and volume of one of the constituent materials (Si and SiON) or the adsorbent (Carbopack X) occupying the ith control volume. The value of the specific heat of graphite (709 J·kg^{-1}K^{-1}) is used for Carbopack X. Generally, R_{ij} represents the thermal resistance due to conduction between the ith and the jth CVs.

Now, R_{12} represents the contact resistance between the membrane floor and the Carbopack X bead, given by:

$$R_{12} = \frac{R''_{t,c}}{A_{12}} \tag{4. 9}$$

where $R''_{t,c}$ =10^{-4} m^2·K W^{-1} is the intrinsic thermal contact resistance at the interface and A_{12} = 4500 μm^2 is the total effective contact area between the Carbopack X layer and the cavity floor membrane. R_{45} is the thermal resistance due to conduction across the contact area between the bottom and top layers, given by:

$$R_{45} = \frac{L_5}{k_{Si} A_{45}} \tag{4. 10}$$

where k_{si} is the thermal conductivity of Si, L_5 = 200 μm is the thickness of the top layer and A_{45} is the bonding area between the top and bottom layers.

To estimate the values of $R_{ij} \neq R_{12}, R_{45}$, we model the device to have a composite structure consisting of cylindrical shells with an outer radius r_i. In this model, each shell represents one of the above control volumes CV_i (Fig. 4.4). We introduce the following boundary conditions in the radial direction:

$$T(r_i) = T_i \qquad \text{(i = 1, 3, 4, 5, 6, and 7)}$$

where T_i represents the temperature of CV_i defined in the original lumped thermal model. Applying these conditions, the analytical expression for R_{ij} is obtained as:

$$R_{ij} = \frac{\ln(r_j / r_i)}{2\pi k_j L_j} \tag{4. 11}$$

where k_j is the thermal conductivity of the constituent material in $\mathrm{CV_j}$, and L_j is the thickness of $\mathrm{CV_j}$, respectively. The values used for k_j and L_j are listed in Table 4.1.

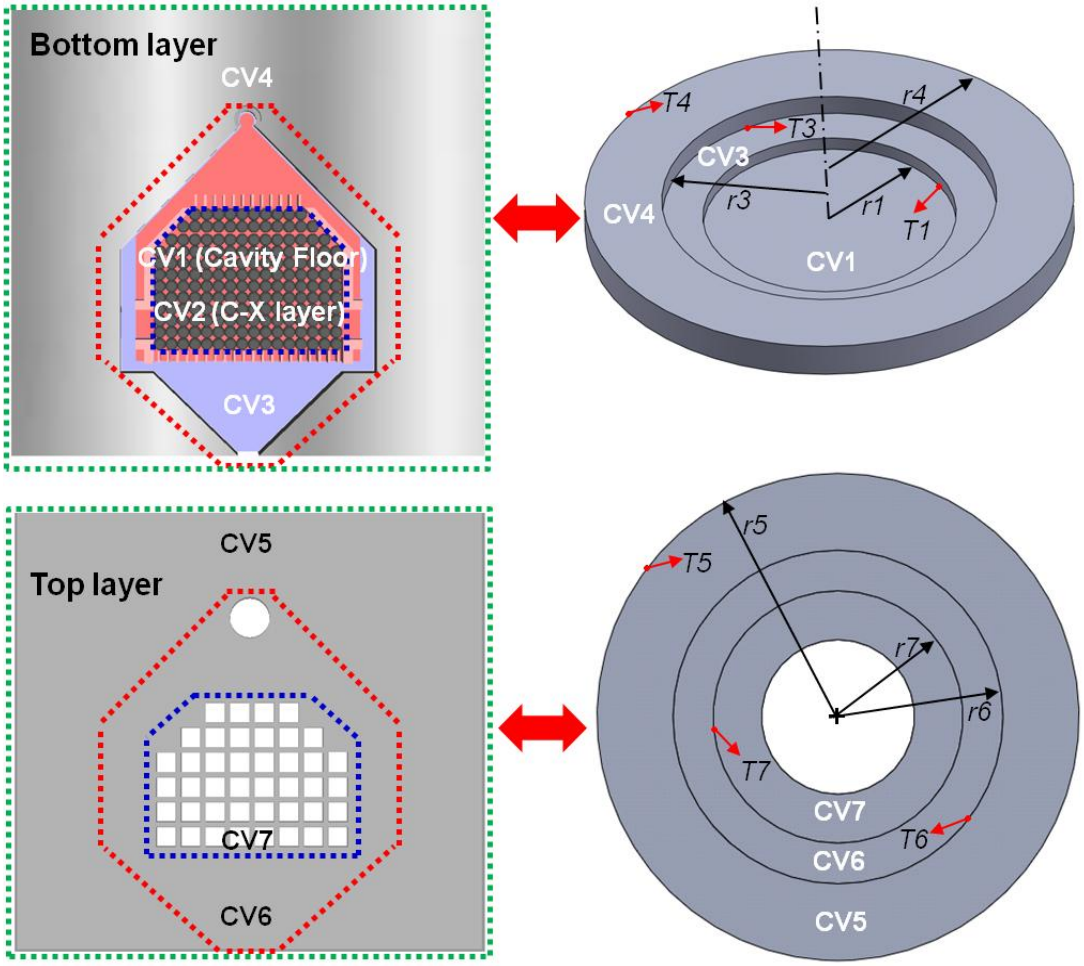

Figure 4.4 Top view of the bottom and top layers of the μPPI (Left) and cylindrical shell models approximating the structures of these layers for the analysis based on the lumped thermal method (Right). These figures show the control volumes (CVs) used for the transient heat transfer analysis. The right figure indicates the reference locations of the CV temperatures T_i (i = 1, 2, 3, 4, 5, 6, and 7) used for estimating the thermal resistance between adjacent CVs.

j	k_j ($\mathrm{W \cdot m^{-1} K^{-1}}$)	L_j (μm)
3	16	15
4	148	250
5	148	200
6	148	200
7	148	200

Table 4.1. List of thermal conductivity (k_j) and thickness (L_j) of each control volume ($\mathrm{CV_j}$).

Inside the device cavity, we assume forced convection at the surface of $\mathrm{CV_i}$ with an area of A_i exposed to the carrier gas flow, a heat transfer coefficient of h, and the ambient temperature T_∞ = 23°C. Assuming the physical properties of N_2 for the carrier gas, Reynolds number is Re = 512.2 for the flow rate of 50 $\mathrm{mL \cdot min^{-1}}$. To estimate the value of h, we first calculate the Nusselt number Nu = hD_h/k =6.22 using the convection correlations for a noncircular tube (rectangular cross section) in the laminar flow regime under the uniform surface heat flux boundary condition [108]. Estimating the hydraulic diameter of the flow channel inside the device cavity D_h = 1.05 mm allows us to obtain the value of h =153 $\mathrm{W \cdot m^{-2} K^{-1}}$ from the above value of Nu and k = 0.026 $\mathrm{W \cdot m^{-1} K^{-1}}$ (N_2 thermal conductivity).

The heat generation by the integrated micro-heater $\dot{E}_{gen}$ is given by

$$\dot{E}_{gen} = \frac{V_{in}^2}{R} \tag{4. 12}$$

where V_{in} and R are the applied input voltage and the electrical resistance, respectively. With all the values of these parameters estimated, the governing equations 4.- 4.7 are solved using the ode45 solver in MATLAB.

These simultaneous thermal equations are given in the following matrix form:

$$\begin{bmatrix} TM_1 \cdot \dot{T}_1 \\ TM_2 \cdot \dot{T}_2 \\ TM_3 \cdot \dot{T}_3 \\ TM_4 \cdot \dot{T}_4 \\ TM_5 \cdot \dot{T}_5 \\ TM_6 \cdot \dot{T}_6 \\ TM_7 \cdot \dot{T}_7 \end{bmatrix} = \begin{bmatrix} -\frac{1}{R_{12}}-\frac{1}{R_{13}} & \frac{1}{R_{12}} & 0 & 0 & 0 & 0 & 0 \\ \frac{1}{R_{12}} & -\frac{1}{R_{12}}-hA_2 & 0 & 0 & 0 & 0 & 0 \\ \frac{1}{R_{13}} & 0 & -\frac{1}{R_{13}}-\frac{1}{R_{34}}-hA_3 & \frac{1}{R_{34}} & 0 & 0 & 0 \\ 0 & 0 & \frac{1}{R_{34}} & -\frac{1}{R_{34}}-\frac{1}{R_{45}}-hA_4 & \frac{1}{R_{45}} & 0 & 0 \\ 0 & 0 & 0 & \frac{1}{R_{45}} & -\frac{1}{R_{45}}-\frac{1}{R_{56}} & \frac{1}{R_{56}} & 0 \\ 0 & 0 & 0 & 0 & \frac{1}{R_{56}} & -\frac{1}{R_{56}}-\frac{1}{R_{67}}-hA_6 & \frac{1}{R_{67}} \\ 0 & 0 & 0 & 0 & 0 & \frac{1}{R_{67}} & -\frac{1}{R_{67}}-hA_7 \end{bmatrix} \begin{bmatrix} T_1 \\ T_2 \\ T_3 \\ T_4 \\ T_5 \\ T_6 \\ T_7 \end{bmatrix} + \begin{bmatrix} \dot{E}_{gen} \\ hA_2T_\infty \\ hA_3T_\infty \\ hA_4T_\infty \\ 0 \\ hA_6T_\infty \\ hA_7T_\infty \end{bmatrix} \tag{4. 13}$$

where TM_i (i = 1, 2, 3, 4, 5, 6, 7) represents the thermal mass of the ith control volume CV$_i$, T_i (i = 1, 2, 3, 4, 5, 6, 7) is the temperature of CV$_i$, $\dot{T}_i$ (i = 1, 2, 3, 4, 5, 6, 7) is the rate of temperature change of CV$_i$, R_{ij} is the thermal resistance due to conduction between CV$_i$ and CV$_j$, h is the heat transfer coefficient due to convection by the carrier gas flow over the Carbopack X surface within the device cavity, A_i is the surface area of CV$_i$ exposed to the ambient, T_∞ is the room temperature (23 ˚C), and $\dot{E}_{gen}$ is the rate of heat generation at the micro-heater, respectively. We obtained the transient temperature profile of each CV by solving equation 4. 13.

4.2.4 Vapor Desorption Kinetics

The passive sampling of VOCs by the μPPI is based on the physisorption of the vapor molecules at the adsorbent surface. The mechanism of physisorption involves weak interactions between the gas molecule and the solid surface by means of the Van der Waals force. The physisorbed vapor molecules can be rapidly desorbed by increasing the surface temperature. Raising the internal (i.e., vibrational) energy of the molecules results in breaking the weak bonds. With its simplicity and reversibility, the physisorption process is widely employed in VOC preconcentration.

Upon heating, the adsorbed molecule receives the thermal energy equivalent to the heat of desorption ΔE_{des}, Even after this, there exists a certain period of time for the molecule to remain on the surface. This period is called the surface residence time τ, which is determined at a given temperature T and pressure as

$$\tau = \tau_0 \exp(-\Delta E_{des} / RT) \tag{4. 14}$$

where τ_0 is the period of vibration of the molecule adsorbed on the surface and is typically on the order of 10^{-13} s [109], and R = 8.3144621 $\mathrm{J \cdot mol^{-1} K^{-1}}$ is the ideal gas constant. It is experimentally shown that the value of ΔE_{des} ranges from 9.5 $\mathrm{KJ \cdot mole^{-1}}$ to 32 $\mathrm{KJ \cdot mole^{-1}}$ for toluene adsorbed on Carbopack X at the atmospheric pressure in the range of sample concentration used in our study [76]. From equation 4. 14, the residence time is calculated to be much shorter than 1 ms during the desorption process, which is negligible as compared to the heating time constant of the μPPI of ~ 100ms. This allows us to simply assume that the vapor desorption occurring in a system instantaneously reaches its equilibrium state at a given temperature.

We next obtain the adsorption capacity of the μPPI from adsorption isotherms - theoretical curves representing the equilibrium mass of vapor adsorbed per mass of adsorbent as a function of vapor concentration at a given temperature *T*. Among existing isotherm models, the Dubinin-Radushkevich-Kaganer (DRK) model is appropriate for the nonporous Carbopack X [76, 103-105]. The DRK model is given as:

$$N_a = N_{am-DRK} \exp\left[-\left(\left(\frac{RT}{\beta E_0} \right) \ln\left(\frac{p}{p_{sat}} \right) \right)^2 \right] \qquad (4.\ 15)$$

where N_a is the molar amount adsorbed (mmol/g) and N_{am-DRK} is the monolayer capacity (mmol/g) of the adsorbent, β is the affinity coefficient of the adsorbent, E_0 is the adsorption energy, p is the partial pressure of the vapor, p_{sat} is the saturation vapor pressure of the adsorbate at the test temperature. All parameters in the equation for toluene and Carbopack X are obtained experimentally and derived from published polarizability data [76, 110, 111]. The parameter values are given in Table 4.2.

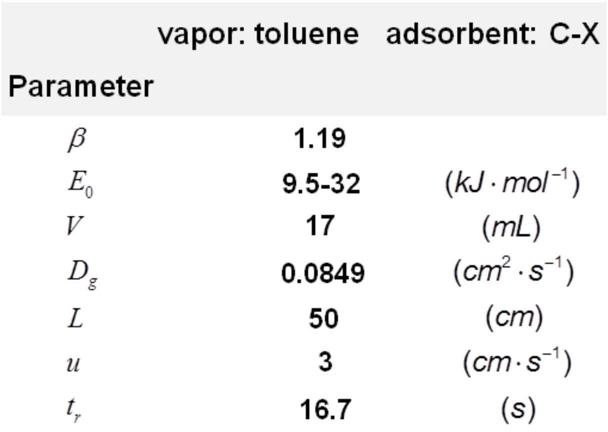

	vapor: toluene	adsorbent: C-X
Parameter		
β	**1.19**	
E_0	**9.5-32**	$(kJ \cdot mol^{-1})$
V	**17**	(mL)
D_g	**0.0849**	$(cm^2 \cdot s^{-1})$
L	**50**	(cm)
u	**3**	$(cm \cdot s^{-1})$
t_r	**16.7**	(s)

Table 4.2. Physical properties of toluene and Carbopack X, and experimental conditions. β: the affinity coefficient of the Dubinin Radushkevich Isotherm model (given as a ratio of the molar polarizability of the analyte to the molar polarizability of a reference, benzene), E_0: the adsorption energy, *V*: the volume of the gas, D_g: the vapor diffusion coefficient in the carrier gas, *L*: the length of the tubing, *u* : the average carrier gas velocity, and t_r: the retention time of the vapor to elute.

The partial pressure *p* (mmHg) and saturation vapor pressure p_{sat} (mmHg) of toluene can be obtained as functions of the adsorbent temperature *T* from the ideal gas law and Antoine equation as [112]:

$$p = \frac{nRT}{V} \tag{4. 16}$$

$$p_{sat} = 10^{\left(6.95464 - \frac{1344.8}{T + 219.482}\right)} \tag{4. 17}$$

where *n* is the number of moles of gas, *V* is the volume of gas used during desorption, respectively.

Now, the temperature profile of the adsorbent (i.e., Carbopack X) $T_2(t)$ as a function of time in equation 4. 13, the partial pressure in equation 4. 16, and the saturation vapor pressure of toluene at the temperature of T_2 in equation 4. 17 are substituted into equation 4. 15. The total amount of the vapor released from the adsorbent at a given time during the thermal desorption process is then obtained by subtracting the real-time adsorption capacity $N_a(T(t))$ from the initial capacity at room temperature $N_a(T(0))$. Thus, the real-time cumulative desorption profile $N_{des}(t)$ is expressed as:

$$N_{des}(t) = N_a(T(0)) - N_{am-DRK}\exp\left[-\left(\left(\frac{RT_2(t)}{\beta E_0}\right)\ln\left(\frac{nRT_2(t)}{V\cdot 10^{\left(6.95464-\frac{1344.8}{T_2(t)+219.482}\right)}}\right)\right)^2\right] \qquad (4.\ 18)$$

4.2.5 Vapor Peak Prediction

The theoretical chromatographic elution profile with respect to a delta-function injection input is given by the Gaussian distribution. The normalized elution profile $f(t)$ is given as:

$$f(t) = \frac{C_{\max}\exp\left(-\frac{(t-t_r)^2}{2\sigma^2}\right)}{\int_{-\infty}^{\infty} C_{\max}\exp\left(-\frac{(t-t_r)^2}{2\sigma^2}\right)} = \frac{1}{\sqrt{2\pi}\cdot\sigma}\exp\left(-\frac{(t-t_r)^2}{2\sigma^2}\right) \qquad (4.\ 19)$$

where $C_{\max}$ is the concentration at the peak maximum, t_r is the retention time to elute, σ is the standard deviation, respectively.

Once vapors are desorbed from the adsorbent, these are immediately injected to a downstream component by a continuous suction air stream. The dispersion of chromatographic bands of vapors still occurs via the circular interconnect tubing during the vapor injection process. Golay and Spangler developed kinetic models that address the elution profile of VOCs leading to the band broadening in the moving phase [113-115]. The simplified Golay and Spangler equation that describes band dispersion in the inert interconnect tubing with a circular cross-section is given as:

$$H = \frac{2D_g}{u} + \frac{r^2}{24D_g}u \tag{4. 20}$$

where H is the height equivalent to a theoretical plate, u is the average carrier gas velocity, D_g is the vapor diffusion coefficient in the carrier gas, r is the radius of the circular tubing, respectively. The first term on the right side of equation 4. 20 describes band dispersion from longitudinal diffusion. The second term describes band dispersion from nonequilibrium effects in the gas phase. Also, the band broadening, which is generally expressed as the elution curve bandwidth of 4σ, is intimately related to H, the retention time of the vapor t_r to elute, and the column length L. The retention time is also expressed as the column length L divided by the carrier gas velocity u. Assuming that the elution profile is the normal distribution and the injection pulse is the delta function, the standard deviation σ is expressed as:

$$\sigma = t_r \sqrt{\frac{H}{L}} \tag{4. 21}$$

Using equations 4. 19 − 4. 21, we can theoretically predict the chromatographic peak band signal resulting from a delta-function injection pulse. Substituting the values of the variables given in Table 4.2 into equation 4. 21 yields an expected standard deviation σ of 0.69 s. This number is applied in equation 4. 19 to theoretically obtain the elution profile of toluene with respect to a delta function injection profile.

The real-time injection profile of the target vapor $g(t)$ at the exit of the μPPI can be obtained by taking the time-derivative of equation 4. 18 (Fig. 4.5A). Then, we can calculate the theoretical peak band signal by taking the convolution of $g(t)$ and its impulse response corresponding to the normalized elution profile $f(t)$ (Fig. 4.5B), which is given by

$$(f * g)(t) = \int_{-\infty}^{\infty} f(\tau) g(t-\tau) d\tau \tag{4. 22}$$

The formulation in equation 4. 22 allows us to predict the band signal characteristics of the vapor peak detected by the FP optical gas sensor, including the peak height, the full width at half maximum (FWHM), and the tailings resulting from the real-time injection profile of the μPPI. All of these predicted band signal characteristics are directly compared to experimental results.

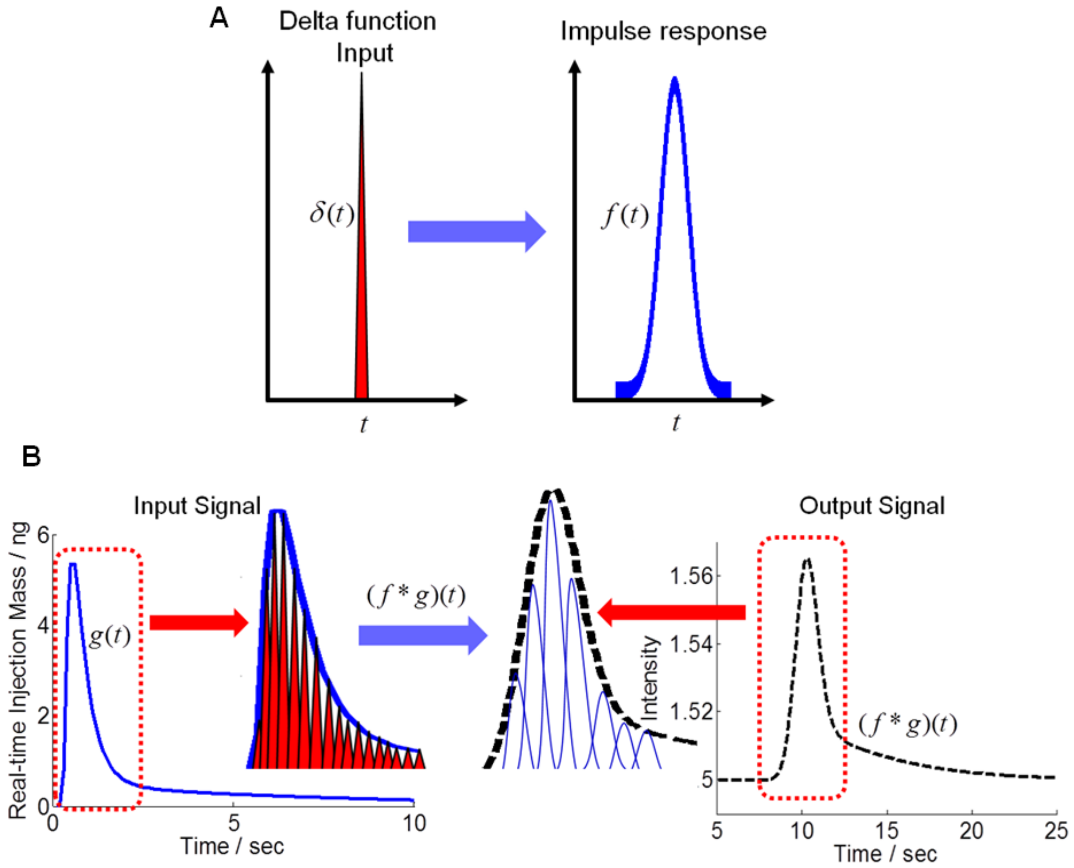

Figure 4.5 (A) Elution profile *f*(*t*) resulting from chromatographic dispersion in response to delta-function injection input $\delta(t)$. (B) "Real" injection peak band profile of toluene at the concentration of 1ppm generated by the μPPI *g*(*t*) (the left plot) and elution profile resulting from chromatographic dispersion in response to *g*(*t*), which is given by the convolution of *g*(*t*) and *f*(*t*) = (*f***g*)(*t*) (the right plot). The time derivative of the theoretical plot of the cumulative mass of toluene released via thermal desorption (Fig. 4.7) gives the theoretical plot of *g*(*t*). The result of this convolution (the right plot of (B)) represents the analytical prediction of the elution peak band signal measured by the FP optical sensor at the detection point.

4.3 Results and Discussion

This chapter demonstrates fast-thermal response and low-power operation of the μPPI, vapor desorption behavior, and effect of micro-heating on the vapor peak elution signals. For this goal, we show the experimental thermal responses of the μPPI for different heating durations and compare the results to the theoretical predictions. Experimental results demonstrating the effect of the thermal response of the μPPI on the vapor desorption phenomena are then presented. Finally, we theoretically and experimentally investigate the effect of on-chip micro-heating of the device on the elution peak signals.

4.3.1 Thermal Response Validation

The heating response of the μPPI was characterized experimentally and compared with the theoretical prediction provided by the aforementioned lumped thermal model. We estimated the parameters, such as thermal conductivity of the constituent materials, the membrane thickness, and the total effective contact area between the Carbopack X layer and the cavity floor from published data and scanning electron microscopy (SEM) images (see Fig. 4.3). The thermal conductivity and the thickness of the membrane affect the heat transfer rate by conduction across the membrane structure from the micro-heater. The thermal contact resistance R_c between the cavity membrane floor surface and the Carbopack X layer can be expressed as:

$$R_c = R''_{t,c} / A_c \tag{4. 23}$$

where $R''_{t,c}$ is the intrinsic thermal resistance of the interface (*i.e.*, the reciprocal of the thermal conductance per unit area) and A_c is the total effective contact area, which is estimated to be 4500 μm^2 from a SEM image (Fig. 4.3C). The intrinsic thermal contact resistance $R''_{t,c}$ generally ranges from 10^{-7} to 10^{-4} m^2·K W^{-1} for an interface between a carbon material and silicon [116, 117]. With the contact resistance at the Carbopack X-silicon interface unknown, we used the upper bound for the value of $R''_{t,c}$ = 10^{-4} m^2·K W^{-1} for the thermal equations for conservative model prediction resulting in a minimum heat transfer rate.

The μPPI was heated for durations of 2, 3, and 5 s at 1.1 W of average dissipated power and was allowed to cool for 50 s. The predicted heating responses of the cavity floor and the experimental results measured by the RTD sensor on the device membrane are both plotted (Fig. 4.6). The experimental data and the theoretical prediction are consistent with each other for all the heating durations. They indicate that the temperature of the membrane floor could reach 250 ˚C within 0.3 s under the above conditions. The device reached the maximum temperature of 289 ˚C, 300 ˚C, and 315 ˚C for the heating duration of 2 s, 3s, and 5s, respectively. The heat transfer model was verified by these tests. The predicted temperature profile of the cavity floor matched the measured temperature profile with an error as small as 2 %.

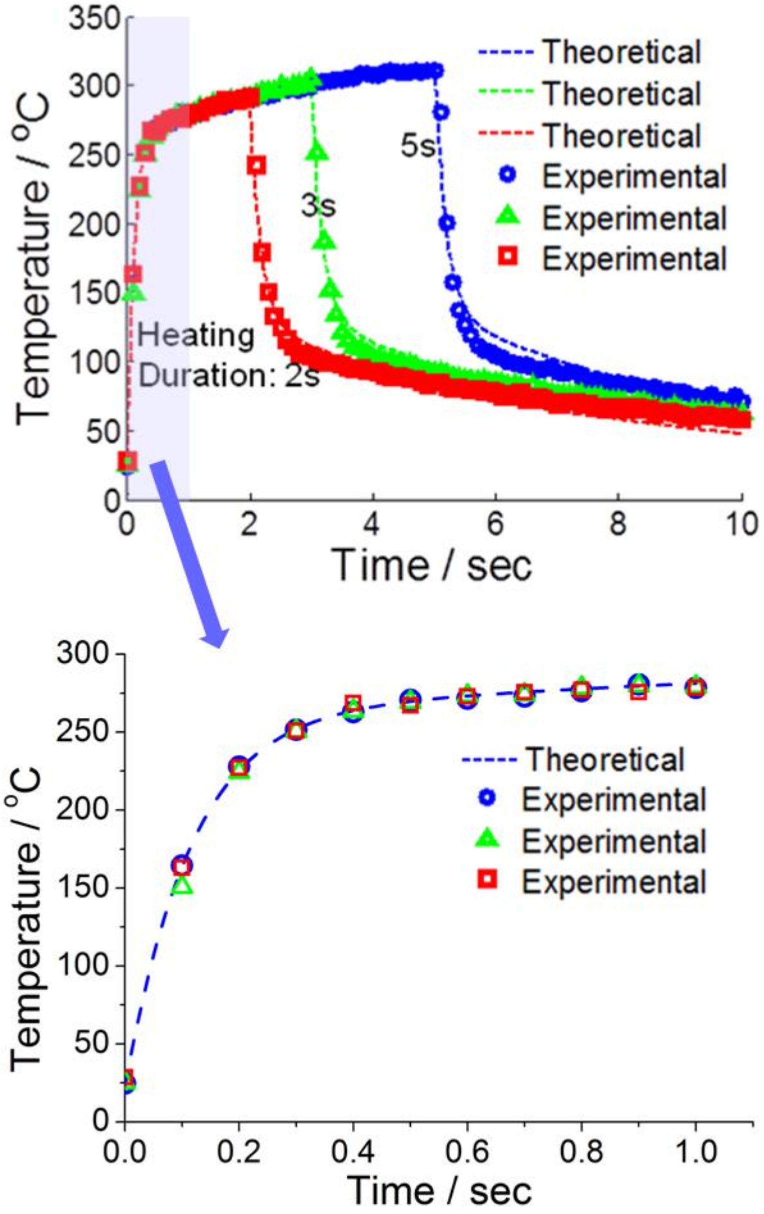

Figure 4.6 Theoretical (T_1 at CV_1) and experimental plots of the temporal temperature profile of the cavity floor membrane of the μPPI for three different heating durations (2 s, 3 s, and 5 s) at a heating power of 1.1 W. The red squares (□), green triangles (Δ), blue circles (o) represent experimental data obtained for different heating durations. The red-dotted, green-dotted, and blue-dotted lines are the theoretical profiles for heating periods of 2 s, 3 s, and 5 s, respectively. The lower plot showing the initial temperature rise during the 2 s (we should include 3 s and 5 s theoretical results to match the experimental results) heating duration indicates the small thermal time constant of ~ 100 ms for the μPPI, which allows the device to rapidly reach the high temperature of 250 ˚C within ~0.3 s.

4.3.2 Thermal Desorption Behavior

Our theoretical model coupled the thermal equations predicting the real-time adsorbent surface temperature with the modified DRK equation. Assuming no sample loss, this heat transfer-desorption hybrid model enabled us to estimate the cumulative total mass of the vapor released from the μPPI by the transient thermal desorption process. Then, we performed tests to explore the correlation between the heating duration and the desorption kinetics. Toluene was first loaded to the μPPI by passive sampling for 15 min at the concentration of 1 ppm. The total mass of the toluene released by the subsequent thermal desorption process was measured for various heating durations by the downstream GC/FID. We repeated tests for additional 2 different concentrations of 350 ppb and 270 ppb in order to thoroughly understand the desorption behavior of toluene within the μPPI and validate our analytical model. During the initial sampling process, the amounts of 496 ng, 175 ng, and 140 ng were sampled for 1 ppm, 350 ppb, and 270 ppb, respectively. The results show that the predictions from the coupled thermal desorption kinetic model agree with the experimental results with a ±10 % error. Both the theoretical prediction and the experimental results indicate that by the desorption process completes the release of 90% of the total mass of the sampled toluene within 3 s, which obviously results from the rapid thermal response of the μPPI. The quantitative characterization of the transient desorption behavior of toluene within the device cavity successfully validated our model.

4.3.3 Effect of Heating Rate on the Peak Band Broadening

Subsequently, we studied, both theoretically and experimentally, the effect of the heating rate of the integrated micro-heater on the injection peak band broadening. The real-time injection profile was numerically derived from the time derivative of the

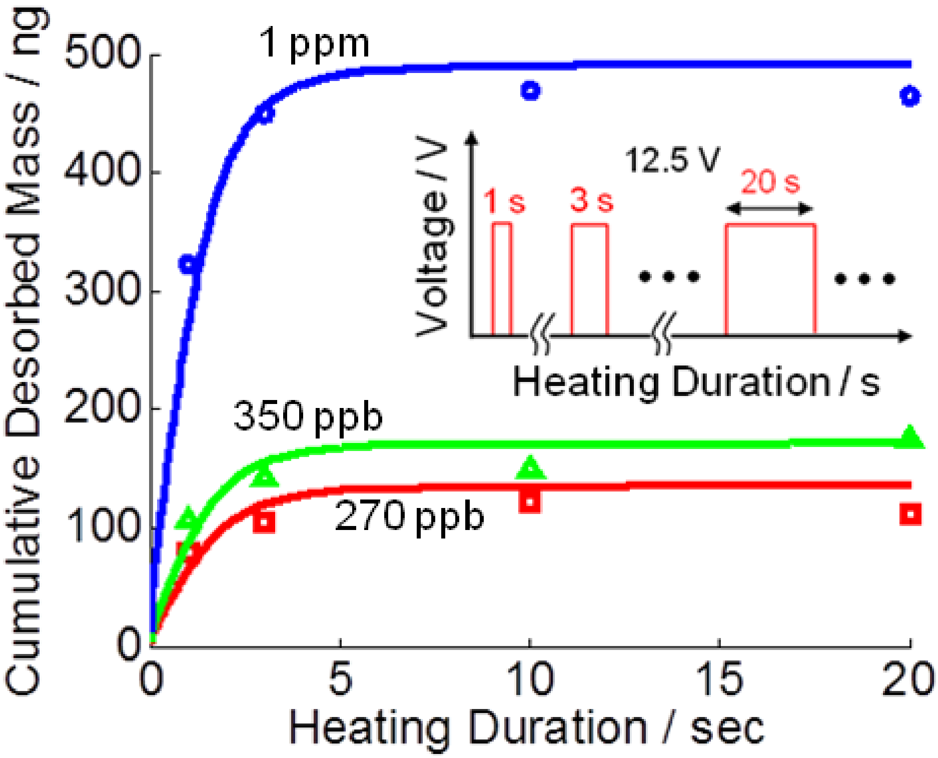

Figure 4.7 Theoretical and experimental plots of the total cumulative mass of toluene released from the μPPI by thermal desorption as a function of heating duration. They are given for toluene originally sampled for 15 min at 3 different concentrations of 270 ppb (red), 350 ppb (green), and 1 ppm (blue). The red squares (□), green triangles (Δ), blue circles (o) represent experimental data points obtained for different heating durations. The red, green, blue solid lines are the theoretical predictions at 270 ppb, 350 ppb, and 1 ppm, respectively. The inset shows the input voltage profiles applied to the micro-heater for a varying duration (i.e., heating duration) ranging from 1 s to 20 s. All of the off-state periods between the adjacent heating cycles involve sampling, desorption/injection, and cleaning processes.

theoretical cumulative desorption curve in Fig. 4.7. The standard deviation σ of the injection peak band was calculated to be 0.69 s by substituting the values of the test condition parameters, such as the gas flow rate, the length and radius of the interconnect tubing, and the diffusion coefficient of toluene, into equation 20 and equation 21. Then, solving equation 22 allowed us to obtain the theoretically predicted injection peak band signal of toluene.

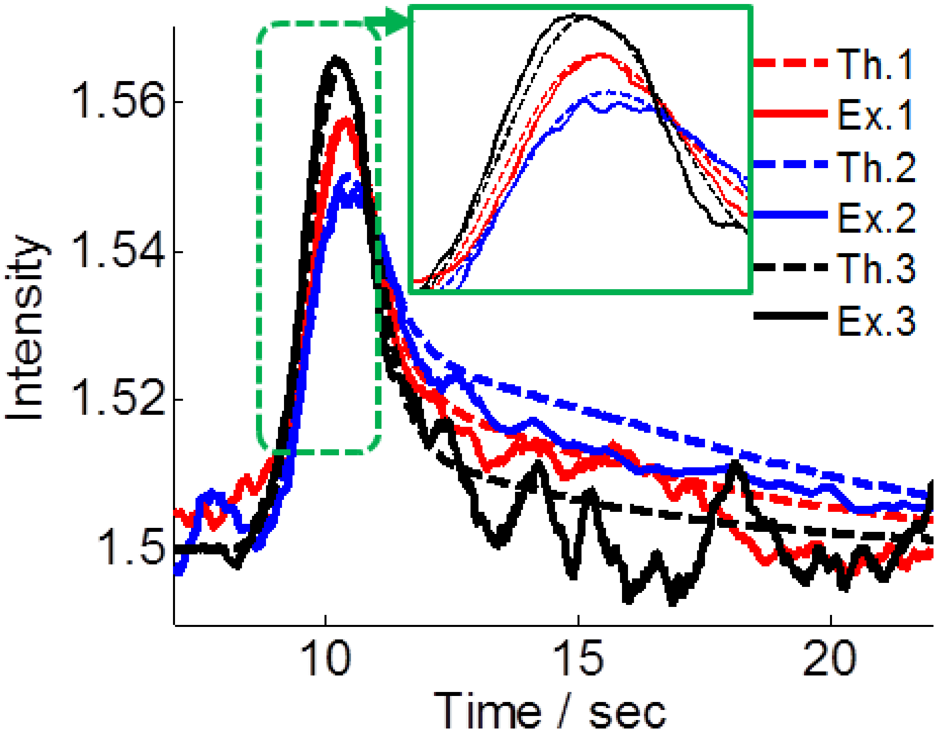

Figure 4.8 Theoretical and experimental plots of the injection peak band profile of toluene generated by the μPPI at different heating rates of 90 ˚C·s^{-1} (black), 80 ˚C·s^{-1} (red), and 70 ˚C·s^{-1} (blue).

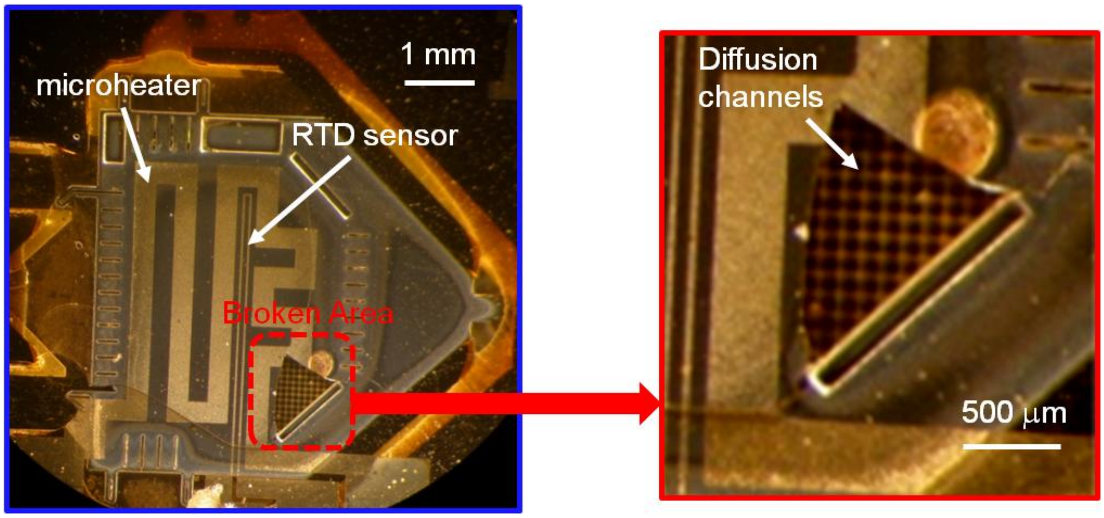

Figure 4.9 Optical image showing the thermomechanical structural failure of the μPPI after applying a high voltage of 25 V to the integrated micro-heater on the cavity floor membrane. This input voltage yields an average heating rate as high as 300 ˚C·s^{-1}. To prevent this device failure, we avoid setting the input heating rate at an arbitrarily high value.

Figure 4.8 shows the theoretically predicted injection peak band signals for 3 different heating rate conditions of 90 ˚C·s^{-1}, 80 ˚C·s^{-1}, and 70 ˚C·s^{-1} and those corresponding experimentally detected signals. Here, the higher heating rate is obviously more desirable for the peak intensity enhancement. There exists, however, the upper bound for the heating rate to prevent the device from breaking down due to a thermal shock. We observed that the μPPI failed when the average heating rate reached the value as high as 300 ˚C·s^{-1} (see the Figure 4.9). To avoid this, we selected the heating rate of 90 ˚C·s^{-1} at a relatively low power of 1.1 W as the upper bound. The signal profiles in the transient ramping and quickly declining regions up to 12 s match quite well the theoretical predictions (Fig. 4.8). After the period of 12 s in the plot, they decline slowly and show residual signal intensity. This signal behavior is due to the continuous release of the toluene from the device for a prolonged heating period in the thermal desorption process.

We quantified the peak tailing effect by taking the ratio of the maximum peak height (A) to the residual peak height (B) (Fig. 4.10) for the experimental result at the heating rate of 70 ˚C·s^{-1} and compared the experimental value to that of the theoretical curve. The stationary-phase free tubing used to interconnect the μPPI and the FP sensor removes the possibility of the peak tailing effect caused by the non-equilibrium interaction between the mobile and the stationary phase in a conventional capillary column. We choose *t* = 20 s in Fig. 4.8 as the reference time point at which the residual

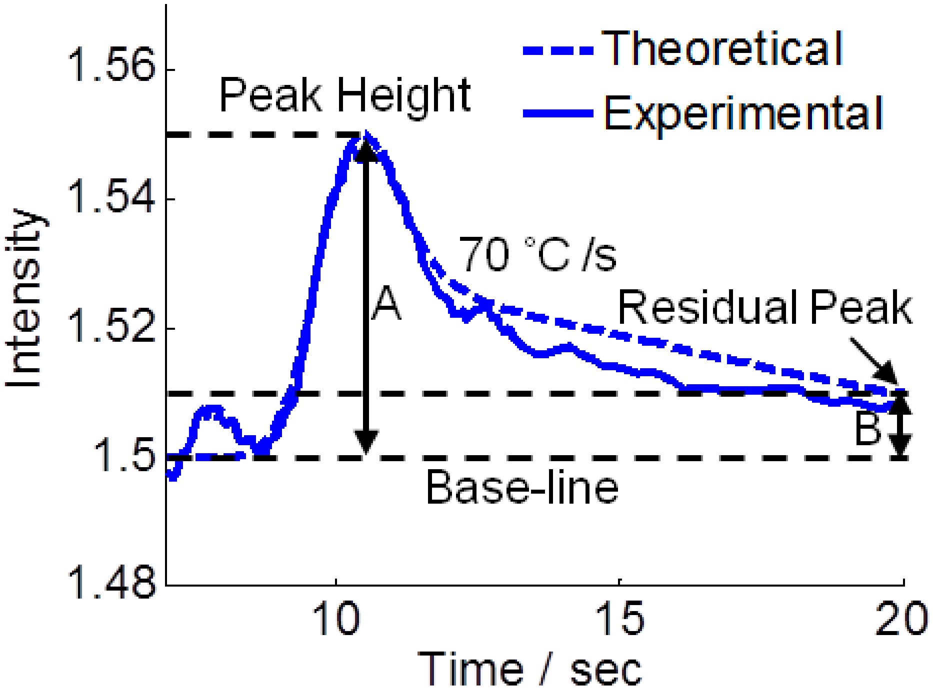

Figure 4.10 Plots of the theoretical and experimental injection peak band profiles of toluene at the heating rate of 70 ˚C·s^{-1}. These plots clearly show injection peak tailings affected by the heating rate.

peak height is determined. Additionally, the peak sharpness or the column efficiency was determined from the full width at half maximum (FWHM) values. Figure 4.11 both theoretically and experimentally shows the tailing effect and the FWHM values as functions of the heating rate. Again, the results indicate that the experimental data are in good agreement with the theoretical predictions. The higher heating rate leads to the smaller tailing effect as well as the shorter FWHM. The increase of heating rate from 70 ˚C·s^{-1} to 90 ˚C·s^{-1} enhances the peak intensity with the tailing effect reduced by 11.2 % in the experiment (11 % in the model prediction) and the FWHM reduced by 1.24 s in the experiment (1.2 s in the model prediction).

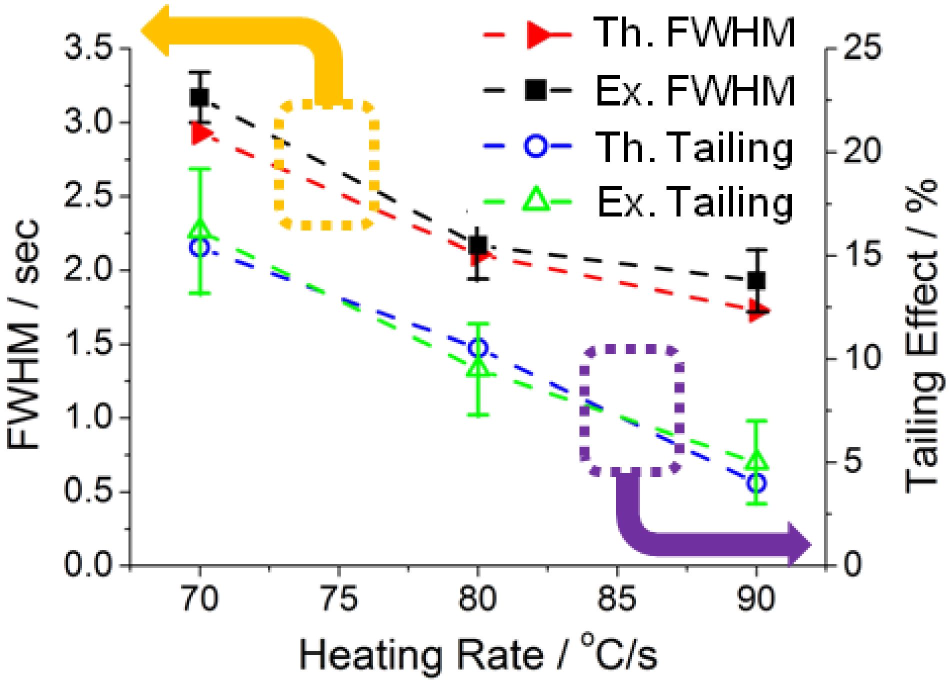

Figure 4.11 FWHM values and quantified injection peak tailing effect at different heating rates of 70 ˚C·s^{-1}, 80 ˚C·s^{-1}, and 90 ˚C·s^{-1}.

4.3.4 Effect of Heating Duration on the Maximum Injection Peak Intensity

Excessive energy consumption due to a prolonged heating duration is undesirable for the development of a portable chromatographic microsystem incorporating the μPPI. On the other hand, an insufficient heating duration also yields a weak injection band signal with incomplete desorption of vapors. As such, it is critical to precisely select the optimal heating duration to achieve the best vapor injection performance of the device with a quantitative understanding of this trade-off. To assess the effect of heating duration on the peak band intensity, the device was tested for various heating durations of

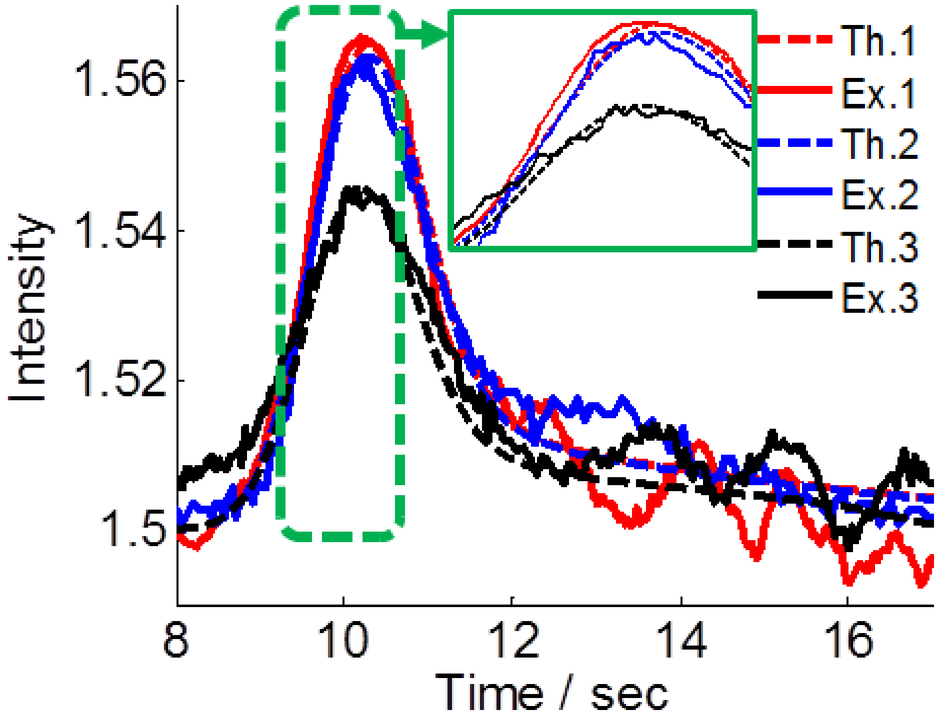

Figure 4.12 Theoretical and experimental plots of the injection peak band profile of toluene for different heating durations of 1 s (black), 3 s (blue), and 10 s (red).

1 s, 3 s, and 10 s at the heating power of 1.1 W (Fig. 4.12).

In this case, we also found reasonably good agreement between our theoretical prediction and experimental results. The experimental FWHM mean value increases slightly with the heating duration from 1.47 s to 1.83 s (Fig. 4.13). Accounting for the error bars in the experimental data, it is consistent with the observation that the variation among the theoretical FWHM values = 0.003 s is insignificant regardless of the heating duration. The maximum peak height for the heating duration of 1 s is 30 % less than the values for other heating durations of 3 s and 10 s (Fig. 4.12 and 4.13). The heating duration of 1 s, which is insufficient to complete the full release of the sampled toluene (Fig. 4.7), results in the small peak height, which is 35 % smaller than that for the heating duration of 10 s. In contrast, the maximum peak height for the heating duration of 3 s is

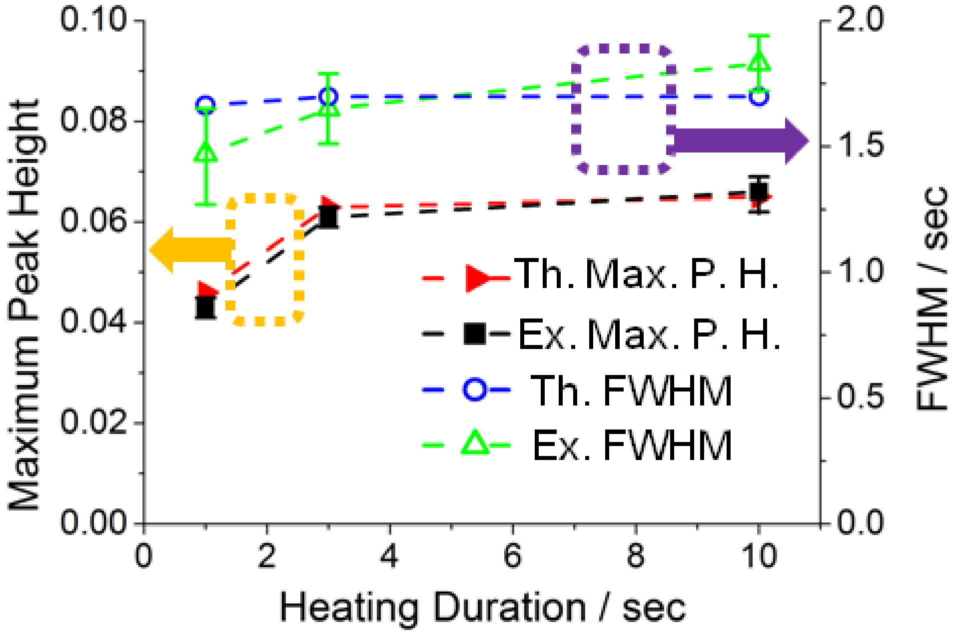

Figure 4.13 Maximum peak height and FWHM value for heating durations of 1s, 3 s, and 10 s.

only 3 % less than that for the heating duration of 10 s. It is shown that 70 % of the total energy consumption is saved by reducing the heating duration from 10 s to 3 s with the small decrease in the maximum peak height (Fig. 4.14). Thus, the heating duration of 3 s provides the optimal heating condition for our device to achieve low-power, high-intensity vapor injection.

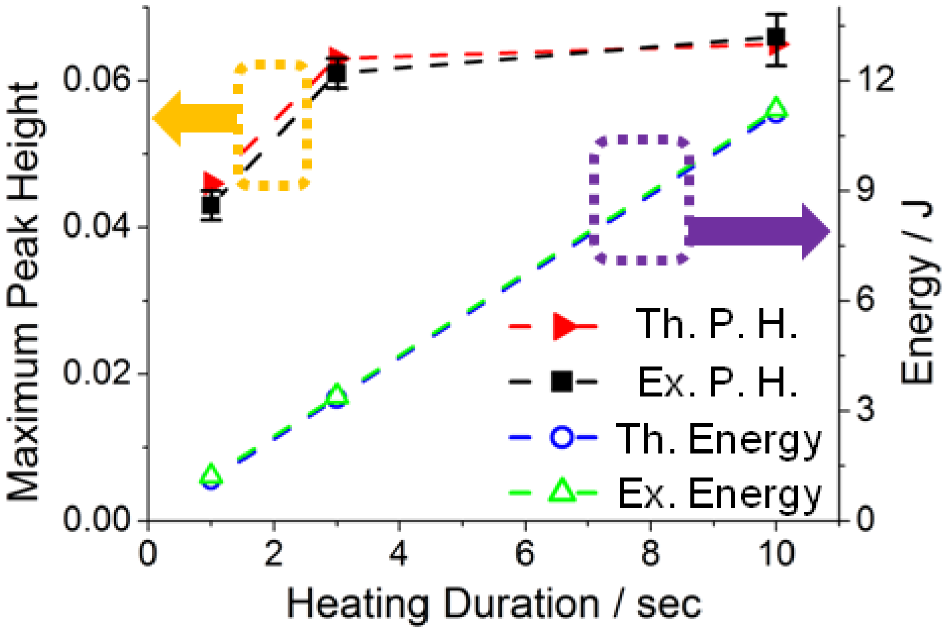

Figure 4.14 Maximum peak height and energy consumption for heating durations of 1 s, 3 s, and 10 s.

4.4 Summary

This chapter studies thermal desorption and delivery of toluene vapor by a microfabricated device that serves as a passive preconcentrator/injector of volatile organic compounds (VOCs) in gas chromatography (GC) analysis. Here, we develop a theoretical model simultaneously accounting for transient heat transfer and vapor desorption kinetics to quantitatively predict the microscale vapor sample release/injection performance of the device. We characterize the total mass and real-time peak band profile of toluene injected to a downstream inert tubing with various temporal heating profiles of the device's integrated micro-heater. The model predictions are in good agreement with experimental results from device characterization using an on-column optical fiber-based Fabry-Pérot gas sensor. Heated from room temperature to 300 ˚C within 3 s at a carrier gas flow rate of 10 mL/min, the device injects 90% of the originally collected toluene, forming a peak band profile with a full width at half maximum bandwidth as small as 1.69 s. The narrow-band injection suppresses the peak tailing effect and limits the total heating energy consumption to 3 J per cycle, which is less than 10% of conventional injection processes.

CHAPTER V

SAMPLING, INJECTION, AND SEPARATION PERFORMANCE FOR VOC MIXTURES

5.1 Introduction

Over the last decade, several laboratories have been developing gas chromatographic microsystems (μGCs) for *in-situ* analysis and *on-site* field monitoring of volatile organic compounds (VOCs). These μGC systems may represent the most promising technology for complex VOC mixture analyses in real-time air monitoring, point-of-care biomedical diagnostics, homeland security, and worker exposure assessment. Most μGC systems consist of fluidically interconnected subsystems: a preconcentrator/injector, a separation column, a detector, and a pump [10-14, 37]. These subsystems are typically microfabricated using silicon microelectromechanical system (MEMS) technology [8, 9, 18-36, 38-60]. Miniaturization enabled by microfabrication allows rapid temperature programming of the GC subsystems with low power, which is critical for the development of a battery-operated handheld GC system. In particular, a microfabricated preconcentrator (μ-preconcentrator) is one of the key components of a μGC system for its ability to enhance the system's detection sensitivity by trapping and accumulating low-concentration VOCs. Due to the limited sensitivity of existing gas sensors, a μGC system without a μ-preconcentrator is prohibited to detect VOCs at the parts-per-billion (ppb) concentration level, which is required in many applications. A μ-preconcentrator additionally serves as a vapor injector delivering plugs of the preconcentrated VOCs to a downstream separation column by thermal desorption. The injection sharpness critically affects the separation resolution of a GC system. Therefore, the device must be capable of generating sharp injection plugs. Microfabricated preconcentrator devices developed in previous studies [94] generally require substantial energy for both carrier gas pumping and VOC thermal injection.

In our previous work, we demonstrated diffusion-based passive sampling of low-concentration toluene using our on-chip device, namely the "microfabricated passive vapor preconcentrator/injector (μPPI)" [94] (Fig. 5. 1A). The μPPI first achieved a sampling rate of 9.1 mL/min for toluene in an air sample. Subsequently, temperature ramping of an integrated micro-heater allowed the μPPI to release and inject the collected vapor sample at a low heating power of ~ 1 W and a carrier gas flow rate of 50 mL/min with an injection sample loss < 5 %. The μPPI device is the *first* microfabricated GC component that has the potential of realizing battery-operated on-chip VOC sampling and injection because of its low power consumption. This device may open a way for highly energy efficient field-deployable GC analyses. However, our previous study was limited to use of the single VOC species (i.e., toluene) for the device characterization. Fully demonstrating the utility of the μPPI in GC analyses still requires a through characterization of the device’s performance using VOC mixtures.

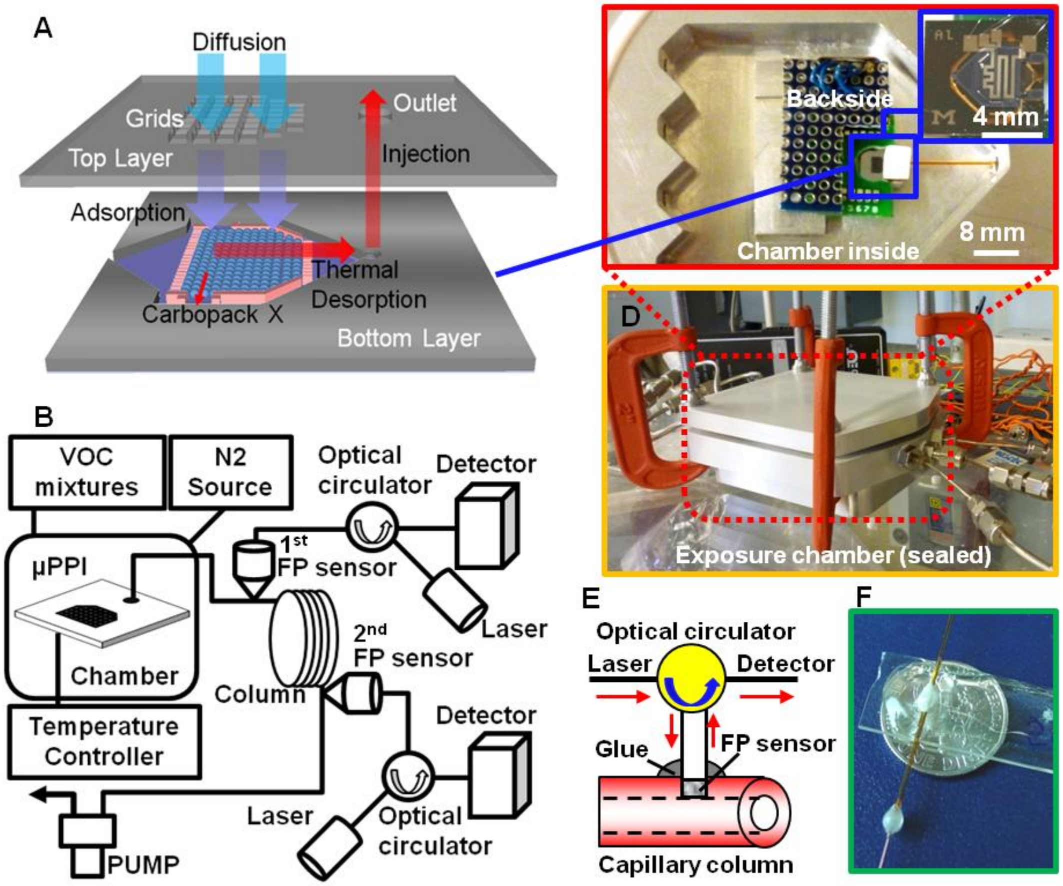

Figure 5.1 (A) Conceptual diagram of the μPPI showing the sampling of VOC mixtures by diffusion and thermal desorption/injection processes. The μPPI comprises two layer structures; the top layer incorporates vertical square diffusion channel grids for passive vapor sampling; and the bottom layer contains a membrane cavity structure with tapered entrance/exit on its two sides, pillar structures to retain the graphitized carbon granules inside, and an integrated heater and a resistance temperature detector (RTD) on its backside. (B) Schematic of the test setup incorporating two Fabry-Pérot (FP) interferometic optical gas sensors used to characterize the preconcentration, desorption/injection, and separation performance of the μPPI for VOC mixtures. (C) Optical image of the μPPI mounted in the exposure chamber. Inset images show the micro-heater and RTD sensor on the backside of the μPPI. (D) Optical image of the sealed exposure chamber. (E) Conceptual diagram of the on-column FP sensor showing its working principles. (F) Optical image of the FP optical gas sensor assembly.

In this chapter, we explore preconcentration, desorption/injection, and separation of VOC mixtures with a broad spectrum of analytes using the μPPI to demonstrate the general utility of the device. Toward this goal, we verify that the μPPI can (1) collect a quaternary mixture containing highly common VOC species as well as single individual compounds on the basis of a zero-power diffusion process, (2) sufficiently preconcentrate analyte VOCs to enhance detection sensitivity, and (3) generate a sharp peak pulse of these concentrated vapors by thermal desorption to achieve a sufficient vapor separation ability. To demonstrate the full μPPI-based GC operations, we have developed a custom GC system employing the device in front of a separation column and two on-column optical fiber-based Fabry-Pérot (FP) gas sensors at the both ends of the separation column (Fig. 5. 1B). These dual sensors detect *in situ* the vapor signals at both of the column inlet and outlet. This sensor arrangement provides the means to directly observe vapor mixture injection profiles of the μPPI as well as accurately measure the retention time for each analyte to take to pass through the separation column. This GC system permits quantitative differentiation and identification of the components of a quaternary VOC mixture with a much simpler fluidic setup than conventional GC instruments. To perform quantitative measurements, we first calibrate the signals of the optical sensors for each of 4 vapor analytes, each having different diffusivity, volatility, and affinity. We next determine the sampling rates for these analytes. Then, an optimal heating condition of the μPPI is explored to generate a sharp vapor injection profile leading to complete separation of the quaternary VOC mixture while preventing a device failure due to thermal shock. Finally, chromatogram peaks obtained by the complete separation are analyzed and quantified. This allows us to quantitatively characterize the detection sensitivity enhancement for each analyte species and the device's vapor sampling performance in the presence of competing adsorptions of the different VOC components in the quaternary mixture sample. With all the device functions for the VOC mixture sample verified, the μPPI proves its capability to enable low-power, signal-enhanced, high-fidelity analyses for its use in a μGC system.

5.2 Materials and Methods

This section discusses materials and methods used for fabricating and characterizing the designed micro-device. The device fabrication was performed at the Lurie Nanofabrication Facility (LNF) at the University of Michigan. The experiment entails calibration of the on-column FP sensor signal as a function of vapor mass, measurement of the sampling rate of VOCs in the μPPI, and separation of the VOC mixture with the custom GC system at varying micro-heating rates.

5.2.1 Materials

Our experiment used 4 different individual VOCs (benzene, TCE, toluene, and *m*-xylene) that represent a broad spectrum of VOCs ranging from low- to high-volatility compounds (8.29 - 95.2 *torr*. The detailed properties of these compounds are given in Table 5. 1. All VOC analytes with purity > 99 % were purchased from Sigma-Aldrich (St. Louis, MO) and were used as received. A non-polar dimethylpolysiloxane (PDMS) coated separation column (HP-1, i.d. = 250 μm) was obtained from Agilent Technologies Inc. (Santa Clara, CA). For GC separation tests, we prepared test atmospheres of VOC mixture comprising the 4 different analyte compounds (*i.e.*, benzene, TCE, toluene, and *m*-xylene) in the N_2 gas of a Tedlar bag of 10 L. The concentration of each component in this VOC mixture sample was 50 ppb. A small amount of each analyte equivalent to 50 ppb in the 10 liter N_2 gas was injected into the bag by a syringe. Carbopack Xs (C-X, specific area = 250 m^2/g, 60/80 mesh) graphitized carbon beads, which were used as the adsorbent materials of the μPPI, were purchased from Supelco (Belafonte, PA) and were used as the adsorbents packed in the μPPI. The separation column and C-Xs were preheated for cleaning at 250 ˚C before use.

	Properties		
VOC analyte	**p_v (torr)**	**D_0 (cm^2/s)**	**MW (g/mol)**
Benzene	**95.2**	**0.0932**	**78.11**
TCE	**69**	**0.0875**	**131.39**
Toluene	**28.4**	**0.0849**	**92.14**
***m*-xylene**	**8.29**	**0.0670**	**106.16**

Table 5.1. List of quaternary compounds and their vapor pressures (p_v), diffusion coefficients (D_0), and molecular weights (MW)

5.2.2 Experimental Setup

To demonstrate the general utility of the μPPI for VOC mixtures in a complete GC system, we modified our previous setup (Fig. 5. 1C and 5. 1D) used for characterizing the vapor injection by the μPPI in Chapter 4. As shown in Fig. 5. 1B, the μPPI-mounted exposure chamber system is fluidically interconnected to two on-column Fabry-Perot (FP) interferometirc optical sensors, a separation column, and a mini-pump. The VOC sample in the N_2 carrier gas is drawn into the system by a mini-diaphragm pump (BTC IIS, Parker, Cleveland, OH). The FP optical sensors were installed at the both ends of a 10 m long (250 μm (i.d.)) stationary phase coated tubular separation column (HP-1, Agilent, Santa Clara, CA). The incident light coming from the external laser source was coupled into the optical sensor through an optical circulator and then partially reflected on the metal layer and the interface of the PDMS layer and air, generating an interference spectrum. When the PDMS layer of the sensor is exposed to VOC analytes, the surface interaction between the polymer and the analytes causes a shift of the interference spectrum. This spectrum shift provides us with the real-time kinetic information of VOC analytes.

5.2.3 Microfabrication of the μPPI and the On-column Sensor

Detailed information on the processing steps of the μPPI device is provided in Chapter 3. The fabrication and assembly of the on-column FP sensor were also previously reported [94]. Briefly, the μPPI was fabricated using bulk micromachining based on growth of thin thermal oxide layer, Si deep reactive ion etch (DRIE), SiON dielectric thin-film deposition, integrated metallic heater/temperature sensor patterning, selective ethlenediamine pyrocatechol (EDP) wet etch of boron-doped silicon, and modified eutectic wafer bonding. The sensor was fabricated by sequential deposition of a metal layer, such as gold or silver, and a polydimethylsiloxane (PDMS) layer on the end-face of a single mode optical fiber to create a FP cavity (Fig. 5. 1E and 5. 1F).

5.2.4 Sensor Signal Calibration

The sensing signals rely on sorption characteristics between the PDMS layer of the optical sensor and VOC analytes. To quantitatively assess the performance of our custom GC setup we calibrated the on-column FP sensor signals for the 4 individual VOCs. We first removed the μPPI-mounted exposure chamber from the test setup, and then connected a Tedlar bag containing benzene vapor of 3 ppm to the setup. The benzene sample in the Tedlar bag was then injected into the first on-column FP optical sensor, installed at the inlet of the separation column, for 10 s at a flow rate of ~1.8 mL/min generated by the mini-pump. The peak signal of the injected vapor was monitored in real-time and was recorded at a rate of 20 Hz, using a customized LabView program. The same tests were consecutively performed for the additional 4 different concentrations of 4 ppm, 5ppm, 6ppm, and 10 ppm in order to obtain a calibration curve showing the correlation of the peak area and the concentration of analyte (benzene) in the tested sample volume. The vapor mass was calculated from the concentration and the sample volume used (sample injection time × flow rate). We then repeated these tests for other analytes of TCE, toluene, and *m*-xylene.

5.2.5 Sampling Rate Measurement with the μPPI Device

To quantify the μPPI's passive vapor sampling capability upon exposure to various VOCs, we steadily passed each of the 4 different analytes (benzene, TCE, toluene, and *m*-xylene) through the exposure chamber containing the device for discrete periods of 15, 30, 45, 60, or 90 min while maintaining each analyte concentration at 500 ppb. In this particular test, we removed the separation column and the second on-column FP optical sensor, installed at the outlet of the separation column, from the setup and only used the first on-column FP sensor for detection. After each sampling was completed, we covered the diffusion channels of the μPPI top layer with a glass, and next purged the chamber for 1 min with nitrogen gas at ~ 1 L/min to remove any residual VOC analyte. The N_2 flow through the chamber was then stopped and we rapidly heated the μPPI from room temperature to ~ 300 ˚C for 30 s to desorb the trapped vapors. The released vapors were drawn through the device outlet port to the sensor at a flow rate of 10 mL/min by the mini-pump, and the mass of each vapor injected by the μPPI was measured using the on-column FP sensor.

5.2.6 VOC Mixture Separation

The VOC mixture sample was passed through the exposure chamber for 60 min by the mini-pump and was collected by the μPPI. The analytes were passively trapped in the μPPI at a constant sampling rate determined by their own diffusivity. We next temporally covered the top layer of the device with a glass chip to avoid sample loss from the diffusion channels during the thermal desorption. The device was then heated up to ~ 300 ˚C at varying heating rates of the integrated Ti/Pt meander-line micro-heater. The thermally desorbed analytes were delivered to the first on-column FP optical sensor at a flow rate of ~ 1.8 mL/min, which is typically used in GC analysis, during the thermal desorption from the μPPI. The first sensor detected superimposed injection band peaks of the four thermally desorbed VOCs from the μPPI. These vapors were then drawn into the separation column which was maintained at ~ 80 ˚C, and were separated due to the different analyte volatilities. Finally, we obtained complementary chromatograms for the VOC mixture using the second on-column FP optical sensor.

5.3 Results and Discussion

This chapter presents results from the on-column FP sensor calibration and the sampling rate measurement for each VOC analyte, and successfully demonstrates injection and complete separation of the VOC mixture at an optimal heating rate of the μPPI. We obtained sensor calibration curves indicating the peak area as a function of the sample mass for the 4 vapor compounds. From the chromatogram data, our study determined the mass fraction of the quaternary VOC mixture collected by the μPPI device. We next explored the optimal heating condition of the μPPI, which resulted in a high-resolution chromatogram indicating a full separation of 4 analyte compounds. By comparing mass uptake data for single-analyte sampling and mixture sampling, we *quantitatively* assess the interference among the mixed 4 analyte compounds during the desorption process at the adsorbents of the μPPI.

5.3.1 Calibration of the On-column FP Optical Sensor

Our results show unique responses of the on-column FP optical gas sensor to the 4 different analyte compounds. A calibration curve for each analyte is provided by the correlation between the area of the sensor signal peak and the analyte concentration in the tested sample volume, which enables the quantitative measurement of vapor mass from the chromatograms. Figure 5. 2 shows a set of calibration curves for 4 individual vapors of benzene, TCE, toluene, and *m*-xylene obtained by collecting samples for 10 s at a flow rate of ~ 2 mL/min for 5 different concentrations of 3, 4, 5, 6, or 10 ppm. The sampled masses achieved from 3 ppm (1.0 ppm·mL) to 10 ppm (3.3 ppm·mL) range from 3.5 ng to 11.7 ng for benzene, 5.8 ng to 19.4 ng for TCE, 3.7 ng to 12.2 ng for toluene, and 4.6 ng to 15.3 ng for *m*-xylene. As shown in Fig. 5. 2, peak responses increase linearly with concentration ($r^2 > 0.99$). At a given concentration of 6 ppm (2.0 ppm·mL), the corresponding peak areas are 0.202 (benzene), 0.296 (TCE), 0.399 (toluene), and 0.717 (*m*-xylene).

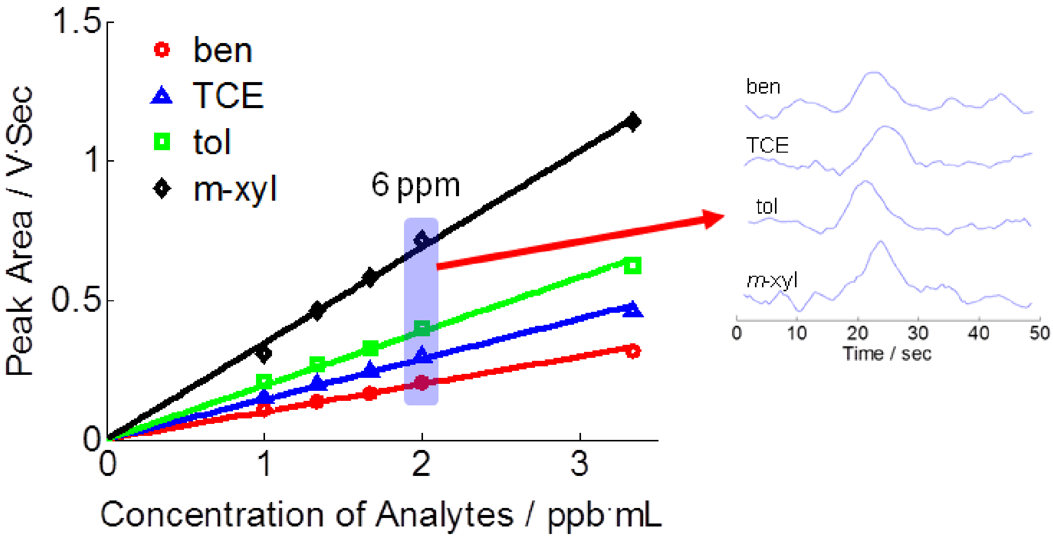

Figure 5.2 Calibration curves generated from injecting different concentrations of 4 individual analytes in Tedlar bags to the on-column FP optical sensor. Samples were injected to the sensor for 10 s at 2 mL/min. The tested concentrations ranged from 3 ppm (1.0 ppm·mL) to 10 ppm (3.3 ppm·mL). Linear regression r^2 values for all analytes are all > 0.99. Inset shows chromatograms of 4 individual analytes (benzene, TCE, toluene, and *m*-xylene) at the concentration of 6 ppm (2 ppm·mL).

5.3.2 Sampling Rate Tests for VOCs

To show that the μPPI can effectively trap a broad spectrum of analytes, we performed tests of the sampling rate for each of 4 individual VOC analytes of benzene, TCE, toluene, and m-xylene. Figure 5. 3 shows plots of sampled mass *versus* sampling time from 15 to 90 min for each analyte. In all cases, the standard deviation was less than 10 %. All the sampled mass in the μPPI was delivered to the optical sensor with no residual analyte in the chamber headspace because we covered the diffusional grids of the top layer with a glass chip. Thus, there was no vapor loss escaping through the diffusion channels by back-diffusion during the desorption process. The results indicate that the sampling performance of the μPPI is consistent and reproducible for each analyte over the entire series of experiments.

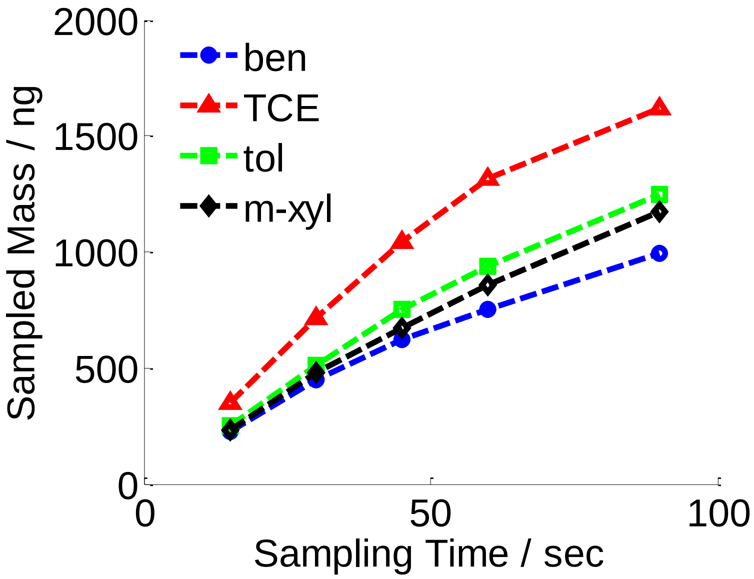

Figure 5.3 Plots of the mass trapped and thermally desorbed by the μPPI as a function of sampling time for each analyte at a concentration of 500 ppb and a suction flow rate of 10 mL/min. The reduction in the mass uptake rate beyond 45 minutes for all analytes reflects the decline of the sampling rate as the number of available surface sites on the adsorbents get decreased.

For all the VOC analytes tested in the experiments, Figure 5. 3 indicates that the mass uptake rates are constant up to ~ 45 min ($r^2 > 0.99$) at a given concentration of 500 ppb. Sampling rates of 8.7 mL/min, 8.6 mL/min, 9.0 mL/min, and 6.9 mL/min were obtained from the slopes of the linear region of the curves for benzene, TCE, toluene, and *m*-xylene, respectively. Using the sampling rate equation in Chapter 3 and the diffusion coefficients of these analytes in Table 5. 1, the theoretical prediction values are 10.2 mL/min (benzene), 9.6 mL/min (TCE), 9.3 mL/min (toluene), and 7.3 mL/min (*m*-

xylene). These experimental values are 3 % (toluene, 9.0 mL/min) - 15 % (benzene, 8.7 mL/min) lower than the theoretical predictions. The corresponding mass uptake rates for the experimental data are 13.9 ng/min (benzene), 23.2 ng/min (TCE), 16.7 ng/min (toluene), and 15.0 ng/min (*m*-xylene). The discrepancies between the experimental sampling rate and the theoretical prediction are more significant for benzene (15 %) and TCE (10 %) than the other analytes (3-5 %). By taking the narrow linear region up to 30 min, the discrepancies for benzene and TCE become 9 % (9.3 mL/min) and 7 % (8.9 mL/min) lower than predicted by the sampling rate equation, respectively. Yet the errors for these analytes are still high, which might be caused by relatively lower responses to the optical sensor due to their higher volatilities.

Beyond ~ 45 min, the μPPI continues to trap the vapor sample, but at a lower sampling rate for each analyte. This sampling process is expected to continue to decrease until the surface adsorption sites on the adsorbents (C-Xs) get completely filled. At the sampling time of 90 min, the mass uptakes for 4 individual analytes of benzene, TCE, toluene, and *m*-xylene were 0.99 μg, 1.62 μg, 1.25 μg, and 1.17 μg, respectively. These values, sequentially, are 68 %, 70 %, 80 %, and 82 % of the total amounts expected (*i.e.*, benzene: 1.47 μg, TCE: 2.33 μg, toluene: 1.55 μg, *m*-xylene: 1.43 μg) assuming the designed constant sampling rate on each of analytes.

5.3.3 VOC Mixture Injection by the μPPI

Our previous study in Chapter 4 indicates that a higher heating rate yields a sharper injection profile with the μPPI. A sharp injection profile is expected to provide

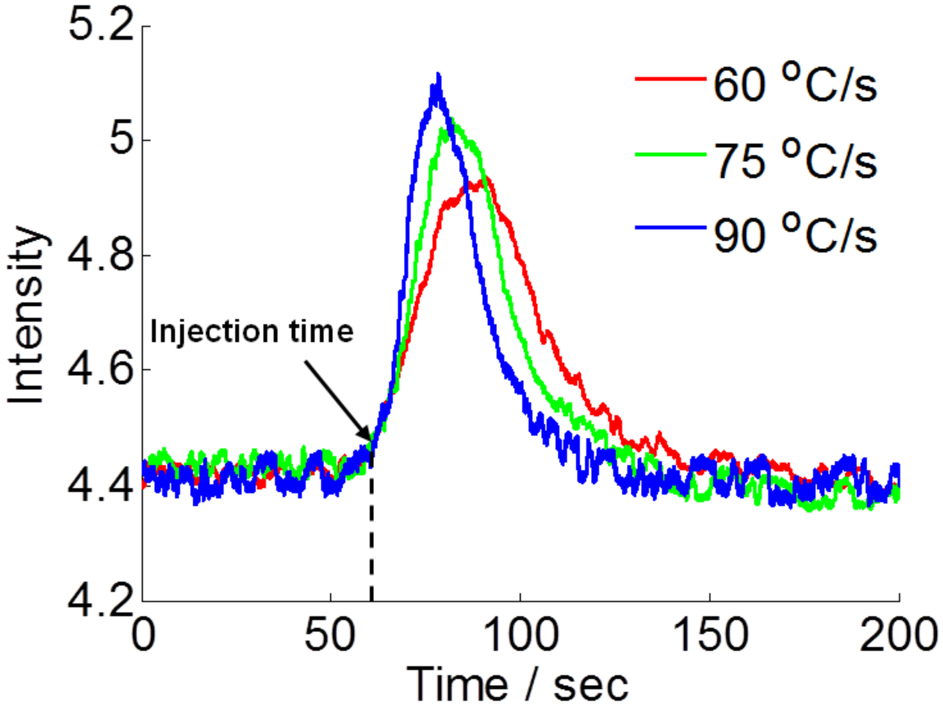

Figure 5.4 Experimental plots of the superimposed peak signals of the released VOC mixtures generated by the μPPI at the different heating rates of 60 ˚C/s (red), 75 ˚C/s (green), and 90 ˚C/s (blue). The released/injected peak band signals of VOC analytes are detected at the first FP optical sensor in the custom GC system prior to separation. The reference time point (t = 0) is the time at which the heating power starts to be applied to the μPPI for thermal desorption.

high chromatogram resolution. However, a heating rate exceeding a certain value results in a device failure due to thermal shock. Thus, we monitored *in situ* vapor injection profiles of the μPPI using the first on-column sensor installed at the column inlet by gradually increasing the heating rate from 60 ˚C/s to a higher value. Here, the injection time (t_i), i.e., the time for the desorbed analytes to travel from the μPPI to the column inlet, was monitored at the heating rates of 60 ˚C/s, 75 ˚C/s, and 90 ˚C/s. (Figure 5. 4). As expected from the result in Chapter 4, the superimposed peak signal enhancement of VOC mixtures was reflected in the decrease from 34.3 s to 20.8 s in the full width at half maximum (FWHM) value along with the increase of heating rate from 60 ˚C/s to 90 ˚C/s. It was also shown that the peak tailings of VOC mixtures were decreased by increasing the heating rate. Based on these superimposed peak signal data, we found that the injection time was consistently ~ 60 s regardless of the heating rates. The accurate retention time data obtained by our GC setup promises to facilitate the differentiation and identification of the compounds.

5.3.4 VOC Mixture Analysis

Figure 5. 5 shows the chromatograms corresponding to the injection profiles at the heating rates of 60 ˚C/s (0.7 W), 75 ˚C/s (0.9 W), and 90 ˚C/s (1.1 W). The 4 different analyte VOCs injected into the column were separated in < 400 s by means of their different interactions with the stationary phase of the column. The chromatogram data were achieved from the second on-column FP optical sensor in the optofluidic GC system. The accurate retention time for each separated analyte was obtained by subtracting t_i from the time (t_o) it took for the peak height signal of each vapor monitored at the column outlet to appear. Benzene and TCE have similar retention time values of ~ 59 s (t_o: 119 s) and ~ 90 s (t_o: 150 s), respectively, shorter than the other analytes of toluene (~ 188 s (t_o: 248 s)) and *m*-xylene (~ 319 s (t_o: 379 s)). Figure 5. 5A and 5. 5B indicate that the peak signals of benzene and TCE overlapped with each other at both heating rates of 60 ˚C/s and 70 ˚C/s generated from the μPPI while toluene and *m*-xylene were clearly separated even at the lower heating rate of 60 ˚C/s. For the maximum heating rate condition of 90 ˚C/s, the eluted peak of benzene was distinctly differentiated

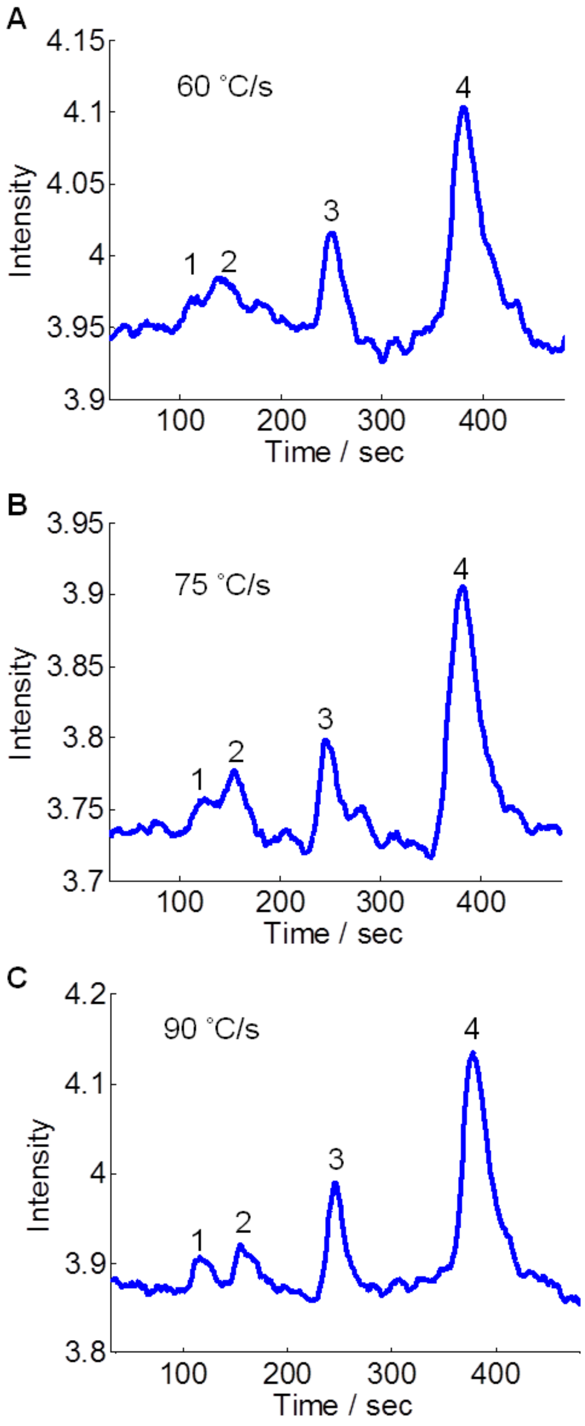

Figure 5.5 Chromatograms from the second on-column FP optical gas sensor for the 3 different heating rates of (A) 60 ˚C/s, (B) 75 ˚C/s, and (C) 90 ˚C/s, generated by the μPPI. Peak assignments are as follows: 1, benzene; 2, trichloroethylene (TCE); 3, toluene; 4, *m*-xylene.

from that of TCE (Fig. 5. 5C). The peak height was also significantly enhanced by ~ 73 %, ~ 37 %, ~ 70 %, and ~ 52 % for benzene, TCE, toluene, and *m*-xylene, respectively, compared to that for the lowest heating rate of 60 ˚C/s. Here, it would be possible to obtain more enhanced chromatograms at a higher heating rate than 90 ˚C/s. However, we used this heating rate for our further analyses as a sufficiently high value to avoid the aforementioned thermal damage of the device.

5.3.5 Analysis of VOC Mixture Adsorption by the μPPI

Low volatility compounds are often easily trapped on the adsorption sites of the adsorbents at room temperature, so-called cold trapping, since the analytes have been cooled below their boiling points. The tested mixture sample contains a broad spectrum of VOCs with different vapor pressures, diffusion coefficients, and affinities. Significant competing interferences among these compounds are expected during the sampling process. To examine these interferences, we calculated the mass of each analyte collected by the μPPI from the chromatogram peak signal obtained at the heating rate of 90 ˚C/s. The calculation shows that the masses of benzene, TCE, toluene, and *m*-xylene for the sampling time of 60 min and the concentration of 50 ppb were 30.6 ng, 46.5 ng, 55.1 ng, and 92.1 ng, respectively. Figure 5. 6A shows the mass uptake distribution of the compounds adsorbed on the surface of the adsorbents in the μPPI. The device trapped the mixture in the mass ratio of 13.6 % for benzene, 20.7 % for TCE, 24.6 % for toluene, and 41.1 % for *m*-xylene. The experimental mass uptake for each analyte was reduced by 68.8 % in benzene, 69.8 % in TCE, 47.6 % in toluene, and 5 % in *m*-xylene in comparison to the mass uptake calculated by the theoretical sampling rate on the assumption of the single analyte sampling (Figure 5. 6B). These results demonstrate that the μPPI can trap all the quaternary mixtures with particular adsorption fractions although the effective sampling rate for each analyte is consequently reduced.

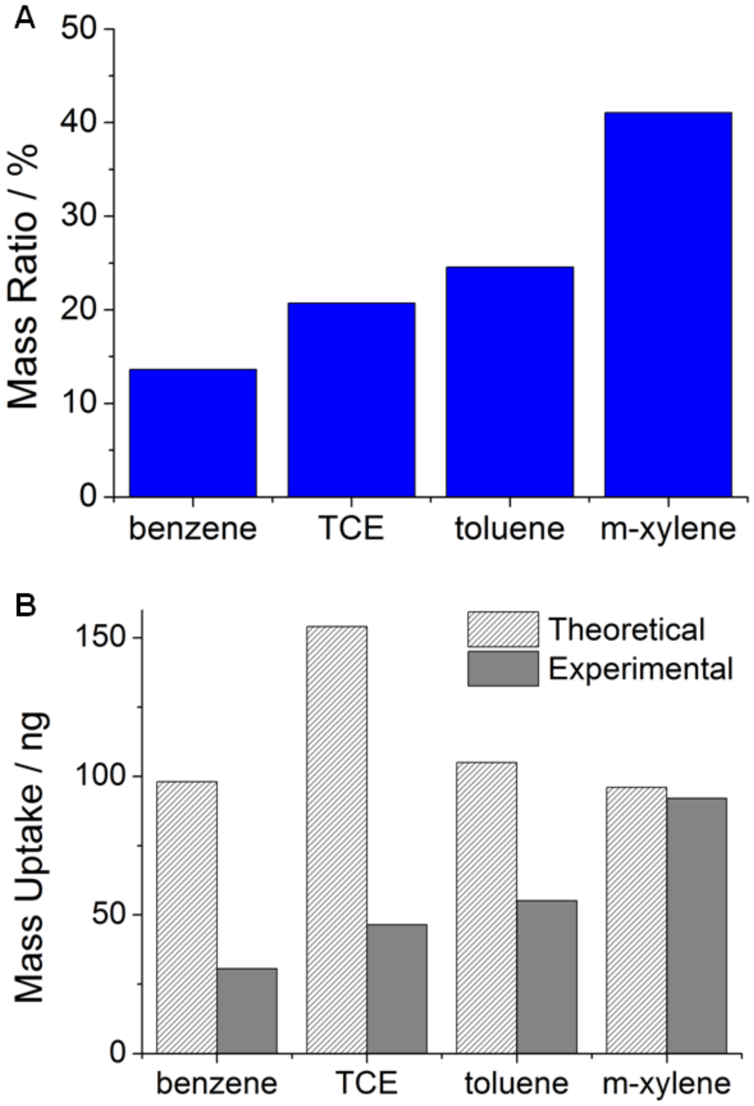

Figure 5.6 (A) Mass uptake distribution of the compounds of the quaternary mixture adsorbed on the surface of the adsorbents and (B) theoretically predicted mass uptake and experimentally obtained mass uptake for the sampling time of 60 min at the concentration of 50 ppb.

5.4 Summary

This chapter studies the applicability of a microfabricated passive preconcentrator/injector (μPPI) for its general utility in a gas chromatographic microsystem (μGC). This study shows that the μPPI enables diffusion-based passive sampling performance of the μPPI for low concentrations of volatile organic compound (VOC) analytes of benzene, TCE, toluene, and *m*-xylene. Using an optofluidic GC system incorporating the μPPI and dual on-column optical sensors, we *quantitatively* analyze the chromatographic separation resolution of the system with the output signals of the optical sensors calibrated for each test VOC analyte. From the chromatogram, the μPPI achieves high sampling rates of 8.7, 8.6, 9.0, and 6.9 mL/min for benzene, TCE, toluene, and *m*-xylene, respectively, for up to ~ 45 min at a concentration of ~ 500 ppb. The study identifies an optimal heating condition of 90 ˚C/s of the μPPI that results in separation resolution allowing the quaternary VOC mixture to be completely separated. For the sampling time of 60 min at the concentration of 50 ppb, the μPPI traps the mixture in the mass-ratio of 13.6 % for benzene, 20.7 % for TCE, 24.6 % for toluene, and 41.1 % for *m*-xylene. Results show that analyzing each chromatogram peak enables us to characterize the adsorption fractions of VOC species with different vapor pressures and affinities within the μPPI.

CHAPTER VI

CONCLUSIONS AND FUTURE WORKS

6.1 Summary of Thesis

6.1.1 Passive vapor sampling of microfabricated preconcentrator/ injector

This thesis study reports on the first development of a microfabricated passive VOC sampler. The µPPI also has an integrated resistive heater that permits *in situ* thermal desorption of captured vapor samples. The results presented demonstrate that the µPPI can capture low-concentration VOCs from the air with zero power dissipation (i.e., without active pumping) at a known and predictable rate. Efficient thermal desorption using the integrated heater and injection of discrete samples to downstream components (with pumping) have also been documented.

The sampling rate of 9.1 mL/min observed for the test vapor, toluene, is remarkably high given the size of the device, and similar rates would be expected from numerous other vapors with comparable diffusion coefficients in air. Thus, sufficient mass can be collected within a few minutes from environments containing low- or sub-ppm analyte for detection. The linear sampling range can be maintained is a function of the vapor concentration and its affinity for the adsorbent material packed in the device. For 1 ppm of toluene and the graphitized carbon adsorbent, Carbopack X, used in the μPPI, we have shown that sampling is maintained at a constant rate for 30 minutes prior to having to thermally desorb the sample and regenerate the adsorbent surface. More than 1 million sampling/desorption cycles are possible without any apparent degradation in performance. These sufficient passive sampling performance and thermal reliability meet the need for use of the μPPI in field-deployable μGC systems for personal exposure monitoring to assess the health impacts of VOCs.

The experimental sampling rate is in excellent agreement with theory prediction based on Fickian diffusion, and the heating power dissipation and capture efficiency of thermally desorbed samples are also in close agreement with the values predicted by the heat transfer and fluid dynamic models. These models guide the device design and operating parameters.

6.1.2 Impact of microscale on-chip heating on vapor release and injection

This chapter presents a quantitative analysis of the impact of microscale heating on the performance of the μPPI, our microfabricated device achieving on-chip vapor sample preconcentraion and injection. We have characterized the total mass of toluene released from the device by thermal desorption as a function of heating duration. This study is the *first* to quantitatively show the effect of thermal desorption on injection peak tailings and signal intensity. Our analytical model accounting for heat transfer, temperature dependent desorption kinetics, and peak band broadening well predicts the real-time vapor peak band signal profiles in good agreement with experiment. The small thermal mass of the membrane cavity structure of the μPPI realizes the device's significantly rapid heating response; it reaches 250 ˚C and 300 ˚C from room temperature within ~0.3 s and 3 s, respectively, with the micro-heater power of 1.1 W. The heating response of the μPPI is well predicted by our lumped thermal model with an error of < 2 %. As a result of the rapid thermal response, more than 90 % of toluene can be released from the graphitized nonporous carbon adsorbent (Carbopack X) of the μPPI within 3 s.

Furthermore, our study has investigated the effects of the heating rate and duration on the injection peak band signals by both theory and experiment. We have quantitatively shown that a higher heating rate increases the injection peak band sharpness and height. A higher heating rate also suppresses injection peak tailings, which would severely limit the ability to separate VOC mixtures with a GC capillary column connected to the device. Excessive thermal desorption of toluene with the μPPI significantly wastes energy. A careful analysis has allowed us to determine the optimal heating conditions to achieve the maximum signal detection sensitivity and chromatographic resolution at minimum energy consumption (< 10% of conventional cases).

6.1.3 Sampling, injection, and separation performance for VOC mixtures

This chapter demonstrated the general utility of the μPPI in a GC system. We characterized the passive preconcentration performance of the device for 4 individual VOC analytes at 500 ppb. Our fluidically simplified custom GC system incorporating the dual on-column optical sensors was capable of observing vapor injection profiles upon the thermal desorption process using the μPPI. The precise chromatographic retention time data obtained for the system facilitated the identification of each component of the VOC mixtures. The calibration data of the optical sensor enabled the quantitative assessment of the chromatographic separation resolution. The optimal heating condition of 90 ˚C/s was determined to achieve complete VOC separations while avoiding thermal shock to the μPPI device. From the chromatogram peak analysis, we determined the adsorption fraction (selective adsorption) of the quaternary mixture to study the interference among the analytes during the adsorption process.

The sampling rates of 8.7 mL/min, 8.6 mL/min, 9.0 mL/min, and 6.9 mL/min observed for the test VOC analytes of benzene, TCE, toluene, and *m*-xylene, respectively, were remarkably high and in good agreement with theoretical predictions (< 15 % error) for the linear sampling region up to 45 minutes. Thus, sufficient masses of low-concentration VOC analytes can be collected for GC analysis within a few minutes from the environment by virtue of passive diffusion-driven sampling. With the sampling time of 60 min, the C-Xs in the μPPI adsorbed the quaternary mixture at the weight ratio of 13.6 % in benzene, 20.7 % in TCE, 24.6 % in toluene, and 41.1 % in *m*-xylene.

Compared to the predicted mass uptake for each analyte, which was calculated from the theoretical sampling rate for the single vapor sampling, we estimated that the mass ratio would be 31.2 % in benzene, 30.2 % in TCE, 52.4 % in toluene, and 95 % in *m*-xylene if no analyte interference occurred. It follows that the compounds with lower volatility tend to more occupy sorption sites on the adsorbent surface than those with higher volatility in the sampling process. In summary, this study validated the general utility of the μPPI in a μGC system using the quaternary vapor mixture representing a broad spectrum of VOCs. We demonstrated that the device reliably collected vapor mixtures without any power requirements and permitted high-resolution chromatographic separation for the mixtures with signal enhancement.

6.2 Future Research and Applications

The continued study on the μPPI promises to have prominent impact on several research fields. Potential future work can explore the following three features: (1) assessment of the influence of the sampling time on multiplexed VOC analysis, (2) reduction of sampling time for high-speed preconcentration of low-concentration analytes in a GC system, and (3) full integration of our μPPI into a battery-operated micro gas chromatography system (system integration).

6.2.1 Adsorption preference of the adsorbents for each component of VOC mixtures

To determine if the adsorbents effectively capture VOC mixtures for separation and detection, accurate data for the adsorbents indicating their gas mixture adsorption are required. Each analyte has a different vapor pressure and interaction with adsorbents. When mixed with other compounds, the sampling rate of reduction is expected to be lower than that of a pure sample. This sampling rate is attributed to competition among the compounds for surface sites during the adsorption process. The time for the adsorbent to become saturated with the analyte in a mixture sample is expected to be shorter than in a pure sample. This saturation time is called “breakthrough.” When the sampling time exceeds the breakthrough, further analyte sampling for the mixture no longer contributes to increase the preconcentration gain. For this reason, determination of the optimal sampling time for each analyte in a given VOC mixture is required to avoid reaching the breakthrough. The optimal sampling time used in the device operation reduces the total analysis time, thus enabling a fast analysis desirable for a portable microanalytical system.

In this thesis work, we have individually characterized the passive sampling rate of the μPPI for each of four VOCs. Our study further determined the preferential adsorption of the components of a quaternary VOC mixture by the adsorbent at a sampling time of 60 min. The result suggests that low-volatility compounds more preferentially occupy the adsorbent surface sites than high-volatility compounds. However, our current data are insufficient for us to fully determine the breakthrough of each analyte in VOC mixtures. As we are unable to assess how the sampling time affects the reduction in the analyte's effective sampling rate. Therefore, it is necessary to repeat the device characterization for several different sampling times. To avoid injection peak tailings, the test should be repeated at the optimal heating condition of 90 ˚C/s for all different sampling time conditions (15, 30, 45, 60, and 90 min), followed by chromatogram peak analysis to determine the breakthrough of each analyte of VOC mixtures. These experiments will provide insight into the preferential adsorption of the VOC mixture components within the μPPI and its effect on the sampling rate of each analyte. From this study, we can finally optimize the sampling time enabling the fast analysis time which is useful for the realization of a μGC system incorporating the μPPI device.

6.2.2 Rapid sampling and preconcentraiton of low-concentration vapor compounds

Another future study will explore the device’s performance for high-speed preconcentration and separation of VOC mixtures at concentrations as low as sub-ppb. Real-time *in situ* gas monitoring is very crucial especially when the toxicity of a particular VOC imposes immediate risks on human health. In this case, a significant reduction in the sampling time is needed as it dominates the total GC analysis time. Sampling analytes at sub-ppb by the current μPPI design may typically take a few hours. To reduce the sampling time for the analytes at such a low concentration, we could redesign the diffusion channels, change the adsorbent dimensions, or replace the adsorbent with a new material. For example, diffusion channels with a shorter length and a larger cross-sectional area could increase the sampling rate. But this approach would be challenging from the device manufacturing point. The device fabrication would require a thinner Si wafer (< 200 μm) with numerous apertures. Such a wafer could easily break during wafer bonding and dicing processes. A promising alternative method would be to utilize carbon nano-tubes (CNTs) vertically grown from the μPPI cavity floor as the adsorbents. Controlling the CNT synthesis process permits adjusting of the analyte diffusion length for the passive sampling process. A higher sampling rate can be achieved by reducing the diffusion length with longer CNTs. In addition, the use of CNTs as the adsorbent significantly enhances the thermal response of the μPPI by the expected increase of the thermal contact conductance between the adsorbents and the device cavity floor. This approach will also contribute to shorten the total analysis time of the GC system incorporating the μPPI.

6.2.3 System integration

Our ultimate goal is to demonstrate a battery-operated gas chromatographic microsystem with the μPPI for fully field-deployable VOC detection under a complex environment. To achieve this goal, a complete μGC system comprising the μPPI, a microcolumn, a microsensor, a micropump, and a battery needs to be fabricated and assembled together. The elimination of the energy used in collecting sample by a pump, which is the most energy-hungry step in the GC analysis, represents perhaps the most promising technological advancement towards developing a battery-operated microanalytical system. Furthermore, innovative packaging and fluidic interconnection schemes need to be explored for the aimed system integration. Ultimately, a hand-held μGC system incorporating the μPPI could be effectively utilized for personal exposure monitoring to study the impact of VOC exposure on human health.

APPENDICES

Appendix I

Top Layer Fabrication

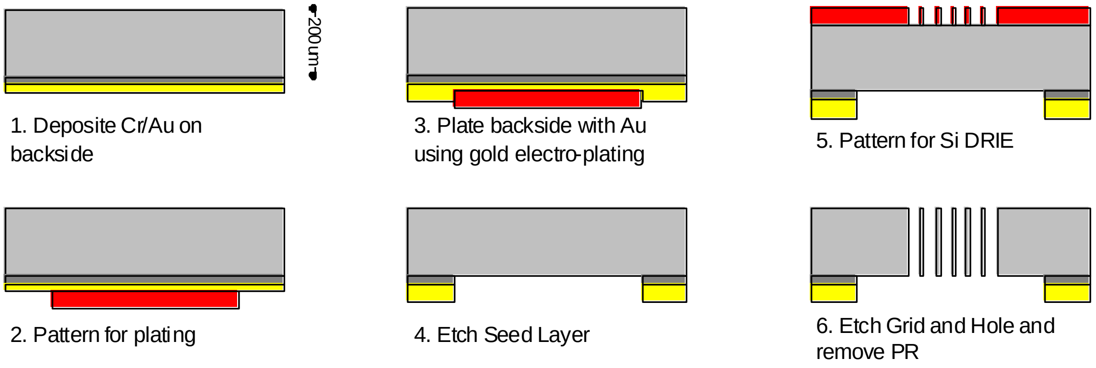

1. Deposite Cr/Au on backside

2. Pattern for plating

3. Plate backside with Au using gold electro-plating

4. Etch Seed Layer

5. Pattern for Si DRIE

6. Etch Grid and Hole and remove PR

Figure I. Fabrication steps for the Top Layer of the Microfabricated Passive Preconcentrator/Injector

1.1. Prefurnace Clean (Prefurnace Clean Bench)

100 Si wafer, thickness 200 ± 10 μm

Organic Clean (H_2O : NH_4OH : H_2O_2 = 2 : 1 : 1): 90 ˚C, 10 min

DI Water Rinse: 2 min

HF (100 : 1) Dip: 30 sec

DI Water Rinse: 2 min

Ionic Clean (H_2O : HCl : H_2O_2 = 2 : 1 : 1): 90 ˚C, 10 min

DI Water Rinse: 15 min

Spin Rinse and Dry: until resistivity reaches 15.1 Ω/cm^2

1.2. Cr/Au deposition (Enerjet Evaporator)

Thickness: 20/500 nm

2.1. Photoresist Patterning for Au Electroplating

HMDS: 4000 rpm, 10 s

Photoresist: PR 1827, ~ 2.7 μm

Spin: 500 rpm, 8 s + 4000 rpm, 30 s

Soft Bake on Hotplate: 110 ˚C, 1 min 10 s

Cool Down in Ambient: ~ 5 min

Exposure (MA6 Mask Aligner): 17 sec

Development (MF 319): 1 min 30 s

DI Water Rinse: 3 min

Descum in March Asher: O_2, 80 W, 250 mT, 1 min

3.1. Au Electro Plating

Gold plating bath: 50 ˚C, 200 rpm

Plating current: 2 mA/cm^2

Volt limit: 2 V

Negative electrode: attached to the sample

Positive electrode: attached to the platinum electrode

Plating: 4 h, 4 μm

DI Water Rinse: 5 min

3.2. Photoresist Removal (Organic Wet Bench)

PRS-2000 Soak: > 10 min

DI Water Rinse: 5 min

Spin Rinse Dry

3.3. Photoresist Patterning for Seed Layer Removal

HMDS: 4000 rpm, 10 s

Photoresist: PR 1827, ~ 2.7 μm

Spin: 500 rpm, 8 s + 4000 rpm, 30 s

Soft Bake on Hotplate: 110 ˚C, 1 min 10 s

Cool Down in Ambient: ~ 5 min

Exposure (MA6 Mask Aligner): 17 sec
Development (MF 319): 1 min 30 s
DI Water Rinse: 3 min
Descum in March Asher: O_2, 80 W, 250 mT, 1 min

4.1. Au Seed Layer Removal

Soak in Gold Etchant: ~ 3 min
DI Water Rinse: 3 min

4.2. Cr Seed Layer Removal

Dip in Cr Etchant: ~ 20 s
DI Water Rinse: 3 min

4.3. Photoresist Removal (Organic Wet Bench)

PRS-2000 Soak: > 10 min
DI Water Rinse: 5 min
Spin Rinse Dry

5.1. Photoresist Patterning for Diffusion Channel Etching

Photoresist: AZ 9260, ~8 μm
Spin on Frontside: 500 rpm, 4 s + 3000 rpm, 30 s
Soft Bake on Hotplate: 110 ˚C, 3 min 30 s
Cool Down in Ambient: > 5 min
Exposure (MA6 Mask Aligner): 28 sec
Development (AZ 400 : DI = 1 : 3): ~ 4 min
DI Water Rinse: 3 min

6.1. Frontside DRIE - Diffusion Channels

DRIE in STS ICP Machine: Recipe TYC-HR2
Target depth: 200 μm, Etching time: ~ 90 min

6.2. Photoresist Removal

PRS-2000 Soak: > 10 min

DI Water Rinse: 5 min

Spin Rinse Dry

Appendix II

Bottom Layer Fabrication

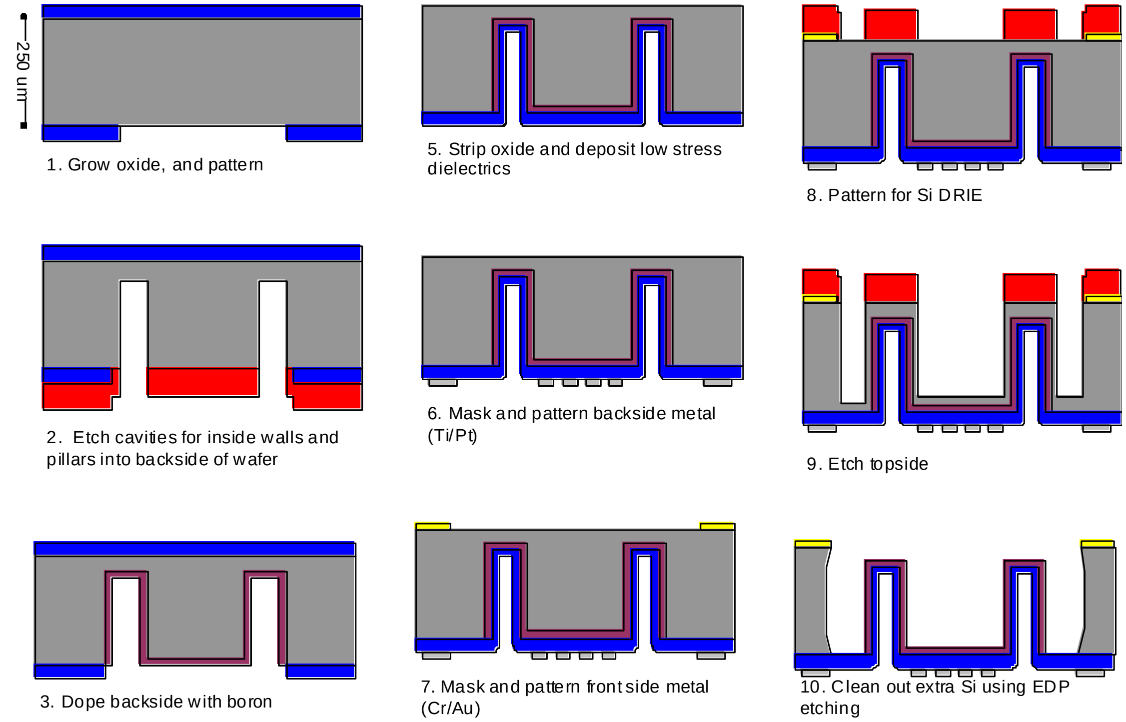

1. Grow oxide, and pattern

2. Etch cavities for inside walls and pillars into backside of wafer

3. Dope backside with boron

5. Strip oxide and deposit low stress dielectrics

6. Mask and pattern backside metal (Ti/Pt)

7. Mask and pattern front side metal (Cr/Au)

8. Pattern for Si DRIE

9. Etch topside

10. Clean out extra Si using EDP etching

Figure II. Fabrication steps for the Bottom Layer of the Microfabricated Passive Preconcentrator/Injector

1.1. Prefurnace Clean (Prefurnace Clean Bench)

100 Si wafer, thickness 250 ± 10 μm

Organic Clean (H_2O : NH_4OH : H_2O_2 = 2 : 1 : 1): 90 ˚C, 10 min

DI Water Rinse: 2 min

HF (100 : 1) Dip: 30 sec

DI Water Rinse: 2 min

Ionic Clean (H_2O : HCl : H_2O_2 = 2 : 1 : 1): 90 ˚C, 10 min

DI Water Rinse: 15 min

Spin Rinse and Dry: until resistivity reaches $15.1\ \Omega/cm^2$

1.2. Thermal Oxidation - Boron Diffusion Barrier (A4 Furnace)

Recipe: DWDA1

Parameter Table: OXIDIZE

Temperature: 1100 ˚C

Dry: 5 min, Wet: 3 hour 20 min, Dry: 10 min, N_2Aneal: 5 min

Thickness: 1 μm

1.3. Photoresist Patterning- Oxide Etching

HMDS: 4000 rpm, 10 s

Photoresist: PR 1827, ~ 2.7 μm

Spin: 500 rpm, 8 s + 4000 rpm, 30 s

Soft Bake on Hotplate: 110 ˚C, 1 min 10 s

Cool Down in Ambient: ~ 5 min

Exposure (MA6 Mask Aligner): 17 sec

Development (MF 319): 1 min 30 s

DI Water Rinse: 3 min

Descum in March Asher: O_2, 80 W, 250 mT, 1 min

1.4. Oxide Patterning (Acid Wet Bench)

BHF Dip: ~ 10 min

1.5. Photoresist Removal (Organic Wet Bench)

PRS-2000 Soak: > 10 min

DI Water Rinse: 5 min

Spin Rinse Dry

2.1. Photoresist Patterning for Thermal Isolation Pillars

Photoresist: AZ 9260, ~8 μm

Spin on Frontside: 500 rpm, 4 s + 3000 rpm, 30 s

Soft Bake on Hotplate: 110 ˚C, 3 min 30 s

Cool Down in Ambient: > 5 min

Exposure (MA6 Mask Aligner): 28 sec

Development (AZ 400 : DI = 1 : 3): ~ 4 min

DI Water Rinse: 3 min

2.2. Backside DRIE - Thermal Isolation Pillars

DRIE in STS ICP Machine: Recipe TYC-HR2

Target depth: 200 μm, Etching time: ~ 90 min

2.3. Photoresist Removal (Organic Wet Bench)

PRS-2000 Soak: > 10 min

DI Water Rinse: 5 min

Spin Rinse Dry

3.1. Prefurnace Clean (Prefurnace Clean Bench)

Organic Clean (H_2O : NH_4OH : H_2O_2 = 2 : 1 : 1): 90 ˚C, 10 min

DI Water Rinse: 2 min

HF (100 : 1) Dip: 30 sec

DI Water Rinse: 2 min

Ionic Clean (H_2O : HCl : H_2O_2 = 2 : 1 : 1): 90 ˚C, 10 min

DI Water Rinse: 15 min

Spin Rinse and Dry: until resistivity reaches 15.1 Ω/cm^2

3.2. Deep Boron Doping (A2 Furnace)

Recipe: BDEP99

Parameter Table: BORON99

Dep Time: 8 hour, Dilution Time: 10 min, Temperature: 1175 ˚C

3.3. Boron Drive-in (A4 Furnace)

Recipe: N2ANL/OX

Parameter Table: N2ANL/OX

Set Time: 10 min, ANL Time: 8 hour, Temperature: 1175 ˚C

Dry: 5 min, Wet: 20 min, Dry: 5 min, N_2Aneal: 5 min, Temperature: 1000 ˚C

5.1. Oxide Removal (Acid Wet Bench)

BHF Dip: ~ 10 min

5.2. Oxynitride Deposition for Membrane Heater (GSI PECVD)

Recipe: Oxynitride 400

Thickness: 15 μm

6.1. Photoresist Patterning for Frontside Protection and Backside Ti/Pt Heater Lift-off

HMDS: 4000 rpm, 10 s

Photoresist: PR 1827, ~ 2.7 μm

Spin: 500 rpm, 8 s + 4000 rpm, 30 s

Soft Bake on Hotplate: 110 ˚C, 1 min 10 s

Cool Down in Ambient: ~ 5 min

Exposure (MA6 Mask Aligner): 17 sec

Development (MF 319): 1 min 30 s

DI Water Rinse: 3 min

Descum in March Asher: O_2, 80 W, 250 mT, 1 min

6.2. Ti/Pt Deposition (Enerjet Evaporator)

Thickness: 10/100 nm

6.3. Ti/Pt Lift-off

Soak in Acetone for 10 min

DI Water Rinse: 3 min

7.1. Photoresist Patterning - Cr/Au Patterning on Frontside

HMDS: 4000 rpm, 10 s

Photoresist: PR 1827, ~ 2.7 μm

Spin: 500 rpm, 8 s + 4000 rpm, 30 s

Soft Bake on Hotplate: 110 ˚C, 1 min 10 s
Cool Down in Ambient: ~ 5 min
Exposure (MA6 Mask Aligner): 17 sec
Development (MF 319): 1 min 30 s
DI Water Rinse: 3 min
Descum in March Asher: O_2, 80 W, 250 mT, 1 min

7.2. Cr/Au deposition (Enerjet Evaporator)
Thickness: 20/500 nm

7.3. Photoresist Removal
PRS-2000 Soak: > 10 min
DI Water Rinse: 5 min
Spin Rinse Dry

8.1. Photoresist Patterning for Cavity to retain C-Xs
Photoresist: AZ 9260, ~8 μm
Spin on Frontside: 500 rpm, 4 s + 3000 rpm, 30 s
Soft Bake on Hotplate: 110 ˚C, 3 min 30 s
Cool Down in Ambient: > 5 min
Exposure (MA6 Mask Aligner): 28 sec
Development (AZ 400 : DI = 1 : 3): ~ 4 min
DI Water Rinse: 3 min

9.1. Frontside DRIE - Cavity to retain C-Xs
DRIE in STS ICP Machine: Recipe TYC-HR2
Target depth: 200 μm, Etching time: ~ 60 min

10.1. EDP Wet Etching
DI Water : Catechol : Pyrazine : Ethylenediamene = 432 mL : 432 g : 8.1 g : 1.35 L
Temperature: 110 ˚C, Time: ~ 100 min

DI Water Rinse: 10 min @ 80 ˚C

10.2 Wafer Dicing

Dicing with MA 1006 dicing Saw: Blade 42525

BIBLIIOGRAPHY

[1] A. T. Hodgson, H. Levin, "Volatile Organic Compounds in Indoor Air: A Review of Concentrations Measured in North America Since 1990," Lawrence Berkeley National Laboratory, pp. 31, 2003.

[2] "Carcinogenic Effects of Benzene: An Update," EPA/600/P-97/001F, April 1998.

[3] A. B. Littlewood, "Gas Chromatography: Principles, Techniques, and Applications," New York: Academic, 1970.

[4] A. Van Es, "High-Speed Narrow Bore Capillary Gas Chromatography," Heidelberg, Germany: Huthig Buch Verlag, 1992.

[5] D. L. DeVoe, "Thermal issues, in MEMS and microscale systems," *IEEE Tranctions on Components and Packaging Technologies*, vol. 25, pp. 576-584, 2003.

[6] B. Kolb, "Headspace sampling with capillary columns," *Journal of Chromatography A*, vol. 842, pp. 163-205, 1999.

[7] M. Harper, "Sorbent trapping of volatile organic compounds from air," *Journal of Chromatography A*, vol. 885, pp. 129-151, 2000.

[8] H. Kim, W. H. Steinecker, S. M. Reidy, G. R. Lambertus, A. Astle, K. Najafi, E. T. Zellers, L. P. Bernal, P. Washabaugh, and K. D. wise, "A Micropump-driven high-speed MEMS gas chromatography system," *IEEE International Conference on Solid-State Sensors and Actuators (Transducers)*, Lyon, France, pp. 1505-1508, June 2007.

[9] J. Liu, N. K. Gupta, X. Fan, K. D. Wise, and Y. B. Gianchandani, "A pressure programmable gas chromatography microsystem utilizing motionless Knudsen pump, fiber-integrated optical detector, and silicon micromachined separation column," *IEEE International Conference on Solid-State Sensors and Actuators (Transducers)*, Beijing, China, pp. 803-806, June 2011.

[10] C.-J. Lu, W. H. Steinecker, W.-C. Tian, M. C. Oborny, J. M. Nichols, M. Agar, J. A. Potkay, H. K. L. Chan, J. Driscoll, R. D. Sacks, K. F. Wise, S. W. Pang, and E. T. Zellers, "First-generation hybrid MEMS gas chromatograph," *Lab on a Chip*, vol. 5, pp. 1123-1131, 2005.

[11] S. Zampolli, I. Elmi, F. Mancarella, P. Betti, E. Dalcanale, G. C. Cardinali, M. Sveri, "Real-time monitoring of sub-ppb concentrations of aromatic volatiles with a MEMS-enabled miniaturized gas-chromatograph," *Sensors and Actuators B,* vol. 141, pp. 322-328, 2009.

[12] P. R. Lewis, R. P. Manginell, D. R. Adkins, R. J. Kottenstette, D. R. Wheeler, S. S. Sokolowski, D. E. Trudell, J. E. Byrnes, M. Okandan, J. M. Bauer, R. G. manley and G. C. Frye-Mason, "Recent Advancements in the gas-phase MicroChemlab," *IEEE Sensors Journal*, vol. 6, pp. 784-795, 2006.

[13] E. T. Zellers, G. Serrano, H. Chang, and L. K. Amos, "A micro gas chromatograph for rapid determinations of explosive marker compounds," *IEEE International Conference on Solid-State Sensors and Actuators (Transducers)*, Beijing, China, pp. 2082-2085, 2011.

[14] S. K. Kim, H. Chang, and E. T. Zellers, "Microfabricated gas chromatograph for the selective determination of trichloroethlyene vapor at sub-parts-per-billion concentrations in complex mixtures," *Analytical Chemistry*, vol. 83, pp. 7198-7206, 2011.

[15] http://www.schwarzer.com/pdf/SP_PUMPS_DataSheet_ClassFZ_Type135FZ.pdf .

[16] http://www.knf.com/pdfs/nmp05_09_015.pdf .

[17] http://divapps.parker.com/divapps/pnd/downloads/upd/CTS%20pump%20data%20sheet .pdf .

[18] I. Gràcia, P. Ivanov, F. Blanco, N. Sabaté, X. Vilanova, X. Correig, L. Fonseca, E. Figueras, J. Santander, and C. Cané, "Sub-ppm gas sensor detection via spiral μ-preconcentrator," *Sensors and Actuators B*, vol. 132, pp. 149-154, 2008.

[19] W.-C. Tian, S. W. pang, C-J. Lu, and E. T. Zellers, "Microfabricated preconcentrator-focuser for a microscale gas chromatograph," *Journal of Microelectromechanical Systems*, vol. 12, pp. 264-272, 2003.

[20] W.-C. Tian, H. K. L. Chan, C-J. Lu, S. W. Pang and E. T. Zellers, "Multiple-stage microfabricated preconcentrator-focuser for micro gas chromatography system," *Journal of Microelectromechanical Systems*, vol. 14, pp. 498-507, 2005.

[21] A. M. Ruiz, I. Gràcia, N. Sabaté , P. Ivanov, A. Sánchez, M. Duch, M. Gerbolés, A. Moreno, and C. Cané, "Membrane-suspended microgrid as a gas preconcentrator for chromatographic applications," *Sensors and Actuators A*, vol. 135, pp. 192-196, 2007.

[22] P. Ivanov, F. Blanco, I. Gràcia, N. Sabaté, A. M. Ruiz, X. Vilanova, X. Correig, L. Fonseca, E. Figueras, J. Santander, and C. Cané, "Improvement of the gas sensor response via silicon μ-preconcentrator," *Sensors and Actuators B*, vol. 127, pp. 288-294, 2007.

[23] W.-C. Tian and S. W. pang, "Thick and thermally isolated Si microheaters for microfabricated preconcentrators," *Journal of Vacuum Science and Technology B*, vol. 21, pp. 274-279, 2003.

[24] I. Gràcia, P. Ivanov, F. Blanco, N. Sabaté, X. Vilanova, X. Correig, L. Fonseca, E. Figueras, J. Santander, and C. Cané, "Influence of the internal gas flow distribution on the efficiency of a μ-preconcentrator," vol. 135, pp. 52-56, 2008.

[25] M. Kim and S. Mitra, "A microfabricated microconcentrator for sensors and gas chromatography," *Journal of Chromatography A*, vol. 996, pp. 1-11, 2003.

[26] C. Pijolat, M. Camara, J. Courbat, J.-P. Viricelle, D. Briand, and N. F. de Rooij, "Application of carbon nano-powders for a gas micro-preconcentrator," *Sensors and Actuators B*, vol. 127, pp. 179-185, 2007.

[27] J. Yeom, C. R. field, B. Bae, R. I. Masel, and M. A. Shannon, "The design, fabrication and characterization of a silicon microheater for an integrated MEMS gas preconcentrator," *Journal of Micromechanics and Microengineering*, vol. 18, 125001, 2008.

[28] R. P. Manginell, d. R. Adkins, M. W. Moorman, R. Hadizadeh, D. Copic, D. A. Porter, J. M. Anderson, V. M. Hietala, J. R. Bryan, D. R. Wheeler, K. B. Pfeifer, and Arthur Rumpf, "Mass-sensitive microfabricated chemical preconcentrator," *Journal of Microelectromechanical Systems*, vol. 17. pp. 1396-1407, 2008.

[29] B. Alfeeli, L. T. Taylor, and M. Agah, "Evaluation of Tenax TA thin films as adsorbent materials for micro preconcentration applications," *Microchemical Journal*, vol. 95, pp. 259-267, 2010.

[30] B. Alfeeli, D. Cho, M. Ashraf-Khorassani, L. T. Taylor, and M. Agah, "MEMS-based multi-inlet/outlet preconcentrator coated by inkjet printing of polymer adsorbents," *Sensors and Actuators B*, vol. 133, pp.24-32, 2008.

[31] E. H. M. Camara, P. Reuil, D. Briand, L. Guillot, C. Pijolat, N. F. de Rooij, "Micro gas preconcentrator in porous silicon filled with a carbon absorbent," *Sensors and Actuators B*, vol. 148, pp. 610-619, 2010.

[32] M. D. Martin, T. J. Roussel, S. Cambron, J. Aebersold, D. Jackson, K. Walsh, J.-T. Lin, M. G. O'Toole, and R. Keynton, "Performance of stacked, flow-through micropreconcentrators for portable trace detection," *International Journal for Ion Mobility Spectrometry*, vol. 13, pp. 109-119, 2010.

[33] E. H. M. Camara, P. Reuil, D. Briand, C. Pijolat, N. F. de Rooij, "A micro gas preconcentrator with improved performance for pollution monitoring and explosives detection," *Analytica Chimica Acta*, vol. 688, pp. 175-182, 2011.

[34] B. Alfeeli, V. Jain, R. K. Johnson, F. L. Beyer, J. R. Heflin, M. Agah, "Chrcterization of poly (2,6-diphenyl-*p*-phenylene oxide) films as adsorbent for microfabricated preconcentrators," *Microchemical Journal*, vol. 98, pp. 240-245, 2011.

[35] H. Lahlou, J.-B. Sanchez, Y. Mohsen, X. Vilanova, F. Berger, E. Llobet, X. Correig, V. fierro, A. Celzard, I. Gràcia, and C. Cané, "A planar micro-concentrator/injector for low power consumption microchromatographic analysis of benzene and 1,3 butadiene," *Microsystem Technologies*, vol. 18, pp. 489-495, 2012.

[36] H.-S. Noh, P. J. hesketh, and G. C. Frye-Mason, "Parylene gas chromatographic column for rapid thermal cycling," *Journal of Microelectromechanical Systems*, vol. 11, pp. 718-725, 2002.

[37] J. A. Dziuban, J. Mróz, M. Szczygielska, M. Małachowski, A. Górecka-Drzazga, R. Walczak, W. Buła, D. Zalewski, Ł. Nieradko, J. Łysko, J. Koszur, P. Kowalski, "Portable gas chromatograph with integrated components," *Sensors and Actuators A*, vol. 115, pp. 318-330, 2004.

[38] G. Lambertus, A. Elstro, K. Sensenig, J. Potkay, M. Agah, S. Scheuering, K. Wise, F. Dorman, and R. Sacks, "Design, fabrication, and evaluation of microfabricated columns for gas chromatography," *Analytical Chemistry*, vol. 76, pp. 2629-2637, 2004.

[39] M. Agah, J. A. Potkay, G. Lambertus, R. Sacks, and K. D. Wise, "High-performance temperature-programmed microfabricated gas chromatography columns," *Journal of Microelectromechanical Systems*, vol. 14, pp. 1039-1050, 2005.

[40] A. Bhushan, D. Yemane, D. Trudell, E. B. Overton, and J. Goettert, "Fabrication of micro-gas chromatograph columns for fast chromatography," *Microsystem Technologies*, vol. 13, pp. 361-368, 2007.

[41] S. Reidy, G. Lambertus, J. Reece, and R. Sacks, "High-performance, static-coated silicon microfabricated columns for gas chromatography," *Analytical Chemistry*, vol. 78, pp. 2623-2630, 2006.

[42] A. D. Radadia, R. I. Masel, M. A. Shannon, J. P. Jerrell, and K. R. Cadwallader, "Micromachined GC columns for fast separation of organophosphonate and organosulfur compounds," *Analytical Chemistry*, vol. 80, pp. 4087-4094, 2008.

[43] S. Reidy, D. George, M. Agah, and R. Sacks, "Temperature-programmed GC using silicon microfabricated columns with integrated heaters and temperature sensors," *Analytical Chemistry*, vol. 79, pp. 2911-2917, 2007.

[44] S. Ali, M. Ashraf-Khorassani, L. T. Taylor, and M. Agah, "MEMS-based semi-packed gas chromatography columns," *Sensors and Actuators B*, vol. 141, pp. 309-315, 2009.

[45] G. Serrano, S. M. Reidy, and E. T. Zellers, "Assessing the reliability of wall-coated microfabricated gas chromatographic separation columns," *Sensors and Actuators B*, vol. 141, pp. 217-226, 2009.

[46] Q.-Y. Cai and E. T. Zellers, "Dual-chemiresistor GC detector employing monolayer-protected metal nanocluster interfaces," *Analytical Chemistry*, vol. 74, pp. 3533-3539, 2002.

[47] C.-J. Lu, J. Whiting, R. D. Sacks, and E. T. Zellers, "Portable gas chromatograph with tunable retention and sensor array detection for determination of complex vapor mixtures," *Analytical Chemistry*, vol. 75, pp. 1400-1409, 2003.

[48] M.-D. Hsieh and E. T. Zellers, "Limits of recognition for simple vapor mixtures determined with a microsensor array," *Analytical Chemistry*, vol. 76, pp. 1885-1895, 2004.

[49] R. Archibald, P. Datskos, G. Devault, V. Lamberti, N. Lavrik, D. Noid, M. Sepaniak, and P. Dutta, "Independent component analysis of nanomechanical

responses of cantilever arrays," *Analytica Chimica Acta*, vol. 584, pp. 101-105, 2007.

[50] S. Wu, A. Deev, M. Haught, and Y. Tang, "Hollow waveguide quantum cascade laser spectrometer as an online microliter sensor for gas chromatography," *Journal of Chromatography A*, vol. 1188, pp. 327-330, 2008.

[51] C. Jin, P. Kurzawski, A. Hierlemann, and E. T. Zellers, "Evaluation of multitransducer arrays for the determination of organic vapor mixtures," *Analytical Chemistry*, vol. 80, 227-236, 2008.

[52] D. J. Rairigh, G. A. Warnell, C. Xu, E. T. Zellers, and A. J. Mason, "CMOS baseline tracking and cancellation instrumentation for nanoparticle-coated chemiresistors," *IEEE Transactions on Biomedical Circuits and Systems*, vol. 3 , pp. 267-276, 2009.

[53] Y. Sun, J. Liu, D. J. Howard, G. Frye-Mason, A. K. Thompson, S. Ja, and X. Fan, "Rapid tandem-column micro-gas chromatography based on optofluidic ring resonators with multi-point on-column detection," *Analyist*, vol. 135, pp. 165-171, 2010.

[54] E. Covington, F. I. Bohrer, C. Xu, E. T. Zellers, and C. Kurdak, "Densely integrated array of chemiresistor vapor sensors with electron-beam patterned monolayer-protected gold nanoparticle interface films," *Lab on a Chip*, vol. 10, pp. 3058-3060, 2010.

[55] J. Liu, Y. Sun, d. J. Howard, G. Frye-Mason, A. K. Thompson, S. Ja, S.-K Wang, M. Bai, H. Taub, M. Almasri, and X. Fan, "Fabry-Pérot cavity sensors for multipoint on-column micro gas chromatography detection," *Anlaytical Chemistry*, vol. 82, pp. 4370-4375, 2010.

[56] M. Li, E. B. Myers, H. X. Tang, S. J. Aldridge, H. C. McCaig, J. J. Whiting, R. J. Simonson, N. S. Lewis, and M. L. Roukes, "Nanoelectromechnical resonator array for ultrafast, gas-phase chromatographic chemical analysis," *Nano Letters*, vol. 10, pp. 3988-3903, 2010.

[57] X. Fan and I. M. white, "Optofluidic microsystems for chemical and biological analysis," *Nature Photonics*, vol. 5, pp. 591-597, 2011.

[58] K. Reddy, Y. Guo, J. Liu, W. Lee, M. K. K. Oo, and X. Fan, "Rapid, sensitive, and multiplexed on-chip optical sensors for micro-gas chromatography," *Lab on a Chip*, vol. 12, pp. 901-905, 2012.

[59] R. P. Manginell, J. M. Bauer, M. W. Moorman, L. J. Sanchez, J. M. Anderson, J. J. Whiting, D. A. Porter, D. Copic, and K. E. Achyuthan, "A monolithically-integrated μGC chemical sensor system," *Sensors*, vol. 11, pp. 6517-6532, 2011.

[60] G. R. lambertus, C. S. Fix, S. M. Reidy, R. A. Miller, D. Wheeler, E. Nazarov, and R. Sacks, "Silicon microfabricated column with microfabricated differential mobility spectrometer for GC analysis of volatile organic compounds," *Anlaytical Chemistry*, vol. 77, pp. 7563-7571, 2005.

[61] S. K. Kim, H. Chang, and E. T. Zellers, "Prototype micro gas chromatograph for breath biomarkers of respiratory disease," *IEEE International Conference on Solid-State Sensors and Actuators (Transducers)*, Denver, CO, pp. 128-131, June 2009.

[62] G. Serrano, H. Chang, and E. T. Zellers, "A micro gas chromatograph for high-speed determinations of explosive vapors," *IEEE International Conference on Solid-State Sensors and Actuators (Transducers)*, Denver, CO, pp. 1654-1657, June 2009.

[63] H. Chang, S. K. Kim, T. Sukaew, F. Bohrer, and E. T. Zellers, "Microfabricated gas chromatograph for sub-ppb determination of TCE in vapor instrusion investigation," *Procedia Engineering*, vol. 5, pp. 973-976, 2010.

[64] S. C. Terry, J. H. Jerman, and J. B. Angell, "A gas chromatographica air analyzer fabricated on a silicon wafer," *IEEE Transactions on Electron Devices*, vol. 26, pp. 1880-1886, 1979.

[65] R. R. Reston and E. S. Kolesar, "Silicon-micromachined gas chromatography system used to separate and detect ammonia and nitrogen dioxide-Part I: design, fabrication, and integration of the gas chromatography system," *Journal of Microelectromechanical Systems*, vol. 3, pp. 134-146, 1994.

[66] E. S. Kolesar and R. R. Reston, "Silicon-micromachined gas chromatography system used to separate and detect ammonia and nitrogen dioxide-Part II: evaluation, analysis, and theoretical modeling of the gas chromatography system," *Journal of Microelectromechanical Systems*, vol. 3, pp. 147-154, 1994.

[67] E. S. Kolesar and R. R. Reston, "Review and summary of a silicon micromachined gas chromatography system," *IEEE Transactions on Components packaging and Manufacturing Technology Part B*, vol. 21, pp. 324-328, 1998.

[68] W. A. Groves, E. T. Zellers, and G. C. Frye, "Analyzing organic vapors in exhaled breath using a surface acoustic wave sensor array with preconcentration: Selection

and chracterization of the preconcentraotr adsorbent," *Analytica Chimica Acta,* vol. 371, pp. 131-143, 1998.

[69] J. W. Grate, N. C. Anheier, and D. L. Baldwin, "Progressive thermal desorption of vapor mixtures from a preconcentrator with a porous metal foam internal architecture and variable thermal ramp rates," *Analytical Chemistry,* vol. 77, pp. 1867-1875, 2005.

[70] C.-J. Lu and E. T. Zellers, "A dual-adsorbent preconcentrator for a portable indoor-VOC microsensor system," *Analytical Chemistry*, vol. 73, pp. 3449-3457, 2001.

[71] G. C. Frye-Mason, r. J. Kottenstette, P. R. Lewis, E. Heller, R. P. Manginell, D. R. Adkins, G. Dulleck, D. Martinez, D. Sasaki, C. Mowry, C. Matzke, L. Anderson, "Hand-held miniature chemical analysis system (μChemlab) for detection of trace concentrations of gas phase analytes," *Proceedings of the μTAS 2000 symposium*, Workshop, Enschede, The Netherlands, 2000.

[72] R. P. Manginell, G. C. Frye-Mason, R. J. Kottenstette, P. R. Lewis, C. C. Wong, "Microfabricated planar preconcentrator," *Technical Digest of the 2000 Solid-State Sensor and Actuator Workshop*, Cleveland, OH, USA, pp. 179-182, 2000.

[73] I. Voiculescu, M. Zaghloul, N. Narasimhan, "Microfabricated chemical preconcentrators for gas-phase microanalytical detection systems," *Trends in Analytical Chemistry*, vol. 27, pp. 327-343, 2008.

[74] M. Martin, M. Crain, K. Walsh, R. A. McGill, E. Houser, J. Stepnowski, S. Stepnowski, H.-D, Wu, and S. Ross, "Microfabricated vapor preconcentrator for portable ion mobility spectroscopy," *Sensors and Actuators B*, vol. 126, pp. 447-454, 2007.

[75] I. Voiculescu, R. A. McGill, M. E. Zaghloul, D. Mott, J. Stepnowski, S. Stepnowski, H. Summers, V. Nguyen, S. Ross, K. Walsh, and M. Martin, "Micropreconcentrator for enhanced trace detection of explosives and chemical agents," *IEEE Sensors Journal*, vol. 6, pp. 1094-1104, 2006.

[76] R. A. Veeneman, "Design and characterization of a multi-vapor preconcentrator for a micro-scale gas chromatograph," PhD thesis, The University of Michigan, 2009.

[77] E. T. Zellers, S. Reidy, R. A. Veeneman, R. Gordenker, W. H. Steinecker, G. R. Lambertus, H. Kim, J. A. Potkay, M. P. Rowe, Z. Qiongyan, C. Avery, H. K. L. Sacks, K. Najafi, and K. D. Wise, "An integrated micro-analytical system for

complex vapor mixtures," *in Technical Digest Transducers'07*, Lyon, France, pp. 1491-1496, June 2007.

[78] E. D. Palmes and A. F. Gunnison, "Personal monitoring device for gaseous contaminants," *Americal Industrial Hygiene Association Journal*, vol. 34, pp. 78-81, 1973.

[79] J. Namiesnik, B. Zabiegala, A. Kot-Wasik, M. Partyka and A. Wasik, "Passive sampling and/or extraction techniques in environmental analysis: a review," *Analytical and Bioanalytical Chemistry*, vol. 381, pp. 279-301, 2005.

[80] M. J. Boss, D. W. Day, *Air sampling and industrial hygiene engineering*, CRC Press, Boca Raton, FL, 2000.

[81] B. A. Plog, P. J. Quinlan, *Fundamentals of industrial hygiene*, NSC Press, 5th. ed., Itasca, IL, 2002.

[82] *http://www.skcinc.com/instructions/1667.pdf*

[83] C-W. Chung, M. T. Morandi, T. H. Stock, and M. Afshar, "Evaluation of a passive sampler for volatile organic compounds at ppb concentrations, varying temperatures, and humidities with 24-h exposures. 2. sampler performance," *Environmental Science and Technology*, vol. 33, pp. 3666-3671, 1999.

[84] J. Gonzalez and S. P. Levine, "The development and evaluation of a thermally-desorbable miniature passive dosimeter for the monitoring of organic vapors," *Americal Industrial Hygiene Association Journal*, vol. 47, pp. 339-346, 1986.

[85] J. Gonzalez and S. P. Levine, "Vapor phase spiking and thermal desorption of a passive sampler," *Americal Industrial Hygiene Association Journal*, vol. 48, pp. 739-744, 1987.

[86] G. O. Nelson, *Gas mixtures: preparation and control*, CRC Press, Boca Raton, FL, 1992.

[87] A. Wheeler and A. J. Robell, "Performance of fixed-bed catalytic reactor with poison in the feed," *Journal of Catalysis*, vol. 13, pp. 299-305, 1969.

[88] E. V. Kring and W. J. Lautenberger, "Dosimeter for measuring gaseous contaminants," *Du-pont U.S.Patent 4,235,097*, Nov. 25. 1980.

[89] C. J. Lu and E. T. Zellers, "Multi-adsorbent preconcentration/focusing module for portable-GC/microsensor-array analysis of complex vapor mixtures," *Analyst*, vol. 127, pp. 1061-1068, 2002.

[90] *http://www.sigmaaldrich.com/analytical-chromatography/air-monitoring/learning-center/adsorbent-selection.html*

[90] F. M. White, *Fluid mechanics*, McGraw-Hill, New York, NY, 10th ed., 2010.

[91] American Conference of Governmental Industrial Hygienists, *Threshold Limit Values for Chemical Substances and Physical Agents and Biological Exposure Indices,* ACGIH, Cincinnati, OH, USA, 2011.

[92] C.-Y. Peng and S. Batterman, "Performance evaluation of a sorbent tube sampling method using short path thermal desorption for volatile organic compounds," *Journal of Environmental Monitoring*, vol. 2, pp. 313-324, 2000.

[93] S. Ross, *Statistics for engineers and scientists*, Elsevier Academic Press, 4th ed., Waltham, MA, 2009.

[94] J. H. Seo, S. K. Kim, E. T. Zellers, and K. Kurabayashi, "Microfabricated passive vapor preconcentrator/injector designed for microscale gas chromatography," *Lab on a Chip*, vol. 12, pp. 717-724, 2012.

[95] J. C. Giddings, "Kinetic origin of tailing in chromatography ," *Analytical Chemistry*, vol. 35, pp. 1999-2002, 1963.

[96] E. W. Cieplinski, "Prevention of peak tailing in the direct gas chromatographic analysis of barbiturates," *Analytical Chemistry*, vol. 35, pp. 256-257, 1963.

[97] E. Grushka, M. N. Myers, P. D. Schettler, J. C. Giddings, "Computer characterization of chromatographic peaks by plate height and higher central moments," *Analytical Chemistry*, vol. 41, pp. 889-892, 1969.

[98] A. Sokolowski and K.-G. Wahlund, "Peak tailing and retention behaviour of tricyclic antidepressant amines and related hydrophobic ammonium compounds in reversed-phase ion-pair liquid chromatography on alkyl-bonded phases," *Journal of Chromatography A*, vol. 189, pp. 299-316, 1980.

[99] T. Fornstedt, G. A. Guiochon, "Comparison between experimental and theoretical profiles of high concentration elution bands and large system peaks in nopnlinear chromatography," *Analytical Chemistry*, vol. 66, pp. 2686-2693, 1994.

[100] B. Lin, T. Yun, G. Zhong, and G. Guiochon, "Shock layer analysis for a single-component in preparative elution chromatography," *Journal of Chromatography A*, vol. 708, pp. 1-12, 1995.

[101] T. Fornstedt, G. Zhong, and G. Guiochon, "Peak tailing and mass transfer kinetics in linear chromatography," *Journal of Chromatography A*, vol. 741, pp. 1-12, 1996.

[102] G. Gotmar, T. Fornstedt, and G. Guiochon, "peak tailing and mass transfer kinetics in linear chromatography: Dependence on the column length and the linear velocity of the mobile phase," *Journal of Chromatography A*, vol. 831, pp. 17-35, 1999.

[103] F. Stoeckli, M. V. López-Ramón, and C. Moreno-Castilla, "Adsorption of phenolic compounds from aqueous solutions, by activated carbons, described by the Dubinin-Astakhov Equation," *Langmuir*, vol. 17, pp. 3301-3306, 2001.

[104] P. A. M. Mourão, P. J. M. Carrott, M. M. L. R. Carrott, "Application of different equations to adsorption isotherms of phenolic compounds on activated carbons prepared from cork," *Carbon*, vol. 44, pp. 2422-2429, 2006.

[105] D. Hugi-Cleary and F. Stoeckli, "On the use of standard DRK isotherms in Dubinin's *t/F* method," vol. 38, pp. 1309-1313, 2000.

[106] J. Liu, Y. Sun, and X. Fan, "Highly versatile fiber-based optical Fabry-Pérot gas sensor," *Optics Express*, vol. 17, pp. 2731-2738, 2009.

[107] J. Liu, N. K. Gupta, K. D. Wise, Y. B. Gianchandani, and X. Fan, "Demonstration of motionless Knudsen pump based micro-gas chromatography featuring micro-fabricated columns and on-column detectors," *Lab on a Chip*, vol. 11, pp. 3487-3492, 2011.

[108] W. M. Kays, M. E. Crawford, *Convection Heat and Mass Transfer*, McGraw-Hill, New York

[109] E. B. wilson, J. C. Decious, P. Cross, *Molecular Vibrations*, Dover, New York, 1980.

[110] K. E. Noll, D. Wang, and T. Shen, "Comparison of three methods to predic adsorption isotherms for organic vapors from similar polarity and nonsimilar polarity reference vapors," *Carbon*, vol. 27, pp. 239-245, 1989.

[111] G. O. Wood, "Activated carbon adsorption capacities for vapors," *Carbon*, vol. 30, pp. 593-599, 1992.

[112] L. M. Surhone, M. T. Tennoe, S. F. Henssonow, *Antoine equation*, Academia, VDM Publishing, Saarbrücken, Germany, 2010.

[113] M. J. E. Golay, "the height equivalent to a theoretical plate of retentionless rectangular tubes," *Journal of Chromatography A*, vol. 216, pp. 1-8, 1981.

[114] J. C. Giddings, J. P. Chang, M. N. Myers, J. M. Davis, and K. D. Caldwell, "Capillar liquid chromatography in field flow fractionation-type channels," *Journal of Chromatography A*, vol. 255, pp. 359-379, 1983.

[115] G. E. Spangler, "Relationships for modeling the performance of rectangular gas chromatographic columns," *Journal of Microcolumn Separations*, vol. 13, pp. 285-292, 2001.

[116] M. Fujii, X. Zhang, H. Xie, H. Ago, K. Takahashi, T. Ikuta, H. Abe, and T. Shimizu, "Measuring the thermal conductivity of a single carbon nanotube," *Physical Review Letters*, vol. 95, 065502, 2005.

[117] Z. Chen, W. Jang, W. Bao, C. N. Lau, and C. Dames, "Thermal contact resistance between graphene and silicon dioxide," *Applied Phycis Letters*, vol. 95, 161910, 2009.